Precursors_cci+

ESA Climate Change Initiative (CCI)

D2.1 Algorithm Theoretical Basis Document (ATBD) - Version 2

Title	D2.1 Algorithm Theoretical Basis Document
Reference	Precursors_cci+_D2.1_ATBD_02_03
Issue	02
Revision	03
Status	Final, corrected for RIDs
Date of issue	30/05/2025
Document type	Deliverable

This work has received funding from the European Space Agency under Contract No 4000138243 and is the result of the cooperation between the partners of the Precursors_cci+ consortium.

	FUNCTION	NAME	DATE
LEAD AUTHOR(S)		Folkert Boersma Sora Seo Pieter Valks Isabelle De Smedt Nicolas Theys Pascal Hedelt Thomas Danckaert Lieven Clarisse Martin Van Damme Cathy Clerbaux Maya George	30/05/2025
REVIEWED BY	Science Leaders	Michel Van Roozendael Folkert Boersma	30/05/2025 30/05/2025
	ESA Project Officers	Simon Pinnock Claire McIntosh	../../….
DISTRIBUTED TO	ESA Precursors_cci+ Consortium		

DOCUMENT CHANGE RECORD

Issue	Revision	Date	Modified items	Observations
0	0	15/05/2023	Initial template	Creation of document
1	0	01/10/2023	First issue of the document (version 1.0), containing descriptions of the L2 algorithms for all products	
1	1	15/12/2023	Revision of document version 1 according to ESA RIDs of 18/10/2023	
2	1	12/12/2024	Second issue containing updates of L2 algorithms and descriptions of the L3 algorithms	
2	2	12/02/2025	Final update, including all contributions	
2	3	30/05/2025	Version corrected for ESA RIDS	

Table of Contents

EXECUTIVE SUMMARY 11

1. PURPOSE AND SCOPE 12

1.1. Purpose 12

1.2. Scope 12

1.3. Applicable documents 12

1.4. Reference documents 12

1.5. List of acronyms 13

2. INSTRUMENTS 16

2.1. ERS-2/GOME 16

2.2. ENVISAT/SCIAMACHY 16

2.3. Sentinel-5P/TROPOMI 17

2.4. METOP/GOME-2 17

2.5. METOP/IASI 17

2.6. AURA/OMI 18

2.7. TERRA/MOPITT 18

3. L2 ALGORITHMS 19

3.1. Tropospheric nitrogen dioxide (L2-NO_2) 19
3.1.1. Overview 19
3.1.2. Algorithm description 19
3.1.3. NO_2 slant column density retrieval 20
3.1.4. Separation of stratospheric and tropospheric NO_2 23
3.1.5. Air mass factor and tropospheric NO_2 column calculation 25
3.1.6. Information content and uncertainty estimate 29

3.2. Formaldehyde (L2-HCHO) 31
3.2.1. Flow diagram of the L2 retrieval algorithm 31
3.2.2. Slant Columns 32
3.2.3. Air Mass Factors 33
3.2.4. Background correction 33
3.2.5. Error estimate, averaging kernels and qa_values 35

3.3. Sulfur dioxide (L2-SO_2) 37
3.3.1. Overview 37

3.3.2. Algorithm description 38
3.3.3. Information content and uncertainty estimate 42

3.4. Glyoxal (L2-CHOCHO) 43
3.4.1. Overview 43
3.4.2. Algorithm description 44
3.4.3. Information content and uncertainty estimate 51

3.5. Carbon monoxide (L2-CO) 53
3.5.1. Overview 53
3.5.2. Algorithm description 53
3.5.3. Uncertainty estimate 55

3.6. Ammonia (L2-NH_3) 56
3.6.1. Retrieval overview 56
3.6.2. HRI 58
3.6.3. The neural network 62
3.6.4. Averaging kernels 66
3.6.5. Retrieval, uncertainty, and post-filtering 68
3.6.6. Examples 70
3.6.7. Advantages of the retrieval algorithm 72
3.6.8. Comparison with an OEM retrieval 73

4. LEVEL-3 ALGORITHMS 75

4.1. Tropospheric nitrogen dioxide (L3-NO_2) from OMI and TROPOMI 75
4.1.1. Overview 75
4.1.2. Data gridding approach 75

4.2. Tropospheric nitrogen dioxide (L3-NO_2) from GOME, SCIAMACHY and GOME-2 81
4.2.1. Overview 81
4.2.2. Data gridding approach 81
4.2.3. Datasets 84

4.3. Formaldehyde (L3-HCHO) 88
4.3.1. Overview 88
4.3.2. Data gridding approach 88
4.3.3. Datasets 89

4.4. Sulfur dioxide (L3-SO_2) 93
4.4.1. Overview 93
4.4.2. Data gridding approach 93
4.4.3. Datasets 93

4.5. Glyoxal (L3-CHOCHO) 95
4.5.1. Overview 95
4.5.2. Data gridding approach 95
4.5.3. Datasets 95

4.6. Carbon monoxide (L3-CO) 97
4.6.1. Overview 97
4.6.2. Methodology 97
4.6.3. Dataset 100

4.6.4. L3 uncertainty estimate 101

4.7. Ammonia (L3-NH_3) 102
4.7.1. Overview 102
4.7.2. Data gridding 102
4.7.3. Example 103

5. REFERENCES 105

List of Figures

Figure 2-1: Overview of platforms and sensors used for the development and generation of CCI+ Precursors data records 16
Figure 3-1: General overview of the processing chain for the retrieval of the L2 tropospheric NO_2 columns. 20
Figure 3-2: Timeseries of stratospheric and tropospheric NO_2 over Europe derived with the data assimilation and STREAM approaches for GOME-2A. Tropospheric NO_2 column values (indicated in red and green) have been divided by a factor of 4. 24
Figure 3-3: Time series of the ratio of total tropospheric NO_2 vertical column to clear-sky tropospheric NO_2 vertical column retrieved using the OCRA/ROCINN and FRESCO v7 cloud products for GOME-2A over Europe. 27
Figure 3-4: Flow Diagram of the DOAS retrieval algorithm for HCHO. 31
Figure 3-5: Flow diagram of the SO_2 column retrieval algorithm. 37
Figure 3-6: Glyoxal retrieval flowchart 43
Figure 3-7: Mean Glyoxal SCD patterns recurring across different years and seasons. 49
Figure 3-8: Graphic representation of the processing steps. Satellite input data are in blue. 53
Figure 3-9: CO uncertainty time series for the globe, for day time and night time measurements, for both Metop-A and Metop-B. 55
Figure 3-10: Conceptual flowchart of the ANNI retrieval method for NH_3. 57
Figure 3-11: Eigenvalue spectrum of the covariance matrix $\mathbf{Sy}$ used for the calculation of the HRI of NH_3. The eigenvalues are ordered from largest to smallest. 60
Figure 3-12: Monthly average HRI time series over 10 remote regions for the three IASI instruments separately. The top panel shows the uncorrected timeseries, and the other panels, from top to bottom, show the effects of the corrections that are applied consecutively. 62
Figure 3-13: Frequency distribution of NH3 total columns (left) and $\boldsymbol{\sigma}$ (right) values in the v3 and v4 training set. 64
Figure 3-14: Summary statistics on the training set: distribution of thermal contrast vs NH_3 total columns (left), and spatial distribution vs thermal contrast (right). 64
Figure 3-15: Example of GEOS-Chem model (blue) and fitted (red) profiles (left) above a source area and (right) for transported NH_3. 64
Figure 3-16: Performance evaluation of the neural network, with added noise. The median value is shown in each grid box, which removes the effect of outliers to better reflect the real performance of the network. 66
Figure 3-17: Numerical demonstration of the linearity and additivity of the HRI as a function of a change in partial column. In the blue and green scenario, NH_3 was varied at one fixed altitude. In the red scenario, partial columns in both layers were varied simultaneously. The black solid lines represent linearity, whereas the dash dotted line, being the sum of the green and blue curve, represents additivity. 67
Figure 3-18: Example ERA5 climatology of the planetary boundary layer for April, morning (left) and evening (right). 69
Figure 3-19: Example NH_3 retrievals from IASI-B on 24 April 2020 (AM, top; PM, bottom). Grey pixels are either cloudy or pixels that do not pass the post filter. 71

Figure 3-20: NH_3 seasonal average, derived from 0.5° by 0.5° monthly averages of the reanalysis product of ANNI v4. Data includes all measurements from IASI-A (October 2007 to December 2019), IASI-B (March 2013 to September 2022) and IASI-C (September 2019 to September 2022), with a cloud fraction below 10 %. 72
Figure 3-21: Comparison between ANNI v4 NH_3 columns and retrievals based on optimal estimation for two scenes, one over Europe (top panels, 18 April 2013, Metop A morning overpass) and North America (bottom panels, 6 May 2021, Metop B morning overpass). The left panels depict the optimal estimation retrieved columns. The middle panels are scatter plots between the two retrievals, where each observation is colour coded according to thermal contrast (brightness temperature of the surface minus the temperature at half the boundary layer height). The right panels summarize the comparison by means of histograms of the differences. 74
Figure 4-1: Schematic example of the procedure to calculate spatio-temporal (gridded) averages of retrieved NO_2 columns for OMI and TROPOMI. 76
Figure 4-2: Monthly mean tropospheric NO_2 columns from L3 products of OMI and TROPOMI for January and June 2019, as well as the total uncertainty for June 2019. 78
Figure 4-3: Timeseries of OMI and TROPOMI L3 monthly NO_2 tropospheric columns, as well as OMI sampled excluding row anomaly affected rows, and TROPOMI co-sampled with OMI over a remote Pacific region, East Asia, Europe and Beijing. 79
Figure 4-4: Tropospheric and full averaging kernel over Beijing for January and July 2019 from OMI L3. 80
Figure 4-5: Effective date (day of the month) and fractional day for January 2019 for TROPOMI L3. 80
Figure 4-6: An example of GOME-2A ground pixel (blue) overlaid on a 0.25° x 0.25° latitude-longitude grid (grey). The percentage of overlap (weighting, $\boldsymbol{w}$) for each grid box is denoted. (image credit: Chan et al., 2023) 82
Figure 4-7: Time series of monthly zonal averages of tropospheric NO_2 columns from GOME-2A, GOME-2B and GOME-2C across different latitudinal bands from 2007 to 2023. 84
Figure 4-8: Monthly averaged tropospheric NO_2 columns at 0.2° × 0.2° resolution from L3 products of GOME-2A, GOME-2B and GOME-2 for February 2019 85
Figure 4-9: Monthly averaged tropospheric air mass factors at 0.2° × 0.2° resolution from L3 products of GOME-2A, GOME-2B and GOME-2 for February 2019 86
Figure 4-10: Time series of monthly average tropospheric NO_2 VCDs from all morning sensors (GOME/ERS-2, SCIAMACHY/ENVISAT, and GOME-2/MetOp-ABC) L3 NO_2 products, covering six source regions from 1995 to 2023. 87
Figure 4-11: Schematic representation of L2 pixels (blue) gridded into a pre-defined grid cell (red). 89
Figure 4-12: TROPOMI L3 gridded variables for August 2022: (a) HCHO clear VCD, (b) bc-corrected SCD, (c) a priori integrated HCHO column, (d) clear AMF. 90
Figure 4-13: (a) L3 monthly gridded a priori profiles and averaging kernel (Aug. 2022) over RC Congo, (b) re-calculated AMF using only the L3 variables (AK, Profiles, surface pressure), (c) differences compared to the L3 gridded AMF. 91
Figure 4-14: Effective date (day of the month) and fractional day gridded in August 2022 for TROPOMI. 91

Figure 4-15: OMI L3 gridded variables for September 2005: (a) SO_2 VCD, (b) SO_2 SCD, (c) a priori integrated SO_2 column, (d) total AMF. 94
Figure 4-16: August 2023 CHOCHO-L3 VCD, a priori VCD, SCD and AMF 96
Figure 4-17: MOPITT, IASI and CCI+ MERGED CO grids for July 2008 (daytime). White areas are cell grids with no data. 99
Figure 4-18: Key variables of CCI+ CO merged monthly L3 product from IASI and MOPITT. Example for July 2008. CO total column (line 1), associated uncertainty (line 2), data source flags (line 3), and surface altitude (line 4), for both daytime (left) and nighttime (right) observations. Flags identify sources: 3 = both IASI and MOPITT, 2 = IASI only, 1 = MOPITT only, 0 = no data. 100
Figure 4-19: CO uncertainty time series for the [20°N-60°N] latitude band, for daytime measurements. The new merged CO CCI+ product is represented in red, IASI in blue and MOPITT in grey. 101
Figure 4-20: Illustration of the weight calculation of an IASI observation (orange ellipse), onto regular grid. 103
Figure 4-21: Illustration of six key variables in the NH_3 L3 datasets. 104

List of Tables

Table 3-1: Overview of NO_2 slant column density settings for morning sensors 20
Table 3-2: Overview of NO_2 slant column density settings for afternoon sensors..... 22
Table 3-3: Overview of stratospheric NO_2 estimation settings for morning sensors. 25
Table 3-4: Selected settings for forward model parameters used in the calculation of tropospheric NO_2 AMFs in the ESA CCI ECV Precursor project for the morning sensors. 28
Table 3-5: Selected settings for forward model parameters used in the calculation of tropospheric NO_2 AMFs in the ESA CCI ECV Precursor project for the afternoon sensors. 28
Table 3-6: Estimation of the uncertainty contributions to the overall, per-pixel tropospheric NO_2 column uncertainty over polluted regions. 30
Table 3-7: Settings used for DOAS spectral fitting for the different satellite instruments. 32
Table 3-8: Input used for AMF calculation for the different satellite instruments. 33
Table 3-9: Background correction settings for the different satellite instruments. 34
Table 3-10: Description of the HCHO qa_value definition 36
Table 3-11: Settings used for COBRA spectral fitting for the different satellite instruments used (preliminary). 40
Table 3-12: Criteria for selecting alternative fitting windows. 40
Table 3-13: Input parameters used for AMF calculation and the for the different satellite instruments used (preliminary) 41
Table 3-14: Estimation of the error sources of the SO_2 COBRA retrieval (preliminary) for typical polluted conditions, at low/high SZA (latitudes). Blue and red fields indicate random (precision) and systematic (trueness) errors. Total errors are computed assuming all contributions are mutually uncorrelated. 42
Table 3-15: Selected pacific background region for daily reference radiance per instrument. 44
Table 3-16: Absorption cross sections 44
Table 3-17: Radiative transfer input data per sensor. 45
Table 3-18: Glyoxal tropospheric vertical column density retrieval uncertainty components 51
Table 3-19: Summary of the origin of the ANNI input parameters for NH_3. 69
Table 4-1: Summary of characteristics of the morning sensor instruments and L2 data products. 81
Table 4-2: Spatial resolution for morning and afternoon L3 products, at daily and monthly time resolution. 88
Table 4-3: Spatial resolution for morning and afternoon L3 products, at daily and monthly time resolution. 95

Executive Summary

The Algorithm Theoretical Basis Document (ATBD, deliverable D2.1 in Precursors_cci+) describes the algorithms used for the generation of the NO_2, HCHO, SO_2, glyoxal (CHOCHO), CO and NH_3 data products. The document covers level-2 and level-3 algorithms and includes descriptions of the sensors used, retrieval methods applied, ancillary data sets as well as a synthetic description of the uncertainty budget. A detailed analysis of the uncertainty budget is provided separately in the End-to-End ECV Uncertainty Budget document (E3UB) (D2.2).

1. Purpose and scope

1.1. Purpose

This document describes the retrieval algorithms used in the Precursors_cci+ project. It addresses six important precursors of ozone and aerosol ECVs, namely: tropospheric NO_2, HCHO, CO, SO_2, NH_3 and glyoxal.

1.2. Scope

The scope of the ATBD is to fully describe each retrieval algorithm used to derive the ECV products from input satellite data. This includes descriptions of input satellite data and ancillary data, retrieval methods and procedures including pre- or post-processing steps, and a general overview of the processing chain applied for each trace gas product. The ATBD addresses both level-2 (L2) and level-3 (L3) retrieval algorithms.

1.3. Applicable documents

[AD-1] Data Standards Requirements for CCI Data Producers. Latest version at time of writing is v1.2: ref. CCI-PRGM-EOPS-TN-13-0009, 9 March 2015, available online at: https://climate.esa.int/media/documents/CCI_DataStandards_v2-3.pdf

[AD-2] CCI Data Policy v1.1. Available online at: https://climate.esa.int/sites/default/files/CCI_Data_Policy_v1.1.pdf

[AD-3] CCI Data Policy v1.1. Available online at: https://climate.esa.int/sites/default/files/CCI_Data_Policy_v1.1.pdf

1.4. Reference documents

[RD-1] GCOS Climate Monitoring Principles, November 1999. Available online at: https://gcos.wmo.int/en/essential-climate-variables/about/gcos-monitoring-principles

[RD-2] Guideline for the Generation of Satellite-based Datasets and Products meeting GCOS Requirements, GCOS Secretariat, GCOS-128, March 2009 (WMO/TD No. 1488). Available online at: https://library.wmo.int/index.php?lvl=notice_display&id=12884#.Yw4rL7RByUk

[RD-3] Quality assurance framework for earth observation (QA4EO): http://qa4eo.org

[RD-4] The Global Observing System for Climate: Implementation Needs, GCOS-200, October 2016. Available online at: https://gcos.wmo.int/en/gcos-implementation-plan

[RD-5] Status of the Global Observing System for Climate, GCOS-195, October 2015. Available online at: https://library.wmo.int/index.php?lvl=notice_display&id=18962#.Yw4r8LRByUk

[RD-6] Hollmann, R., et al., The ESA climate change initiative: Satellite data records for essential climate variables. American Meteorological Society. Bulletin, Vol. 94, No. 10, 2013, p. 1541-1552.

[RD-7] Joint Committee for Guides in Metrology, 2008, Evaluation of measurement data — Guide to the expression of uncertainty in measurement (GUM), JGCM 100: 2008. Available online at: https://www.iso.org/sites/JCGM/GUM-JCGM100.htm

[RD-8] Merchant, C., et al., 2017, Uncertainty information in climate data records from Earth observation, Earth Syst. Sci. Data Discuss., vol. 9, p511-527

[RD-9] Precursors_cci+ User Requirement Document (URD), version 1, ref. Precursors_cci+_D1.1_URD_01_01, 25 January 2024, https://climate.esa.int/en/projects/precursors-for-aerosols-and-ozone/

[RD-10] Precursors_cci+ Algorithm Theoretical Basis Document (ATBD), version 1, ref. Precursors_cci+_D2.1_ATBD_00_01, 15 December 2023, https://climate.esa.int/en/projects/precursors-for-aerosols-and-ozone/

[RD-11] Precursors_cci+ End to End ECV Uncertainty Budget (E3UB), version 1, ref. Precursors_cci+_D2.2_E3UB_01_02, 24 June 2024, https://climate.esa.int/en/projects/precursors-for-aerosols-and-ozone/

[RD-12] Precursors_cci+ Product User Guide (PUG), version 1, ref. Precursors_cci+_D4.2_PUG_01_01, 29 May 2024, https://climate.esa.int/en/projects/precursors-for-aerosols-and-ozone/

[RD-13] Precursors_cci+ Product Validation and Algorithm Selection Report (PVASR), version 1, ref. Precursors_cci+_D2.3_PVASR_01_01, 29 April 2024, https://climate.esa.int/en/projects/precursors-for-aerosols-and-ozone/

[RD-14] Precursors_cci+ Product Validation and Intercomparison Report (PVIR), version 1, ref. Precursors_cci+_D4.1_PVIR_01_01, 26 April 2024, https://climate.esa.int/en/projects/precursors-for-aerosols-and-ozone/

[RD-15] Precursors_cci+ Climate Assessment Report (CAR), version 1, ref. Precursors_cci+_D5.1_CAR, Precursors_cci+_D5.1_CAR_01_02, 23 April 2024, https://climate.esa.int/en/projects/precursors-for-aerosols-and-ozone/

1.5. List of acronyms

AC-SAF	Satellite Application Facility on Atmospheric Composition Monitoring
ADP	Algorithm Development Plan
AK	Averaging Kernel
AMF	Air-mass factor
ATBD	Algorithm Theoretical Basis Document
BIRA-IASB	Royal Belgian Institute for Space Aeronomy
BIRA-IR	BIRA-IASB Infrared Team
BIRA-SYN	BIRA-IASB Synergy Team
BIRA-UVVIS	BIRA-IASB UV-Vis Team
BIRA-MOD	BIRA-IASB Tropospheric Modeling Team
CAMS	Copernicus Atmospheric Monitoring Service

C3S	Copernicus Climate Change Monitoring Service
CCI	ESA Climate Change Initiative
CCI+	Climate Change Initiative Extension (CCI+), is an extension of the CCI over the period 2017-2024.
CEOS	Committee on Earth Observation Satellites
CMUG	Climate Modeling User Group
CO	Carbon monoxide
COBRA	COvariance-Based Retrieval Algorithm
CRDP	Climate Research Data Package
CRG	Climate Research Group
DLER	Directional Lambertian Equivalent Reflectance
DLR	German Aerospace Centre
DOAS	Differential Optical Absorption Spectroscopy
ECMWF	European Centre for Medium-range Weather Forecast
ECV	Essential Climate Variable
ENVISAT	Environmental Satellite (ESA)
EO	Earth Observation
ESA	European Space Agency
EU	European Union
EUMETSAT	European Organisation for the Exploitation of Meteorological Satellites
FCDR	Fundamental Climate Data Record
FRESCO	Fast Retrieval Scheme for Clouds from the Oxygen A band
FRM	Fiducial Reference Measurement
GCOS	Global Climate Observation System
GOME	Global Ozone Monitoring Instrument (aboard ERS-2)
GOME-2	Global Ozone Monitoring Instrument – 2 (aboard MetOp-A, -B and -C)
IASI	Infrared Atmospheric Sounding Interferometer
HRI	Hyperspectral Range Index
KNMI	Royal Netherlands Meteorological Institute
LEO	Low Earth Orbit
LER	Lambertian Equivalent Reflectance
LUT	Look-up table
Metop	Meteorological Operational Platform (EUMETSAT)
MOPITT	Measurement of Pollution in the Troposphere
NASA	National Aeronautics and Space Administration
NDACC	Network for the Detection of Atmospheric Composition Change
NH_3	Ammonia
NN	Neural Network
NO_2	Nitrogen dioxide
NRT	Near-Real Time
OCRA	Optical Cloud Recognition Algorithm)
OMI	Ozone Monitoring Instrument (aboard EOS-Aura)
PCA	Principal Component Analysis
QA4ECV	Quality Assurance for Essential Climate Variables
QA4EO	Quality Assurance framework four Earth Observation

R&D	Research and Development
ROCINN	Retrieval of Cloud Information using Neural Networks
SAF	Satellite Application Facility
SCIAMACHY	Scanning Imaging Absorption Spectrometer for Atmospheric
S5P	Sentinel-5 Precursor
SoW	Statement of Work
STREAM	STRatospheric Estimation Algorithm from Mainz
SZA	Solar Zenith Angle
TEMIS	Tropospheric Emission Monitoring Internet Service
TIR	Thermal Infrared spectral range
TROPOMI	Tropospheric Monitoring Instrument (aboard Sentinel-5 Precursor)
TOA	Top-of-atmosphere
TOAR-II	Tropospheric Ozone Assessment Report Phase-II
ULB	Université Libre de Bruxelles
IUP-UB	Institute of Environmental Physics, University of Bremen
UPAS	Universal Processor for UV/Vis Atmospheric Sensors
UV-Vis	Ultraviolet and visible spectral range
WP	Work Package

2. Instruments

Ozone and aerosol precursors under focus in this project can be retrieved from a series of nadir UV-VIS and thermal infrared (TIR) sensors. We focus more particularly on the ESA and ESA Third Party Mission (ESA-TPM) sensors listed in Figure 2-1 and shortly described in this section.

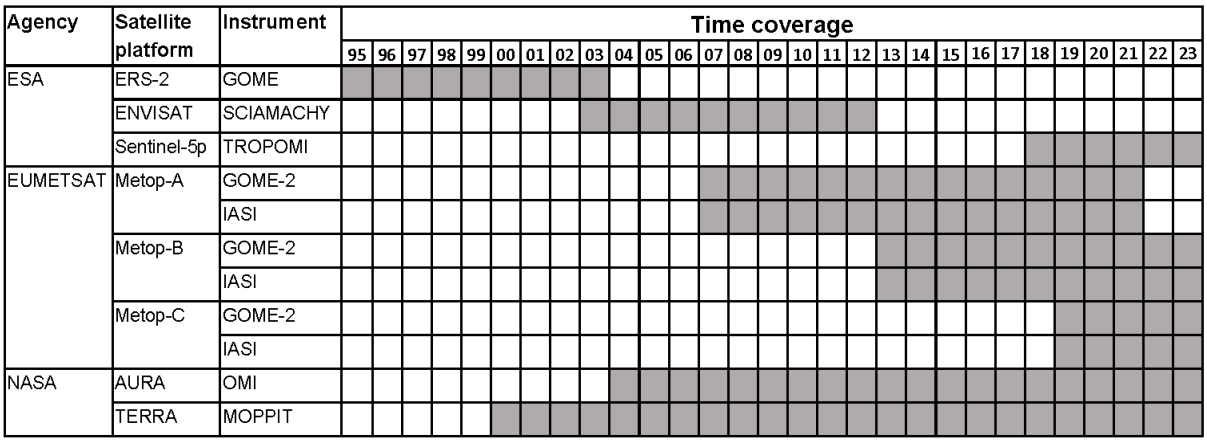

Figure 2-1: Overview of platforms and sensors used for the development and generation of CCI+ Precursors data records

2.1. ERS-2/GOME

The GOME (Global Ozone Monitoring Experiment) instrument is a 4 channel UV/Vis grating spectrometer which observed the earth's atmosphere in nadir viewing geometry. It has a moderate spectral resolution of 0.2 - 0.4 nm and a ground-pixel size of 320 x 40 km2 (960 x 40 km2 for the back scan). A detailed description of the instrument is given in Burrows et al. (1999). GOME was launched on ERS-2 into a sun synchronous polar orbit in April 1995, and delivered data until June 2011 when the ERS-2 platform was shut down. However, as a result of aging problems of the ERS-2 platform, pointing accuracy is reduced from February 2001. This affects mainly the solar measurements of GOME, decreasing the frequency of good solar irradiance measurements and thereby increasing noise in some products. Further, since June 2003, a permanent failure of the last tape recorder on ERS-2 limits GOME coverage to areas where direct downlink of data was possible. In Ozone_cci, GOME measurements are used to retrieve total columns and vertical distributions of ozone. Because of its proven stability and of its long lifetime (16 years), GOME is generally considered as the European “Gold Standard” for total ozone measurements.

2.2. ENVISAT/SCIAMACHY

SCIAMACHY (Scanning Imaging Absorption Spectrometer for Atmospheric CHartographY) is a multi-channel UV-Vis-NIR spectrometer launched on the ENVISAT platform in 2002. Its primary mission objective was the global monitoring of trace gases in the troposphere and in the stratosphere (Bovensmann et al., 1999). The solar radiation transmitted, backscattered and reflected from the atmosphere is recorded at medium resolution (0.2 nm to 1.5 nm) over

the range 240 nm to 1700 nm, and in selected regions between 2.0 µm and 2.4 µm. SCIAMACHY is particular since it has three different viewing geometries: nadir, limb, and sun/moon occultation, which yield total column values as well as distribution profiles in the stratosphere and upper troposphere. In this project both nadir and limb measurements are used in Channels 1, 2 and 3. In nadir view, used for ozone total column and vertical profile retrievals, the ground pixel size for channels 2-3 is 30x60 km^2, i.e. a resolution intermediate between GOME and OMI. The swath width of SCIAMACHY at nadir is similar to GOME (960 km), however due to the alternate nadir and limb mode operation, global coverage is only obtained in approximately 6 days. In limb view, ozone number density profiles are derived in the stratosphere by exploiting the Hartley and Chappuis spectral absorption bands in channels 1 and 3. SCIAMACHY data are available from July 2002 till April 2012 when communication with ENVISAT was lost.

2.3. Sentinel-5P/TROPOMI

The TROPOMI instrument is a space-borne, nadir-viewing, imaging spectrometer covering wavelength bands between the ultraviolet and the shortwave infrared. It is the single payload of Sentinel-5 Precursor, the first Copernicus mission dedicated to the monitoring of atmospheric composition. Launched on 13 October 2017 for a mission of minimum seven years, it operates in a push-broom configuration (non-scanning), with a swath width of ~2600 km on the Earth's surface. The TROPOMI instrument is similar in concept to OMI, but it offers a much-improved spatial resolution of about 5.5x3.5 km2 at nadir, with similar or better radiometric performance than OMI. Covering the ultraviolet (UV), visible (VIS), near (NIR) and short-wavelength infrared (SWIR), it provides daily global measurements of a number of gases in the atmosphere, including ozone, methane (CH_4), HCHO, NO_2, SO_2, aerosol and carbon monoxide (CO).

2.4. METOP/GOME-2

The first GOME-2 instrument was launched on-board the EUMETSAT satellite Metop-A in October 2006 (Munro et al., 2016). Built on a design almost identical to GOME, it covers the same spectral range as its predecessor but with an improved spatial resolution. The nominal ground-pixel size is 80 x 40 km2 with a global coverage in almost one day (swath of 1920 km). GOME-2 continues the measurement series started with GOME, and in this project it is therefore used to retrieve total columns and vertical distributions of ozone. Data are available since January 2007 on an operational basis. A second GOME-2 instrument was launched in 2012 on the Metop-B platform, and a third one was launched in November 2018 on Metop-C.

2.5. METOP/IASI

The Infrared Atmospheric Sounding Interferometer (IASI) is a nadir looking Fourier Transform Spectrometer associated with an imaging instrument launched on the Metop series of European meteorological EUMETSAT's polar-orbit satellites. The mission is dedicated to high-resolution atmospheric sounding of trace gases like ozone, methane or carbon monoxide on a global scale and to operational meteorological soundings with a high accuracy requirement (1 K for tropospheric temperature and 10% for humidity with a vertical resolution of 1 km). Three IASI instruments have been successively launched in October 2006, in September 2012

and in November 2018 on Metop-A, -B and –C respectively. The Metop satellites are sun-synchronous with a 98.7° inclination to the equator, and a global coverage twice daily at about 09:30 and 21:30 local time. Each of the three launched Metop platforms makes a little more than 14 orbits a day. IASI is a cross-track scanner covering the infrared spectral domain from 645 to 2,760 cm−1 (3.62–15.5 µm) with a total of 30 ground fields of regard (FOR) per scan. The spectrum is measured in three wavelength bands (8.26–15.5, 5.0–8.26, and 3.62–5.0 µm), with a separate detector allowing the continuous spectral coverage with no gaps, and each FOR measures a 2×2 array of footprints characterized by a 12-km diameter at nadir. The apodized spectral resolution is 0.5 cm−1 and each spectrum is sampled every 0.25 cm−1 providing a total of 8461 radiance channels.

2.6. AURA/OMI

The Ozone Monitoring Instrument (OMI) is a nadir viewing imaging spectrograph that measures the solar radiation backscattered by the Earth's atmosphere and surface over the entire wavelength range from 270 to 500 nm with a spectral resolution of about 0.5 nm. OMI was launched on-board the NASA satellite AURA in July 2004. In comparison to the GOME and SCIAMACHY sensors, OMI is characterized by a larger swath width of 2600 km, which enables measurements with a daily global coverage at all latitudes. The nominal OMI pixel size of 13 × 24 km^2 at nadir is also significantly smaller. The small pixel size enables OMI to look in between the clouds, which is important for retrieving tropospheric information. The light entering the telescope is also depolarised using a scrambler, which avoids polarization-related artefacts. OMI data are available since 2004 and the instrument is still operational, however in 2007 OMI started to experience the so-called row anomaly which reduces the amount of useful measurements, despite correction algorithms being implemented in the L1 processing chain.

2.7. TERRA/MOPITT

MOPITT (Measurement of Pollution in the Troposphere) is one of the earliest satellite sensors to use gas correlation spectroscopy. It is a nadir sounding (vertically downward pointing) instrument that measures upwelling infrared radiation at 4.7 µm and 2.2-2.4 µm. It was launched on the NASA Terra satellite in December 1999. The Terra satellite is in a 705-km, sun-synchronous orbit with a 10:30 a.m. equator crossing time.

The MOPITT sensor measures emitted and reflected radiance from the Earth in three spectral bands. As this light enters the sensor, it passes along two different paths through onboard containers of carbon monoxide. The different paths absorb different amounts of energy, leading to small differences in the resulting signals that correlate with the presence of these gases in the atmosphere. MOPITT’s spatial resolution is 22 km at nadir with a swath of 640 km wide. It can measure the concentrations of carbon monoxide in 5-km layers down a vertical column of atmosphere, to help scientists track the gas back to its sources.

3. L2 algorithms

3.1. Tropospheric nitrogen dioxide (L2-NO_2)

3.1.1. Overview

The L2 algorithms used to generate a tropospheric nitrogen dioxide product from the GOME, SCIAMACHY, GOME-2, OMI and TROPOMI sensors are based on the DOAS-approach and follow the same retrieval principles. The L2-NO_2 data products have the tropospheric NO_2 column density as their main retrieval outcome, but also provide the stratospheric vertical column and total vertical column density. The algorithms provide geophysical data for every ground pixel observed by the 5 sensors. In addition to the vertical columns, the L2_NO_2 dataset will contain retrieval uncertainty estimates for every pixel, and information on intermediate retrieval steps, such as the spectral fitting result and diagnostics, and information on factors that have influenced the retrieval such as clouds, surface reflectance, and the vertical distribution of NO_2.

3.1.2. Algorithm description

The NO_2 retrieval procedure consists of a procedure with three steps, and is performed for each L1 spectrum:

(1) Retrieval of the total NO_2 slant column density (N_s) from the L1 radiance and irradiance spectra measured by the sensor with the Differential Optical Absorption Spectroscopy (DOAS) method,
(2) Separation of the N_s into a stratospheric (N_s^{strat}) and tropospheric part ($N_s^{trop} = N_s - N_s^{strat}$) based on information from a system incorporating slant columns and modelled or climatological information on tropospheric contributions,
(3) Conversion of the tropospheric slant column density into a vertical column density (N_v^{trop}) via a tropospheric air mass factor (M^{trop}).

The central retrieval equation can thus be written as:

$$N_v^{trop} = \frac{N_s - N_s^{strat}}{M^{trop}} \qquad \textbf{Eq. 3-1}$$

In Eq. 3-1 the factor M^{trop} quantifies how the tropospheric slant column has been influenced by scattering, absorption, and reflection in the troposphere or by the Earth's surface. M^{trop} depends on the satellite viewing geometry, the presence of clouds or aerosols, surface properties, and the vertical distribution of NO_2 in the troposphere. The retrieval procedure therefore requires accurate, pixel-specific information on these geophysical parameters, and the NO_2 L2 algorithms obtain this from the satellite measurements themselves, or from well-tested ancillary datasets.

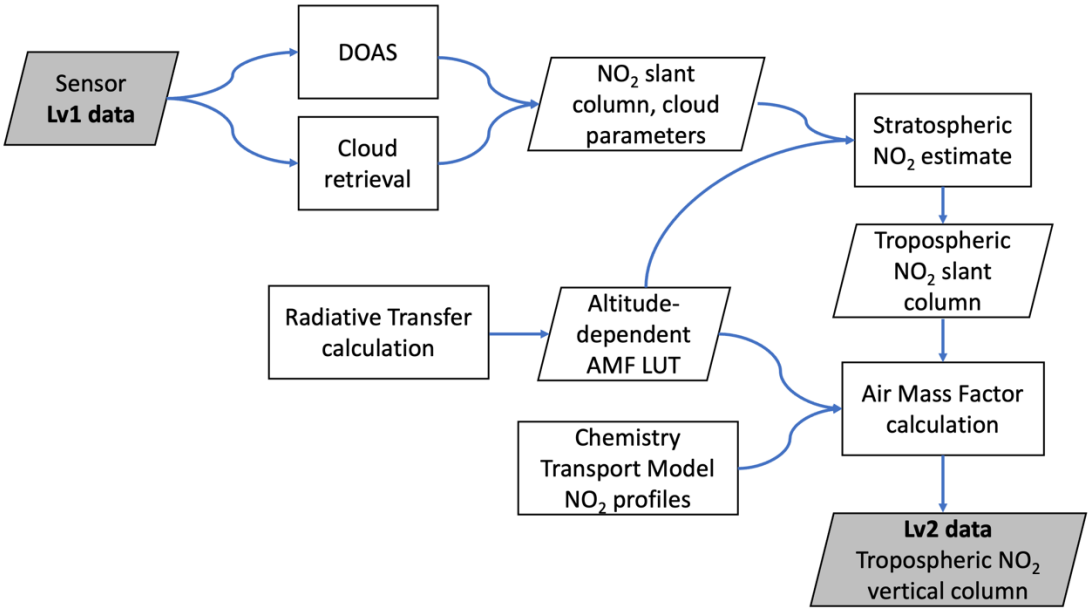

Figure 3-1: General overview of the processing chain for the retrieval of the L2 tropospheric NO_2 columns.

For all 5 sensors, the retrieval procedure for NO_2 is identical in terms of retrieval steps. But because of instrumental differences in terms of overpass time, spectral range, calibration issues and limitations in terms of processing capacity, different approaches are required for different instruments in some cases. In what follows, we describe what actions have been taken to ensure as much as possible consistency between L2 NO_2 products.

3.1.3. NO_2 slant column density retrieval

The approach to determine NO_2 slant column densities from L1 data is DOAS. The below tables summarize the settings selected for NO_2 slant column density retrieval for each of the five morning sensors (Table 3-1) and the two afternoon sensors (Table 3-2).

Table 3-1: Overview of NO_2 slant column density settings for morning sensors

	GOME	SCIAMACHY	GOME-2A	GOME-2B	GOME-2C
L1 version	v5.1	v8	v6.3	v6.3	v6.3
Fitting window	425-465 nm	425-465 nm	425-497 nm	425-497 nm	430-465 nm[1]
Fitting method	Optical density	Optical density	Optical density	Optical density	Optical density

[1] Systematic offsets between GOME-2C and GOME-2A/B slant columns because of level-1 issues in GOME-2C. To ensure consistency in NO_2 slant columns between the three instruments, a different spectral fitting window was selected for GOME-2C.

Solar reference	Daily Pacific radiance spectrum[2]	Daily solar reference using ASM diffusor	SAO solar reference in vacuum[3]	SAO solar reference in vacuum	SAO solar reference in vacuum
Polynomial	4th order	4th order	5th order	5th order	4th order
Fitting parameters	NO_2, O_3, O_2-O_2, H_2O, Ring, liquid water	NO_2, O_3, O_2-O_2, H_2O, Ring, liquid water	NO_2, O_3, O_2-O_2, H_2O, Ring, liquid water	NO_2, O_3, O_2-O_2, H_2O, Ring, liquid water	NO_2, O_3, O_2-O_2, H_2O, Ring, liquid water
Undersampling correction	Yes	No	No	No	No
Eta correction	Yes	No	Yes[4]	Yes	Yes
Reference	Boersma et al. (2018)	Boersma et al. (2018)	Liu et al. (2019)	Liu et al. (2019)	Valks et al. (2019)

Most settings are highly consistent between the morning sensors. Previous tests indicated excellent consistency between GOME and SCIAMACHY NO2 slant columns despite different usage of solar reference (QA4ECV D4.5 – Figure 20). Georgoulias et al. (2019) showed that the (QA4ECV) data products from GOME, SCIAMACHY and GOME-2A are fit-for-purpose of monitoring long-term trends in tropospheric NO_2 columns, a further indication of good consistency of the NO_2 slant columns.

Tests in the Round Robin phase in this project showed very good consistency between NO_2 slant columns from GOME-2A and GOME-2B derived with the 425-497 nm window. The selection of this window however is a notable change relative to the 405-465 nm window used for GOME-2A in the QA4ECV-project. Round Robin tests indicated that the NO_2 slant columns obtained from the 405-465 nm spectral window show a good overall consistency with those from the 425-497 nm window (used in the AC-SAF prototype). However, after June 2015, the GOME-2A NO_2 slant columns from the 405-465 nm window show substantial sensitivity to the updated v6.1 (and later versions) GOME-2A L1b data, diagnosed as stronger seasonality and 'jumps' in NO_2 slant column over background areas. Small uncertainties and high robustness in GOME-2A NO_2 slant columns are obtained with the 425-497 nm window and with the v6.3 L1 data also after June 2015. This fitting window, in conjunction with the v6.3 level 1b data also significantly reduces the inter-instrument bias between GOME-2A and GOME-2B, which is why they are the recommended setting for GOME-2 retrievals in the ESA CCI+ ECV Precursor project.

For GOME-2 on MetOp-C, an alternative fitting window 430 - 465 nm is used. This adjustment was made due to a significant (~40%) positive offset observed between NO_2 slant columns from GOME-2C and GOME-2A/B when applying an identical fitting window (EUMETSAT, 2019). This offset is related to systematic structures in the DOAS fitting residual for GOME-2C at wavelengths < 430 nm. By shifting the start wavelength for GOME-2C to 430 nm and the end

[2] The Pacific Ocean reference sector is the region enclosed by 10° S – 10° N, 160° E – 100° W, +1.476 10^{15} molec.cm^{-2} in reference spectrum
[3] sao_solref_vac
[4] Eta and Zeta from GOME-2 calibration key data

wavelength to 465 nm, the inter-instrument bias in NO_2 slant columns between GOME-2C and GOME-2A/B is effectively reduced, while maintaining a high signal-to-noise.

The spectral fitting settings selected for the afternoon sensors OMI and TROPOMI are indicated in Table 3-2. For OMI, most settings are consistent with those used within the QA4ECV project. However, since that project ended, a new OMI L1 data set has become available (Kleipool et al., 2022) in line with developments for TROPOMI. The new collection-4 L1 data comprise a clear improvement relative to the previous OMI L1 data and will be used as starting point for the spectral fitting from OMI. A second deviation with respect to the QA4ECV OMI NO_2 spectral fitting is that the set of fitting parameters no longer includes the intensity offset correction. Including such a term in the spectral fitting has been shown to impact the NO_2 slant columns up to 1×10^{15} molec.cm^{-2} (QA4ECV D4.2) over clean ocean scenes, where the term accounts for spectral structures associated with vibrational Raman scattering in water and results in smaller uncertainties and somewhat lower NO_2 slant columns (Oldeman, 2018). Leaving out the intensity offset term in the spectral fitting however has the advantage of making the OMI DOAS fit consistent with the TROPOMI DOAS fit (van Geffen et al., 2022).

Table 3-2: Overview of NO_2 slant column density settings for afternoon sensors.

	OMI	**TROPOMI**
L1 version	Coll004	v2.0
Fitting window	405-465 nm	405-465 nm
Fitting method	Optical density	Optical density
Solar reference	Annual mean solar reference	
Polynomial	4th order	4th order
Fitting parameters	NO_2, O_3, O_2-O_2, H_2O, Ring, liquid water	NO_2, O_3, O_2-O_2, H_2O, Ring, liquid water
Undersampling correction	No	No
Eta correction	No	No
Reference	Boersma et al. (2018)	van Geffen et al. (2021) van Geffen et al. (2022)

The temperature for the absorption cross-section spectra of the fitting parameters is fixed. The spectral shape of these cross-section spectra usually does not change with temperature, but for NO_2, the amplitude decreases with increasing atmospheric temperature (Boersma et al., 2004). The final NO_2 slant column densities therefore need to be corrected for deviations of the effective atmospheric NO_2 temperature from T = 220 K, at which the NO_2 cross section was measured as used in most spectral fitting retrievals. This correction requires knowledge of vertical NO_2, temperature, and sensitivity profiles and is therefore done at step 3 – the air mass factor calculation- of the retrieval (Figure 3-1).

OMI and TROPOMI NO_2 SCDs showed across-track biases, or stripes, due to small detector viewing angle dependent differences in calibration parameters. A destriping approach, integrated in the retrieval algorithm, is applied after the retrieval of the SCDs. The destriping

correction is determined from orbits over the Pacific Ocean (150 – 180 W over 30 belt in the Tropics). Subsequently, the NO_2 SCDs are corrected by subtracting the stripe amplitude correction. Further details can be found in Boersma et al. (2011), Boersma et al. (2018), and van Geffen et al. (2022).

3.1.4. Separation of stratospheric and tropospheric NO_2

The next major algorithm step in the L2 algorithm is the estimation of the stratospheric NO2 column density. The Round Robin outcome, recommendations from the QA4ECV project, and recent validation studies (Verhoelst et al. (2021); Wang et al. (2020); Compernolle et al. (2020); Hendrick ret al. (2012)) pointed out that there are only small differences between forecast stratospheric NO_2 based on **data assimilation** of NO_2 slant columns in TM5-MP (Dirksen et al., 2011) and daily smoothed stratospheric NO_2 estimated with the **STREAM** approach (Beirle et al., 2016). Based on this body of evidence we consider both data assimilation and STREAM viable approaches to separate the stratospheric from the tropospheric NO_2 signal for the retrievals in this project. Practical considerations dictate that L2-retrievals performed at KNMI use data assimilation and those performed at DLR use STREAM. Table 3.3 below provides an overview of the algorithm settings and inputs for the morning sensors. For the afternoon sensors, both retrieval algorithms are operated at KNMI, data assimilation will be used as in the QA4ECV and S5P projects.

The methods to estimate stratospheric NO_2 resemble one another in that they use a similar weighting scheme, which effectively screens slant columns retrieved over polluted regions and regions with substantial tropospheric NO_2 background. There are some differences between the two approaches, which are worth emphasizing:

- Data assimilation provides a stratospheric NO_2 field which is model-predicted, but strongly rooted in an observation-driven system.
- STREAM provides a smoothed, spatially interpolated stratospheric NO_2 field, which is based on daily observations, and on assumptions that spatial variability in stratospheric NO_2 is generally smooth.

Figure 3-2 illustrates the good consistency between the data assimilation and STREAM methods in estimating the stratospheric NO_2 amounts over Europe from GOME-2A. After June 2015, the discrepancies between data assimilation and STREAM increase somewhat, especially in summer, but this mainly reflects systematic differences in the input NO_2 slant column datasets used in the two retrievals tested in the Round Robin.

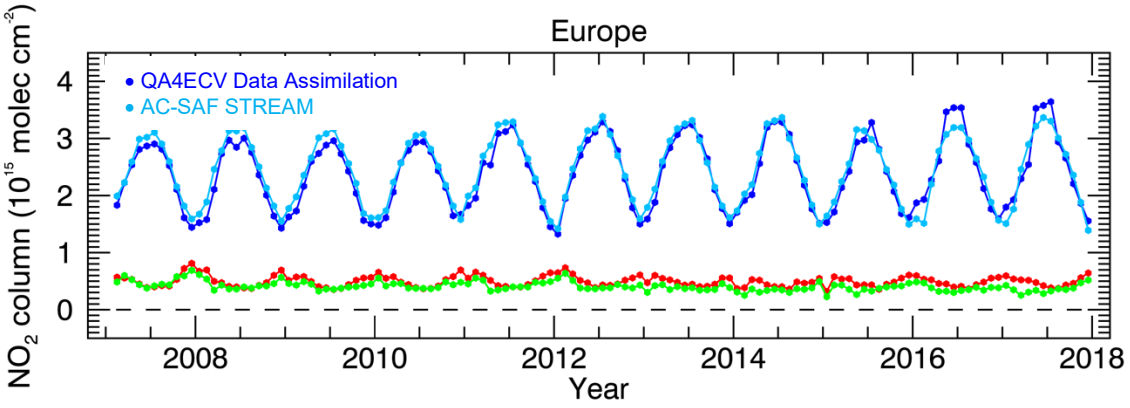

Figure 3-2: Timeseries of stratospheric and tropospheric NO_2 over Europe derived with the data assimilation and STREAM approaches for GOME-2A. Tropospheric NO_2 column values (indicated in red and green) have been divided by a factor of 4.

Data assimilation in TM5-MP

The L2 retrievals at KNMI use data assimilation of NO_2 slant columns in the TM5-MP chemistry transport model (Williams et al., 2017). This system incorporates observed information on NO_2 slant columns, clouds, and estimates of surface reflectivity to update the TM5-MP simulation of the 3-D global NO_2 distribution in such a way that the model simulation of stratospheric NO_2 comes in close agreement with the satellite observations, especially over regions with background levels of tropospheric NO_2 that are dominated by stratospheric NO_2. The assimilation scheme is based on the Kalman-filter technique, in which the TM5-MP model state is adjusted towards the observations, providing a new analysis of the model state for every orbit. For a detailed description of the Kalman filtering, see Eq. (1) and Figure 1 in Dirksen et al. (2011), and recent developments are described in van Geffen et al. (2022). Because satellite observations over pristine regions with low amounts of tropospheric NO_2 receive more weight, the filtering approach leads to relatively strong forcing of the simulated stratospheric NO_2 concentrations towards the satellite observations and will result only in marginal adjustment of the simulated tropospheric NO_2 field over polluted regions.

STREAM

The L2 retrievals at DLR use the STRatospheric Estimation Algorithm from Mainz (STREAM) method, developed by Beirle et al. (2016). This an improved modified reference sector method. A reference sector method has shortcomings in larger uncertainties over polluted areas since this uses measurements over clean regions with assumptions of longitudinally invariable stratospheric NO_2 columns and of negligible tropospheric NO_2 abundance (e.g. Boersma et al. (2004)). Instead of binary masks based on arbitrary thresholds, STREAM applies a weighted convolution scheme where cloudy observations are given a high weight and polluted observations are given low weight. The STREAM method has been adapted to GOME-2 measurements by calculating weighting factors for each satellite pixel to define the contribution of initial total columns to the stratospheric estimation based on a tropospheric NO_2 climatology and the GOME-2 cloud product (Liu et al., 2019).

Table 3-3: Overview of stratospheric NO_2 estimation settings for morning sensors.

	GOME	SCIAMACHY	GOME-2A	GOME-2B	GOME-2C
Method	Data assimilation	Data assimilation	STREAM	STREAM	STREAM
Use of CTM	Yes	Yes	No	No	No
Spatial convolution	No	No	Yes	Yes	Yes
Accounts for diurnal cycle in stratospheric NO_2	Yes	Yes	No	No	No
Correction for residual tropospheric contribution to NO_2 SCD	Yes	Yes	No	No	No

3.1.5. Air mass factor and tropospheric NO_2 column calculation

The tropospheric NO_2 algorithms use as default pre-calculated air mass factor look-up tables to convert slant columns into meaningful vertical columns (Lorente et al., 2017). The AMF (M) is the ratio of the slant column density of the absorbing gas along the (slant) optical path from the Sun to the satellite and the vertical column density above the surface area (pixel) the satellite is viewing. The tropospheric air mass factor follows from the ratio of the slant column density and vertical column density modelled with a radiative transfer model:

$$M_{tr} = \frac{N_{s,tr}}{N_{v,tr}} \qquad \textbf{Eq. 3-2}$$

The tropospheric air mass factor depends on the vertical profile of the trace gas and can be written as (Palmer et al. (2021); Eskes and Boersma (2003)):

$$M_{tr} = \frac{\sum_l m_l n_l c_l}{\sum_l n_l} \qquad \textbf{Eq. 3-3}$$

With m_l the altitude-dependent AMFs or bob-AMFs describing the vertically resolved sensitivity to NO_2 in layer l, $n_l$the vertical column density in layer l, and c_l the temperature correction term discussed in section 3.1.3. The summation in Eq. 3-3 takes place over all vertical layers in the troposphere. The altitude-dependent AMFs depend on retrieval parameters, including the satellite viewing geometry, as well as the forward model parameters surface albedo (a_s), surface pressure (p_s), (effective) cloud fraction (f_{cl}), and (effective) cloud pressure (p_{cl}), so M_{tr} can be written as a function of the set of forward model parameters $(a_s, p_s, f_{cl}, p_{cl}, \boldsymbol{n})$ with $\boldsymbol{n}$ a vector indicating the a priori tropospheric vertical profile.

Altitude-dependent AMFs

The altitude-dependent AMFs, or vertical sensitivities, have been calculated with a radiative transfer model by including a small, optically thin amount of NO_2 to the model atmosphere layer l for an atmosphere that is otherwise devoid of NO_2. The value for m_l is then given by ratioing the excess NO_2 slant column to the vertical column added to that layer ($m_l = \delta N_{s,l}/\delta N_{v,l}$). The radiative transfer model atmosphere does not include aerosols and describes the Earth's surface as a Lambertian reflector.

The altitude-dependent AMFs for the GOME, SCIAMACHY, OMI, and TROPOMI retrievals have been calculated with the Doubling-Adding KNMI (DAK) radiative transfer model (De Haan et al. (1987); Stammes et al. (2001)) version 3.2 at 437.5 nm, which includes a pseudo-sphericity correction, and a posterior correction against the full-sphericity model McArtim to better account for extreme viewing geometries (Boersma et al., 2018). Altitude-dependent AMFs for the GOME-2 retrievals have been generated by the VLIDORT radiative transfer model at 461 nm. The altitude-dependent AMFs are stored as a function of pre-define surface albedo, terrain height, solar zenith angle, viewing zenith angle, relative azimuth angles, and layer-height. Then, with the best available quantitiative information on the values of these parameters, altitude-dependent AMFs for the clear-sky situation and for the coudy-sky portion of a pixel (if present) are obtained by multi-dimensional interpolation in the look-up table. Quantities and reference points in the AMF look-up table calculated with DAK can be found in Table 4 in van Geffen et al. (2022).

Correction for cloud cover

It is important to account for the effect of clouds when calculating tropospheric AMFs in the presence of clouds. We calculate AMFs in (partly) cloudy situations via the independent pixel approximation (IPA, Martin et al. (2002)):

$$M_{tr} = (1 - w)M_{clear} + wM_{cl} \qquad \textbf{Eq. 3-4}$$

with w the the cloud radiance fraction (the portion of radiance coming from the cloudy part of the pixel):

$$w = \frac{f_{cl}I_{cl}}{R} = \frac{f_{cl}I_{cl}}{f_{cl}I_{cl}+(1-f_{cl})I_{clear}} \qquad \textbf{Eq. 3-5}$$

where I_{cl} is the radiance coming from the cloudy part of the pixel, I_{clear} the radiance from the clear part of the pixel, and the R total scene radiance. M_{clear} represents the clear-sky (tropospheric) AMF, and M_{cl} the cloudy-sky (tropospheric) AMF. The main motivation for using Eq. 3-4 to calculate the tropospheric AMF is that very few pixels are completely cloud-free, especially for the historical sensors. The relevant physical effects, reduced sensitivity to NO_2 below the cloud level ('screening') and enhanced sensitivity to NO_2 above the cloud ('albedo effect') are explicitly accounted for in this independent pixel approximation. The

cloud radiance can be determined from the radiance in the NO_2 fit window, or via the analytical approach of Vermote and Tanre (1992), using the effective cloud fraction f_{cl} from the cloud retrieval process for the sensor of interest.

Table 3.4 summarizes the selection of information sources for ancillary data (or forward model parameters) on the atmospheric state needed for each pixel to calculate the tropospheric AMF M_{tr} via the recipe of Eq. 3-2 - Eq. 3-5 above.

To allow for future accounting for the viewing angle dependency of surface albedo, the GOME-2 DLER dataset (Tilstra et al., 2021) was adopted. This dataset is derived by dividing the GOME-2 orbit swath into five segments and retrieving the traditional surface LER for each segment based on the data from the respective part of orbit swath. The GOME-2 DLER dataset improves the underestimation of the surface albedo on the western side of the GOME-2 orbit and increases AMFs by up to 15 % in polluted regions compared to the previous GOME-2 surface LER climatology (Liu et al., 2020).

The NO_2 retrieval is affected by the presence of clouds with high clouds shielding underlying parts of the atmosphere and low clouds contributing enhancements in NO_2 absorption due to multiple scattering and albedo effects. To account for cloud effects in GOME-2 NO_2 retrieval, cloud corrections are applied using the OCRA/ROCINN cloud parameters (Lutz et al, 2016; Loyola et al, 2018). During the Round Robin exercise, we compared the impact of cloud correction on the GOME-2 AMF using OCRA/ROCINN and FRESCO v7 for the GOME-2A mission period. Generally, cloud corrections from both OCRA/ROCINN and FRESCO are similar. However, cloud corrections using cloud parameters from OCRA/ROCINN result in up to 10% higher tropospheric NO_2 columns in polluted regions (Europe), reflecting higher OCRA/ROCINN cloud heights leading to a stronger 'screening effect' in the AMF calculation, as shown in Figure 3-3. For clean areas, the difference in the impact on the cloud corrections between the two cloud products is relatively small, ~5 %.

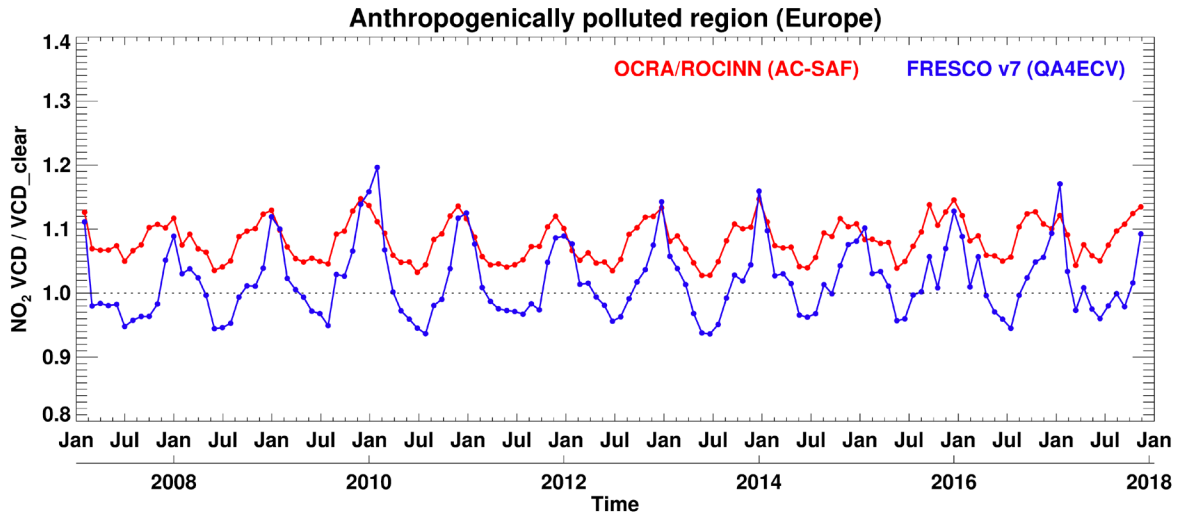

Figure 3-3: Time series of the ratio of total tropospheric NO_2 vertical column to clear-sky tropospheric NO_2 vertical column retrieved using the OCRA/ROCINN and FRESCO v7 cloud products for GOME-2A over Europe.

Table 3-4: Selected settings for forward model parameters used in the calculation of tropospheric NO_2 AMFs in the ESA CCI ECV Precursor project for the morning sensors.

Forward model parameter	GOME	SCIAMACHY	GOME-2A	GOME-2B	GOME-2C
Surface albedo	GOME-2 DLER v4 MIN	GOME-2 DLER v4 MIN	GOME-2 DLER v4 MIN	GOME-2 DLER v4 MIN	GOME-2 DLER v4 MIN
Surface pressure	ECMWF/DEM	ECMWF/DEM	GTOPO30	GTOPO30	GTOPO30
Cloud fraction	FRESCO v7/v8	FRESCO v7/v8	OCRA	OCRA	OCRA
Cloud pressure	FRESCO v7/v8	FRESCO v7/v8	ROCINN	ROCINN	ROCINN
Cloud albedo	0.8	0.8	ROCINN	ROCINN	ROCINN
A priori NO_2 profile	TM5-MP	TM5-MP	TM5-MP/CAMS	TM5-MP/CAMS	TM5-MP/CAMS

Table 3-5 summarizes the selection of information sources for ancillary data (or forward model parameters) on the atmospheric state needed for each pixel to calculate the tropospheric AMF M_{tr} via the recipe of Eq. 3-2 - Eq. 3-5 above for OMI and TROPOMI. For OMI, several changes have been made relative to the OMI QA4ECV approach, mostly to make the OMI NO_2 retrieval as consistent as possible with the operational TROPOMI retrieval. This includes the cloud fraction and cloud radiance fraction now taken from the NO_2 spectral window at 440 nm instead of O_2-O_2 continuum near 477 nm. A notable but unavoidable difference, however, is that for OMI, cloud pressures are retrieved from the O_2-O_2 absorption signature, which has proved to be less sensitive to low clouds than FRESCO.

One innovative aspect in the OMI and TROPOMI NO_2 retrievals that will be used in the ESA CCI ECV Precursor project is that the cloud products used provide (1) an effective cloud fraction and cloud pressure, but also (2) a scene albedo and scene pressure assuming that the cloud fraction is zero. When snow/ice flags, or sunglint flags are up, option (2) may be selected to calculate the AMF and ultimate tropospheric column. For example, if the scene pressure retrieved for a pixel is close to the reported ECMWF surface pressure, the scene is often brighter than indicated by the surface albedo climatology, because of sudden snowfall, or sunglint. Riess et al. (2022) showed that accurate tropospheric AMFs can be calculated with a cloud fraction of zero, and a surface albedo and effective surface pressure retrieved by the cloud retrieval.

Table 3-5: Selected settings for forward model parameters used in the calculation of tropospheric NO_2 AMFs in the ESA CCI ECV Precursor project for the afternoon sensors.

Forward model parameter	OMI	TROPOMI
Surface albedo	OMI LER MIN	S5P DLER MIN
Surface pressure	ECMWF/DEM	ECMWF/DEM
Cloud fraction	NO_2 fitting window	NO_2 fitting window
Cloud pressure	O_2-O_2	FRESCO-wide
Cloud albedo	0.8	0.8
A priori NO_2 profile	TM5-MP	TM5-MP

3.1.6. Information content and uncertainty estimate

Table 3-6 summarizes the assessment of the main contributions to the overall uncertainty budget on tropospheric NO_2 retrieval within this project. These uncertainties should be interpreted as representative of typical single-pixel uncertainties for retrievals over polluted regions encountered by users. Expressions for systematic or structural uncertainty are under investigation and will be provided in cycle 2 of the project.

Table 3-6: Estimation of the uncertainty contributions to the overall, per-pixel tropospheric NO_2 column uncertainty over polluted regions.

Uncertainty contribution	Random	Systematic
From NO_2 slant column ($\frac{\sigma_{N_S}}{M_{tr}}$)	0.4-0.8×10^{15} molec. cm^{-2}	< 1.0×10^{15} molec. cm^{-2}
From stratosphere ($\frac{\sigma_{N_{S,strat}}}{M_{tr}}$)	0.2×10^{15} molec. cm^{-2}	< 0.5×10^{15} molec. cm^{-2}
From tropospheric AMF ($\frac{\sigma_{N_S}}{M_{tr}}$)	20-35% (sensor dependent)	TBD
Approximation for σ_{N_v}	$\sigma_{N_v} = 0.5 \times 10^{15} + 0.3N_v$	TBD

3.2. Formaldehyde (L2-HCHO)

We provide here only a short description of the L2 HCHO DOAS retrieval. Extended descriptions are provided in De Smedt et al. (2018) (QA4ECV), De Smedt et al. (2021) (TROPOMI) and Valks et al. (2019) (GOME-2 AC SAF). Within the CCI+ ozone precursors project, the settings of the L2 retrieval algorithm have been updated with the aim to further improve the consistency between the sensors, to include the conclusions of the round robin study (PVASR report)[RD-14], and to include more recent auxiliary datasets. The settings for each step of the algorithm and for each sensor are summarized in sections 3.2.2, 3.2.3 and 3.2.4, and in the corresponding tables.

3.2.1. Flow diagram of the L2 retrieval algorithm

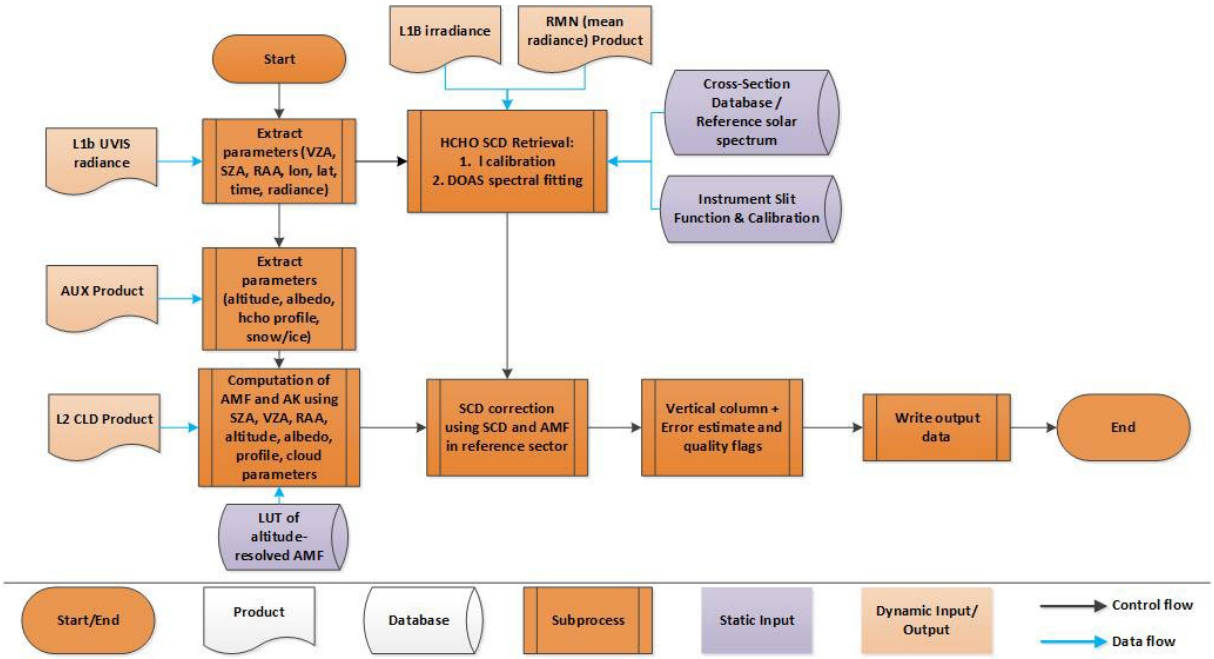

Figure 3-4: Flow Diagram of the DOAS retrieval algorithm for HCHO.

Figure 3-4 shows the flow diagram of the L2 HCHO DOAS retrieval algorithm. The HCHO slant column (N_s) fit is performed in the UV, and the relevant absorption cross-section data as well as instrumental characteristics are used as input. An average of radiances selected in a remote sector is calculated to obtain a reference spectrum for the DOAS fit. Subsequently, to convert the slant column to a vertical column (N_v), an air mass factor (M) that accounts for the average light path through the atmosphere is calculated. For this purpose, several auxiliary data are read from external sources: cloud cover data, topographic information, surface albedo, and the a priori shape of the vertical HCHO profile in the atmosphere. Additional background normalization is required in the case of weak absorbers such as formaldehyde. Before converting the slant columns N_s into vertical columns N_v, remote background values of N_s are normalized to compensate for unknown offsets ($N_{s,0}$), and background vertical columns derived from a CTM is added ($N_{v,0}$).

The final HCHO vertical column (**N_v**) is obtained using the following equation:

$$N_v = \frac{N_s - \overline{N_{s,0}}}{M} + \overline{N_{v,0}} = \frac{N_s - \overline{N_{s,0}} + \overline{M_0} \times \overline{N_{v,0,CTM}}}{M} \quad \text{Eq. 3-6}$$

The main outputs of the different steps of algorithm are:

1. The slant column density (N_s): see section 3.2.2.
2. The air mass factor (M): see section 3.2.3.
3. The mean values used for the reference sector correction ($\overline{N_{s,0}}$, $\overline{N_{v,0CTM}}$, and $\overline{M_0}$): see section 0.

Complementary product information includes the averaging kernel, the error on the total column, and quality assurance values.

3.2.2. Slant Columns

The fit of the slant columns (N_s) is performed in the UV part of the spectra (see Table 3-7 for details). All cross sections are convolved with the instrumental slit functions (for every row separately for OMI and TROPOMI). The TROPOMI slit functions have been adjusted once after launch and the cross-sections have been pre-convolved. For OMI, GOME-2, SCIAMACHY and GOME, the slit functions are adjusted daily and the cross sections are convolved online. The DOAS reference spectrum is updated daily with an average of Earth radiances measured in the equatorial Pacific region. The fit therefore results in a differential slant column, corresponding to the HCHO excess over sources compared to the remote background. Details are provided in Table 3-7.

Table 3-7: Settings used for DOAS spectral fitting for the different satellite instruments.

Sensor / Settings	TROPOMI	OMI	GOME-2	SCIAMACHY	GOME
Level 1 version	Collection 3	OML1BRUG.003	R 5.12	Y 8.02	5.1
Wavelength calibration	325-360 nm Pre convolution with adjusted FM IRSF, per row	325-360 nm Online convolution with adjusted slit function from PFM IRSF, per row	325-360 nm Online convolution with adjusted slit function from PFM IRSF	325-360 nm Fit of the slit function: Gaussian line shape	
Solar Atlas	Chance and Kurucz, 2010				
Fitting intervals	328.5-359 nm				328.5-346 nm
Reference spectrum	Daily average of radiances, per detector row.		Daily average of radiances, per VZA bins.		Daily average of radiances, per pixel type (0,1,2,3).
Reference sector	Lat: [-5° 5°], Long: [180° 240°]	Lat: [-15° 15°], Long: [150° 250°]			
Cross-sections	HCHO: Meller and Moortgat (2000), 298K O_3: Serdyuchenko et al. (2013), 223 + 243K NO_2: Vandaele et al. (1998), 220K BrO: Fleischmann et al. (2004), 223K O4: Thalman et al., 2013, 293K Ring: Generated following Chance et al, 1997. Non linear O_3 terms: generated internally based on O3223. Calculated from the Taylor expansion of the wavelength and the O3 optical depth (Puķīte et al., 2010).				
Additional cross-sections			Polarisation_eta, polarisation_zeta, Pseudo_east_west		undersampling
Polynomial	Order 5				

Intensity offset	Linear offset (1/reference spectrum)	
Shift / stretch	Non-linear / First order	
Iterative Spike Removal	Tolerance factor 5, maximum iteration 3	Tolerance factor 3, maximum iteration 3

3.2.3. Air Mass Factors

For optically thin absorbers, the tropospheric AMF (M) can be expressed as the sum of the altitude dependent air mass factors (m_l) weighted by the partial columns (n_{al}) of the a priori vertical profile in each vertical layer l, from the surface up to the tropopause index (lt) (Palmer et al., 2001):

$$\boldsymbol{M = \frac{\sum_{l=1}^{l=lt} m_l(\lambda, \theta_0, \theta, \varphi, A_s, p_s, f_c, A_{cloud}, p_{cloud}) n_{al}(lat, long, time)}{\sum_{l=1}^{l=lt} n_{al}(lat, long, time)}} \qquad \textbf{Eq. 3-7}$$

where A_s is the surface albedo, p_s is the surface pressure, while f_c, A_{cloud} and p_{cloud} are respectively the cloud fraction, cloud albedo and cloud pressure. The AMF calculation assumes Lambertian reflectors for the ground and the clouds and makes use of pre-calculated altitude dependent air mass factors look-up-tables. This look up table has been created using the VLIDORT 2.8 radiative transfer model (Spurr et al., 2008a) at a 340 nm, wavelength representative for the retrieval interval. For each pixel, m_l is computed by linear interpolation of the LUT at the a-priori profile pressure grid and using the auxiliary data sets described in Table 3-8. The AMF calculation module is almost identical to the one used for the operational retrieval of HCHO columns from TROPOMI, and the reader is referred to the S5P HCHO ATBD for more detailed information (De Smedt et al., 2018, 2021).

Table 3-8: Input used for AMF calculation for the different satellite instruments.

Sensor / Settings	**TROPOMI**	**OMI**	**GOME-2**	**SCIAMACHY**	**GOME**
Surface albedo	TROPOMI DLER v2.1 at 340 nm(Tilstra, 2023)				
Cloud product	OCRA-ROCINN collect. 3	OMCLDO2 v2.0 Collect. 4	AC SAF OCRA-ROCINN	FRESCO version SC-v7	FRESCO version GO-v7
Cloud correction	Baseline: cloud filtering, no cloud correction (VCD clear, AMF clear, AK clear). Optional: cloud correction based on the independent pixel approximation and a Lambertian reflector cloud model, no cloud correction for CF *<10% (CF=0) (VCD, AMF, AK).				
A priori profiles	CAMS reanalysis, 3h time step (Innes et al., 2019)				CAMS reanalysis, 3h time step, climatology.

*FOR OCRA/ROCINN, it is defined as an effective cloud fraction with a cloud albedo of 0.8.

3.2.4. Background correction

Retrieved HCHO slant columns can present large offsets depending on minor changes in the fit settings and minor instrumental spectral inaccuracies. Resulting offsets are generally global but also show particular dependencies, mainly with detector row or VZA (across track) and with latitude (along track). Offsets can also present a time dependency, resulting from instrumental degradation. The background correction is based on the assumption that the

HCHO column observed over remote oceanic regions (Pacific Ocean) is only due to methane oxidation. The natural background level of HCHO is well estimated from chemistry model simulations of CH_4 oxidation.

The correction includes two steps:

1. a destriping correction in the Equatorial Pacific (refence sector 1, dimension: ground pixels/SZA bins). Offset correction factors are determined for each ground pixel or SZA bin as the median of all slant columns ($N_{s,0}$) falling into to the Equatorial Pacific. Data selection is based on the residuals from the DOAS fit and on the cloud fraction.
2. a latitudinal-bias correction in the entire Pacific Ocean (reference sector 2, dimension: latitude bins). The second correction relies on latitude-dependant polynomials, calculated using the destriped slant columns averaged in latitude bins in the entire Pacific Ocean, independently of their cross-track position. An additional data selection, based on the destriped slant column value in the reference sector is applied in order to exclude grid cells with real emissions (ex: from Alaska fires).

At the end of these steps, the correction factors are subtracted from all SCDs (N_s) of all observations worldwide, so that in the reference sector, the median background corrected slant columns are close to zero. To the corrected HCHO slant columns, the background HCHO columns from the model are added (see equation 3-6).

In practice, the corrections are calculated using 2-dimensional arrays (dimension: latitude bins x ground pixels/SZA bins) updated on a daily basis and providing the median values of the observations falling into the entire reference sector (reference sector 2) for the following variables:

- $\overline{N_{s,0}}$: mean HCHO slant column density in the reference sector.
- $\overline{M_0}$: mean clear air mass factor in the reference sector.
- $\overline{N_{v,0,CTM}}$: mean model HCHO vertical in the reference sector. The model columns are derived from the a priori profiles.

Details of the reference sector limits, array dimensions and selection criteria are provided in Table 3-9.

Table 3-9: Background correction settings for the different satellite instruments.

Sensor / Settings	TROPOMI	OMI	GOME-2	SCIAMACHY	GOME
refence sector 1	Lat: [-10° 10°], Long: [180° 240°]				
reference sector 2	Lat: [-90° 90°] Long: [180° 240°]				
Acrosstrack dim. in ref. sector 1	450 ground pixels	60 ground pixels	SZA bins: TBD	SZA bins	3 pixel types (east, center, west)
Along track dim. in ref. sector 2	36 (5° latitude bin)				
RMS threshold	$3\overline{RMS}$				
CF threshold	0.5				
SZA threshold	70				

Threshold of the destriped SCD for applying the zonal correction: 2.5e16
Latitudinal normalization polynomial degree: 8

3.2.5. Error estimate, averaging kernels and qa_values

Many factors contribute to the retrieved HCHO tropospheric column uncertainty. The random uncertainty of the final HCHO columns is dominated by the error of the fitted slant columns (instrument dependent). The systematic uncertainty is dominated by error in air mass factor calculations, resulting from uncertainties on a priori information such as a priori profile shapes, clouds or surface albedo (mostly not instrument dependent). We refer to the End-to-End ECV Uncertainty Budget (E3UB) [RD-11] for a detailed description of the implementation of error modules in the L2 retrievals and an analysis of the error budget for HCHO.Averaging kernels and quality assurance values

Retrieved satellite quantities always represent a weighted average over all parts of the atmosphere that contribute to the signal observed by the satellite instrument. The DOAS total column retrieval is implicitly dependant on the a priori tracer profile n_a. Indeed, the radiative transfer calculation accounts for the sensitivity of the measurement to the HCHO concentrations at all altitudes and the sensitivities are weighted with the assumed a priori profile shape to produce the vertical column. The averaging kernel (AK) is proportional to this measurement sensitivity profile, and provides the relation between the retrieved column N_v and the true tracer profile x (Rodgers, 2000; Rodgers and Connor, 2002):

$$\boldsymbol{N_v - N_{v,a} = AK.(x^{pc} - n_a^{pc})} \qquad \textbf{Eq. 3-8}$$

where the profiles are expressed in partial columns (*pc*). For total column observations of optically thin absorbers DOAS averaging kernels are calculated as follows (*Eskes and Boersma*, 2003):

$$\boldsymbol{AK(l) = \frac{m(l)}{M}} \qquad \textbf{Eq. 3-9}$$

where $m(l)$ is the altitude-resolved air mass factor and M is the tropospheric air mass factor (see Equ. 3.7). The air mass factor and therefore the retrieved vertical column, depends on the a priori profile shape, in contrast to the altitude-resolved air mass factor which describes the sensitivity of the slant column to changes in trace gas concentrations at a given altitude and does not depend on the a priori profile in an optically thin atmosphere. From the definition of AK, we have $N_{v,a} = AK.n_a^{pc}$.

Quality assurance values (*qa_value*) are provided for every pixel.

The qa_value is a variable ranging from 0 (error) to 1 (good quality). It quantifies the quality of the main HCHO vertical column product. The qa_value is based on the qa_value calculation rule described in Table 3-10.

For valid pixels, the main quality parameter is the cloud (effective) fraction. Other quality parameters decrease the *qa_value* below the recommended threshold. For general

applications, pixels are considered of good quality for qa_value above 0.5. All quality criteria are met and cloud-covered pixels are filtered out (CF<0.4). Two additional thresholds are defined. One stricter filtering can be applied using only qa_value>0.75 (CF<0.2). This stricter filtering is designed for air quality applications and the simultaneous use of HCHO and NO_2 observations. Another threshold is defined for qa_value>0.35 (CF<0.6). This more relax filtering is designed for fire scene observations and allows for the selection of more pixels with large HCHO columns in fire scenes. Users should be warned that cloud contamination, and related errors, are therefore more important using this filter.

An additional filtering based on the interquartile interval* is performed on the vertical columns passing the main quality criteria (qa_value >0.5) to remove statistical outliers.

Table 3-10: Description of the HCHO qa_value definition

Description	***qa_value***
No error / no warning	1
Sun glint scene warning	0.95
South Atlantic Anomaly (SAA) warning	0.90
Effective cloud fraction<=0.2	0.75
Effective cloud fraction<=0.4	0.50
Effective cloud fraction<=0.6	0.35
Effective cloud fraction>0.6	0.25
Air mass factor clear M_{clear}<0.1	0.21
Air mass factor M<0.1	0.17
Pixel contains snow/ice	0.13
Surface albedo A_s>0.8	0.11
Solar Zenith Angle >75°	0.08
Fit residual RMS>max_rms (3*mean(RMS))	0.05
Background correction error	0.02
Air mass factor error	0.01
Fit of slant column error	0.00
Statistical outliers: (qa_value>=0.50) and (N_v<w1*)	0.4

* Statistical outlier calculation:

- q1=percentile(N_v [(qa_value>=0.50)] ,25)
- q3=percentile(N_v [(qa_value >=0.50)] ,75)
- iqr=q3-q1
- w1=q1-3*iqr

3.3. Sulfur dioxide (L2-SO_2)

3.3.1. Overview

The SO_2 algorithm relies on the two steps Covariance-Based Retrieval Algorithm (COBRA; Theys et al., 2021) to retrieve sulphur dioxide vertical columns from satellite nadir UV hyperspectral measurements. First, the measured top-of-atmosphere radiances are analyzed and yield the slant columns (SCD, or the integrated concentration along the light path). In a second step, a radiative transfer calculation of air mass factors (AMF) is performed to convert the SCD into the VCD output (VCD=SCD/AMF). A diagram illustrating the algorithm modules is given in Figure 3-5.

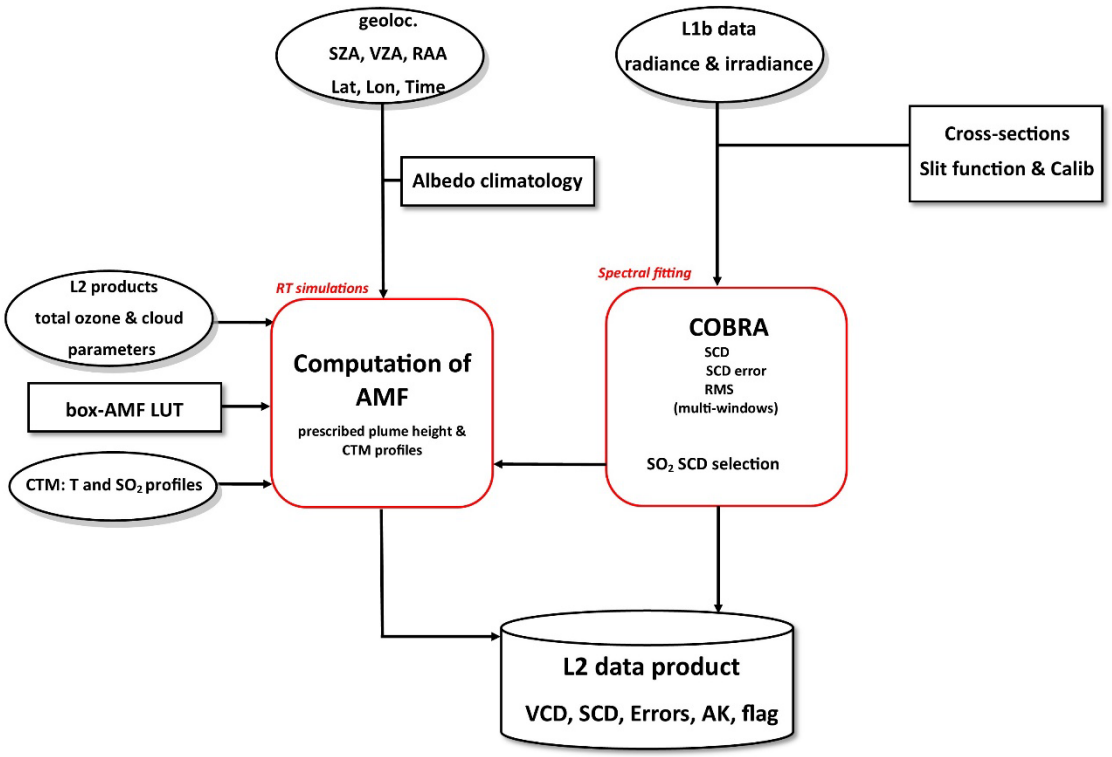

Figure 3-5: Flow diagram of the SO_2 column retrieval algorithm.

The radiance and irradiance data are read from the L1b files, along with geolocation data as pixel coordinates and observation geometry. The relevant absorption cross sections data as well as characteristics of the instrument like slit function and wavelength calibration parameters are used as input of the spectral fitting module. The SO_2 fit is performed using COBRA in multiple fitting windows, characterized by different SO_2 absorption strengths. Depending on the retrieved columns amounts in the different fitting windows, a selection of the final SCD is performed. This step is to avoid saturation, ensuring that the results are valid for a wide range of SO_2 column amount. Subsequently, the slant column is converted to a vertical column through division by an air mass factor which accounts for the average light path through the atmosphere. To do so, altitude-resolved air mass factors are extracted from a pre-computed look-up-table. The AMF is computed for SO_2 profiles from a chemical

transport model as well as for box profiles with prescribed SO_2 plume heights, representative of volcanic scenarios. The AMF module also includes calculation of errors and column averaging kernels. Note that the AMF module is similar to the one used for TROPOMI operational SO_2 retrievals (Theys et al., 2017, 2023).
The next subsections give details on the two algorithmic steps (spectral fitting and radiative transfer calculations), as well as an overview of the input data needed for the retrievals.

3.3.2. Algorithm description

Spectral fitting

In a preparatory step, we extract the intensities over the wavelength range 310-390 nm and compute the total measured optical depth y = - log (I / I_o), which is the logarithmic ratio of the wavelength calibrated measured intensity (I) and the solar intensity spectrum (I_o). For the wavelength calibration, we use the same approach as for the TROPOMI operational SO_2 algorithm (as described in Theys et al., 2017), although the exact settings depend on the satellite instrument considered.

We assume the measurement vector (y) can be linearized around a background SO_2-free spectrum $\bar{y}$:

$$y = \bar{y} + k.SCD + \epsilon_{bg} + \epsilon \qquad \textbf{Eq. 3-10}$$

with ϵ_{bg} being the uncertainty on the SO_2-free spectrum, and ϵ is the measurement noise. The SO_2 contribution to the measured spectral optical depth is the product of the instrument slit convolved absorption cross-section vector *k* and the SO_2 slant column density *SCD* (in molecules/cm²).

The basic principle of the method is to consider all contributions to the difference $(y - \bar{y})$ other than SO_2 as an error term (ϵ_{bg} + ϵ) with a Gaussian distribution. If one can define an ensemble Y of N measured spectra, representative of the total (ϵ_{bg} + ϵ) variability, and characterized by a mean measurement vector $\bar{y}$ and a covariance matrix *S*:

$$S = \frac{1}{N-1}.\sum_{i=1}^{N}(y_i - \bar{y})(y_i - \bar{y})^T \qquad \textbf{Eq. 3-11}$$

then the solution of the problem writes as:

$$\widehat{SCD} = (k^T S^{-1} k)^{-1} k^T S^{-1} (y - \bar{y}) \qquad \textbf{Eq. 3-12}$$

It follows that the retrieval error on the SCD is given by:

$$\widehat{SCD}_{err} = \chi.\sqrt{(k^T S^{-1} k)^{-1}} \qquad \textbf{Eq. 3-13}$$

with χ being the normalized root-mean-square, i.e.:

$$\chi^2 = \frac{1}{N_\lambda - 1} . (\Delta y^T S^{-1} \Delta y) \qquad \textbf{Eq. 3-14}$$

where $\Delta y = y - \bar{y} - k.\widehat{SCD}$ (residual) and N_λ being the number of wavelengths in the fitting interval. This variable evaluates the fit quality and is typically close to 1, except for conditions of bad fit quality (χ>>1).

Fundamentally, COBRA generalizes the measurement error covariance matrix used in Optimal Estimation Methods (OEM; Rodgers, 2000) by incorporating geophysical background spectral variability (including all cross-correlations), variability from the atmosphere or induced by instrumental changes. A remarkable feature of COBRA is its simplicity. The SCD retrieval in Eq. 3-12 reduces to a simple dot product between the $y - \bar{y}$ residue and $k^T S^{-1}$ (skipping the normalization factor $(k^T S^{-1} k)^{-1}$); the target SCD is only the fit parameter, this is contrast to most other retrieval methods. Note that, in principle, the COBRA approach is applicable to any spectral fitting range. Here, the SO_2 SCD retrieval is performed in different fitting windows. There are differences depending on the satellite instrument used but, as a baseline, SCDs are typically retrieved from 310.5-326 nm (w1), 325-335 nm (w2) and 360-390 nm (w3). In the following, the slant column results in the respective windows are referred as SCDi (i=1,2,3). It should be noted that, in practice, a covariance matrix S (and mean spectrum $\bar{y}$) is associated specifically to each window, but the set of clean spectra Y used to construct the covariance matrices is common to all fitting windows.

Although simple in concept, the practical implementation for COBRA requires some caution. The main difficulty lies in the definition of the ensemble Y used to construct *S*. The reader is referred to Theys et al. (2021) for more detailed discussion on COBRA pro and cons. For the retrieval of SO_2, we have conducted several tests and come to the following general implementation choices (note that the settings are different for each sensor, see Table 3.1): the input spectra for the covariance matrix calculation are analyzed separately for each across-track position. We also treat each orbit/day individually. The data are first screened for solar zenith angles larger than 65°, and to cope with the latitudinal dependence, the data are divided into a number (from 3 to 6) of equal and non-overlapping along-track segments. For each segment, an initial covariance matrix *S* is derived for w1 (the most sensitive spectral range) and initial estimates of SO_2 slant columns (SCD1) are inverted through Eq. 3-12. To do so, the spectra with strong SO_2 absorption must be filtered out to avoid contamination of the initial covariance matrix. For this purpose, SO_2 SCD results from a simplified DOAS sub-module are used (see Table 3-11). In a second step, improved estimates of *S* and SO_2 SCDs are obtained iteratively by further removing SO_2 contaminated spectra from the ensemble Y. For this, we use the ratio of the SCD to its retrieval uncertainty (Eq. 3-12 and Eq. 3-13), referred to as the signal to noise ratio (SNR). A fixed SNR upper value of 1.5 is used for the filtering and the number of iterations is set to 5. Note that most pixels are SO_2-free, except in some rare cases of extended SO_2 plumes. A lower limit on the number N of SO_2-free spectra is set to 50. If this limit is reached, because of a major volcanic eruption for example, the SO_2 SCD retrieval for

the corresponding across-track position–segment pair falls back on the SCDs from the last iteration or ultimately the DOAS SCD results.

Table 3-11: Settings used for COBRA spectral fitting for the different satellite instruments used (preliminary).

	Satellite instrument			
	GOME/ERS2	**SCIAMACHY/ ENVISAT**	**OMI/AURA**	**TROPOMI/S5P**
Fitting intervals	313-326, 325-335nm	tbd	310.5-325, 325-335, 360-390 nm	310.5-325, 325-335, 360-390 nm
Covariance calculation	per day, per viewing angle (3), 3 segments	tbd	per orbit, per row (60), 3 segments*	per orbit, per row (450), 6 segments
DOAS pre-filtering	no	tbd	yes, from linear DOAS module. $SCD1_{doas}$<5DU & $SCD2_{doas}$<15DU	yes, from operational product. $SCD1_{doas}$<2DU & $SCD2_{doas}$<30DU (**)
Cross-sections†	SO_2: *Bogumil et al.*, 2003 (203K) for w1 & w2, *Hermans et al.* (2009, extrapolated at 203K) for w3. Other cross-sections and settings used in DOAS retrievals: see *Theys et al.*, 2017, 2023. For linear DOAS module: irradiance used as reference, fit of wavelength shift and squeeze according to Beirle et al. (2013), no SCD background correction.			

*Pixels affected by the row anomaly are filtered out. ** For rows 23-430. External rows: 3 DU, 40 DU, respectively. † All cross-sections are convolved using instrumental spectral response functions (row dependent in case of OMI and TROPOMI). Note: DU=Dosbon Unit (1 DU: 2.69×10^{16} molecules/cm^2).

The output results of the spectral fitting procedure described above, are SO_2 slant columns in three fitting windows (SCD1, SCD2 and SCD3). The next step is to combine the slant columns into a single SCD. For this, a set of transition criteria are used that are based on the measured SO_2 SCDs. The latter are summarized in Table 3-12.

Table 3-12: Criteria for selecting alternative fitting windows.

Window number	**w1**	**w2**	**w3**
Wavelength range	310.5 – 326 nm	325-335 nm	360-390 nm
Derived slant column	SCD1	SCD2	SCD3
Application	Baseline	SCD1 > 5 DU & SCD2 > 30 DU & SCD2> 2 x SCD1	w2 selected & SCD3 > 100 DU & SCD3 > 2 x SCD2

Radiative transfer calculations

The AMF simulates the trace gas concentration integrated along the complex photon path in the atmosphere, relative to the vertical path. Here, the AMF can be formulated (Palmer et al., 2001) by:

$$AMF = \int m'(p) \cdot s(p) \mathrm{d}p \qquad \textbf{Eq. 3-15}$$

with $m'=m(p)/C_{temp}(p)$, where m(p) is the so-called weighting function (WF) or pressure dependent air mass factor, C_{temp} is a temperature correction and s is the SO_2 normalized a-priori mixing ratio profile, as function of pressure (p).

The AMF calculation assumes Lambertian reflectors for the ground and the clouds and makes use of pre-calculated WF look-up-tables at suitable wavelengths (depending on the fitting window used). We note that the AMF calculation module is almost identical to the one used for the operational retrieval of SO_2 columns from TROPOMI, and the reader is referred to the S5P SO_2 ATBD for more detailed information (Theys et al., 2017, 2023). Here we limit the description to the differences compared to the operational S5P AMF calculation module.

In practice, the WF depends on observation geometry (solar zenith angle: SZA, line-of-sight angle: LOS, relative azimuth angle: RAA), total ozone column (TO3), scene albedo (alb), surface pressure (p_s), cloud top pressure (p_{cloud}) and effective cloud fraction (f_{eff}). The generation of the WF LUT has been done for a large range of physical parameters (as listed in Table 4 of Theys et al., 2017). For each pixel, the WF is computed by linear interpolation of the WF LUT at the a-priori profile pressure grid and using the auxiliary data sets described in Table 3-13. Finally, the AMF is calculated using Eq. 3-15.

Table 3-13: Input parameters used for AMF calculation and the for the different satellite instruments used (preliminary).

	Satellite instrument			
	GOME/ERS2	**SCIAMACHY/ ENVISAT**	**OMI/AURA**	**TROPOMI/S5P**
Total ozone column	tbd / CCI TO3 product	tbd / CCI TO3 product	OMSO2.003	S5P L2 SO_2 OFL+RPRO
Surface albedo*	OMI minLER 328, 376 nm (*Kleipool et al.*, 2008)	OMI minLER 328, 376 nm (*Kleipool et al.*, 2008)	OMI minLER 328, 376 nm (*Kleipool et al.*, 2008)	OMI/TROPOMI minLER 328, 376 nm (*Kleipool et al.*, 2008 ; *Tilstra*, 2023)
Clouds (product/cloud correction)**	FRESCOv7 (*Wang et al.*, 2008)/no	tbd/no	OMCLDO2.003/ no	OCRA-ROCINN (from S5P L2 SO_2 OFL+RPRO v3.2)/no
SO_2 profile shapes and temperature profiles	CAMSrea/ TM5 (tbd) +box profiles at 1,7,15km height	CAMSrea/ TM5 (tbd) +box profiles at 1,7,15km height	CAMSrea/ TM5 (tbd) +box profiles at 1,7,15km height	CAMSrea/ TM5 (tbd) +box profiles at 1,7,15km height

* Current baseline is to process only the scenes free of snow/ice (identified as such by a proper snow/ice flag).
** Cloud correction applied or not applied: total AMF or clear-sky AMF are used in the VCD calculation.

3.3.3. Information content and uncertainty estimate

Because exploiting the information content of the L2_SO_2 product is first a matter of data filtering, it requires some caution. To describe the quality of the retrieved SO_2 vertical column (and guide the users), a quality assurance value (qa_value) is assigned to each pixel. The quality assurance value is a numerical value with a range of [0 1], with the convention that a value <0.5 means that the pixel retrieval results should be discarded. The initial qa_value is 1 (full quality). For some conditions (e.g., in the presence of clouds) or when an error/warning flag is raised, the qa_value is reduced by a certain fraction. As a matter of fact, the qa_value calculation rule is instrument specific and, at the time of writing, it is not fully defined. In a next ATBD version, the calculation rule will be described in more detail but as a general rule, good quality results (qa_value>0.5) can only be obtained if all of the following conditions are fullfilled: AMF>0.15, -3.5 DU<VCD<10 DU, SZA<65, cloud fraction<0.3.

It should be emphasized that qa_value for SO_2 is only applicable to the VCD for the pollution scenario (based on model a-priori profiles). For volcanic cases, the retrievals are not as difficult as for boundary layer SO_2, especially for volcanic plumes above clouds, and it is difficult to assign a general quality flag for these cases. It is suggested that the users consider the SO_2 VCD assuming box profiles for volcanic cases.

Regarding the total uncertainty characterization, it is the subject of a different document (End-to-End ECV Uncertainty Budget). Table 3-14 summarizes the assessment of the main contributions to the global error budget on SO_2 retrieval from COBRA.

Table 3-14: Estimation of the error sources of the SO_2 COBRA retrieval (preliminary) for typical polluted conditions, at low/high SZA (latitudes). Blue and red fields indicate random (precision) and systematic (trueness) errors. Total errors are computed assuming all contributions are mutually uncorrelated.

Error source	Error on VCD	
	SZA=30°	SZA=60°
Instrument signal-to-noise	0.6 DU	1.2 DU
SO_2 absorption cross-section, spectral interferences +instrumental features	0.1 DU + 10%	0.2 DU + 15%
Surface albedo*	15%	15%
SO_2 Profile shape	20-50%	20-50%
Cloud correction	10%	10%
Cloud fraction	5%	5%
Cloud pressure	20%	20%
Aerosols (except in case of volcanic eruptions)	< 15%	< 25%
Structural (AMF)	15%	15%
Total random error	0.6 DU + 20%	1.2 DU + 20%
Total systematic error	0.1 DU + 45%	0.2 DU + 55 %
Total systematic error kernel	0.1 DU + 27%	0.2 DU + 35 %

*snow/ice free scenes

3.4. Glyoxal (L2-CHOCHO)

3.4.1. Overview

The glyoxal vertical column retrieval is based on the differential optical absorption spectroscopy (DOAS) algorithm for TROPOMI by Lerot et al. (2021) presented in Figure 3-6, and has been transferred to the OMI and GOME-2 instruments to obtain maximally consistent results from all sensors.

As a first step, the measured optical depth at top of atmosphere is fit against a set of known absorption spectra for glyoxal and other important absorbers in the same wavelength range, as well as pseudo absorbers which compensate for instrumental effects, in order to determine the glyoxal column density along the effective light path, or slant column density (SCD). In the next step, we divide the SCD by an air mass factor (AMF) in order to obtain a vertical column density (VCD). The AMF is calculated by modelling the radiative transfer through the atmosphere, considering each observation's viewing geometry and local surface albedo, for a model atmosphere based on an a priori vertical profile shape from a chemical transport model. An empirical correction is applied to the retrieved vertical columns to compensate for the effect of strong NO_2 absorption on the spectral fit. A final background correction to the resulting VCD's is compensates for systematic differences which arise from instrument calibration imperfections and viewing zenith angle (VZA) dependencies.

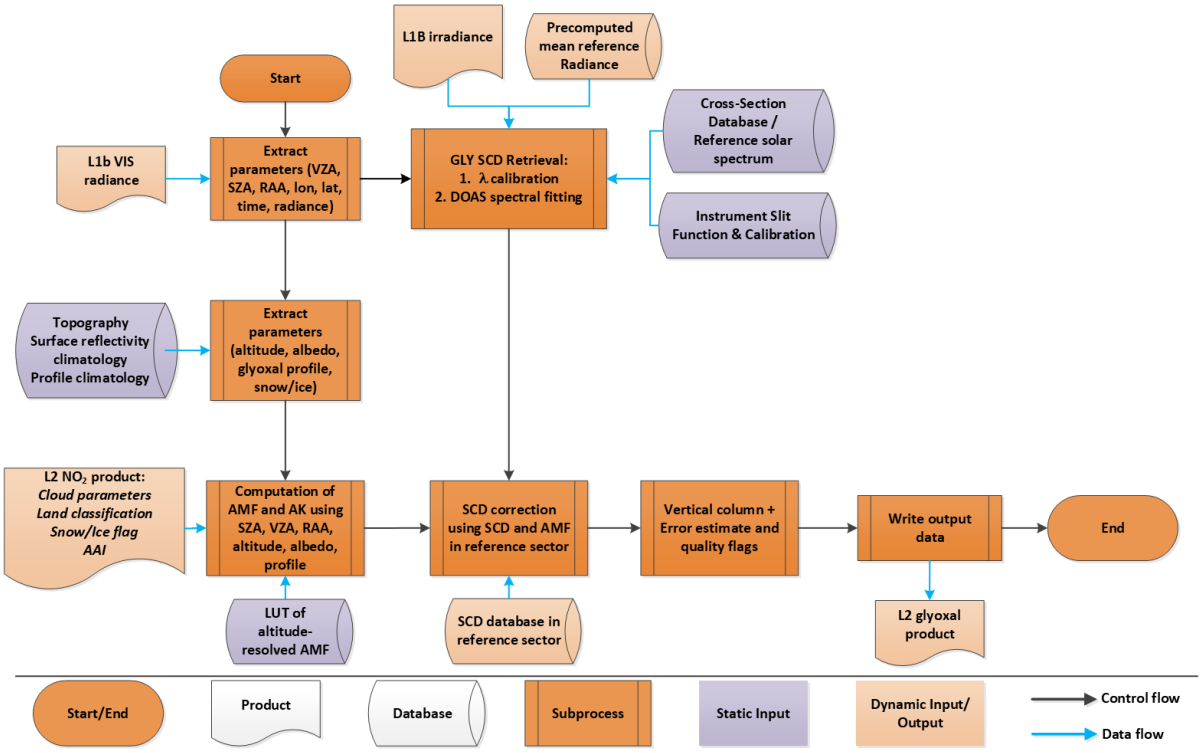

Figure 3-6: Glyoxal retrieval flowchart

3.4.2. Algorithm description

Spectral fitting

In order to minimize the effect of spectral interferences and instrumental limitations, the reference spectrum I_0 used in the DOAS fit for glyoxal is a daily mean radiance spectrum obtained from measurements over a region in the equatorial Pacific (typically 15°S -15°N and 150°-250°E, where the exact settings differ per instrument, see Table 3-15). A calibration procedure (Lerot et al., 2021; Danckaert et al., 2017) ensures that this refence spectrum is aligned with the wavelength grid of the cross sections used in the fit. For each observed radiance I, we then fit the atmospheric transmittance spectrum in a wavelength range of 435-460 nm, which includes the strongest glyoxal absorption bands, and has been found to work well for glyoxal retrievals for all 3 instruments (Barkley et al., 2017; Lerot et al., 2010; Alvarado et al., 2014; Chan Miller et al., 2014). A non-linear fitting procedure (Danckaert et al., 2017) is used to align the wavelength grid of the radiance I with that of the calibrated reference I_0. We then fit the optical depth against a set of cross sections σ_j and obtain slant column densities $N_{s,j}$ from the linear least squares solution of the following equation:

$$\ln\frac{I}{I_0}(\lambda) = \sum_j \sigma_j(\lambda) N_{s,j} + P(\lambda) + \epsilon \qquad \textbf{Eq. 3-16}$$

Here, the set of cross sections σ_j includes absorption spectra for glyoxal, O_3, NO_2 (at 220K and 294K to account for temperature dependence), $O_2 - O_2$ and water vapour. Absorption spectra are obtained from laboratory measurements and convolved to instrument resolution using the available data on the respective instrument spectral response function; see Table 3-16 for an overview. Additional cross sections are included to treat the effect of inelastic scattering (Ring effect) and intensity offsets in the spectra such as those caused by instrumental stray light. For the GOME-2 instruments, additional cross sections are included to compensate for polarization effects. For TROPOMI, a set of cross sections based on mean residual spectra is added to compensate for the effect of scene intensity heterogeneity (Richter, 2018). A polynomial $P(\lambda)$ of degree 3 is included to fit broad-band atmospheric absorption features.

Table 3-15: Selected pacific background region for daily reference radiance per instrument.

Instrument	Radiance reference region
TROPOMI	15°S – 15°N, 180°E – 240°E
OMI	15°S – 15°N, 150°E – 250°E
GOME-2 / METOP-A/B	15°S – 15°N, 180°E – 240°E
GOME-2 / METOP-C	20°S – 20°N, 150°E – 250°E

Table 3-16: Absorption cross sections

Species	Cross section
Glyoxal	Volkamer et al. (2005)
O_3	Serdyuchenko et al. (2014), 223K
NO_2	Vandaele et al. (1998), 220K and 294K
$O_2 – O_2$	Thalman and Volkamer (2013), 293K
H_2O (water vapour)	Rothman et al. (2013), 293K

Radiative transfer calculations

To compute the AMF, we rely on the formulation from (Palmer et al., 2001), which decouples the radiative transfer computation from the absorber's a priori atmospheric profile shape:

$$\mathrm{AMF} = \sum_{j=1}^{N} m_j s_j \qquad \textbf{Eq. 3-17}$$

Where the atmosphere has been discretized into N vertical layers, m_j is the box air-mass factor or weighting function for layer j, and $s_j = \frac{n_j}{\sum_k n_k}$ is the a priori profile shape.

For the glyoxal AMF computation, we use a precomputed five dimensional lookup table of box air mass factors $m_j(\theta_0, \theta, \phi, \mathrm{A}, p_s)$, depending on the solar zenith angle θ_0, the line-of-sight zenith angle θ, relative azimuth angle ϕ, surface albedo A and surface pressure p_s , computed at a wavelength of 448nm using the VLIDORT 2.7 radiative transfer code (Lerot et al., 2021). For the retrieval, this lookup table is interpolated using the observation geometry values provided in the L1B input data, surface albedo from the OMI min LER albedo product (Kleipool et al. 2008), and scene surface pressure (Table 3-17). Profile shapes s are obtained by interpolating a database of monthly a priori profiles for morning and noon overpass times generated by the chemical transport model MAGRITTE on a 1° x 1° longitude/latitude grid. For observations over oceans, we use a fixed glyoxal concentration profile measured with an airborne MAX-DOAS instrument over the Pacific Ocean during the TORERO campaign (Volkamer et al., 2015), as current models cannot reproduce the enhanced glyoxal concentrations which have been detected over oceans in several studies. Table 3-17 provides an overview of the exact input data sets used for each sensor.

The effects of clouds and aerosol are not modeled. Instead, we apply a strict filter where all observations with an effective cloud fraction above 20% are discarded. This is motivated by the fact that glyoxal slant columns over bright scenes tend to be biased high, due to poorly understood residual spectral intereferences. For the same reason, observations over scenes with snow and ice are excluded from the retrieval. Observations with solar zenith angle above 70° are also excluded from the retrieval, motivated by the fact that, especially at low sun elevation, Rayleigh scattering strongly reduces the sensitivity of nadir-viewing UV-visible instruments to the lower atmosphere.

Table 3-17: Radiative transfer input data per sensor.

	GOME-2	OMI	TROPOMI
Snow/ice flag, land/ocean flag	NO_2 OFL	$O_2 – O_2$ cloud	NO_2 OFL
Cloud fraction, Cloud pressure	NO_2 OFL	$O_2 – O_2$ cloud	NO_2 OFL
Surface pressure / surface altitude	NO_2 OFL	$O_2 – O_2$ cloud	NO_2 OFL
A priori profile shapes	MAGRITTE simulations at 9h30 local time	MAGRITTE simulations at 13h30 local time	
Surface albedo	Kleipool et al. 2008		

Empirical correction for strong NO_2 absorption

The fitting approach used in Eq. 3-16, which fits a single slant column value for all wavelengths, relies on the assumption that the effective light path through the atmosphere is independent of the wavelength. In the case of strong absorption by one or more species, this assumption may no longer hold, and the quality of the fit is degraded. For glyoxal retrievals in the 435-460 nm fitting window, extreme NO_2 concentrations can have this effect. Pukite et al. (2010) have shown that fitting additional cross sections which represent the Taylor expansion of a wavelength-dependent slant column, can compensate the error, but this comes at the cost of increased scatter in the retrieved SCD's, especially in regimes with low NO_2 SCD's. Therefore, we opt for an empirical correction of the glyoxal SCD, using a linear function of the fitted NO_2 SCD:

$$\Delta\mathrm{SCD}_{\mathrm{CHOCHO}} = -8.75 \cdot 10^{12}\ molec.\,\mathrm{cm}^{-2} - 7.01 \cdot 10^{-3}\ \mathrm{SCD}_{\mathrm{NO_2}} \qquad \textbf{Eq. 3-18}$$

where the correction coefficients in Eq. 3-18 have been determined from a sensitivity test comparing fitted glyoxal SCD's with and without the additional Pukite terms in regimes with high NO_2 SCD's (Lerot et al., 2021).

Background correction

Systematic biases in the retrieved SCD's remain, due to interferences with spectral signatures from other absorbers, or due to instrumental effects. In order to reduce these biases, we apply a background correction using observations in a reference sector in the equatorial Pacific, where we assume a homogeneous background glyoxal vertical column density

$$\mathrm{VCD}^{\mathrm{ref}} = 1 \cdot 10^{14}\ \mathrm{molec.\,cm}^{-2} \qquad \textbf{Eq. 3-19}$$

For any satellite observation, this reference VCD can be translated into a corresponding $\mathrm{SCD}^{\mathrm{ref}}$ using the observation's air mass factor:

$$\mathrm{SCD}^{\mathrm{ref}}(\mathrm{obs}) = \mathrm{VCD}^{\mathrm{ref}} \cdot \mathrm{AMF}(\mathrm{obs}) \qquad \textbf{Eq. 3-20}$$

The background correction consists of correcting for the mean difference between the retrieved slant column $\mathrm{SCD}(\mathrm{obs})$ and the corresponding $\mathrm{SCD}^{\mathrm{ref}}(\mathrm{obs})$ for observations int the reference sector. The following sections describe the exact correction procedure as well as selection criteria for reference spectra for each of the three the instrument types.

GOME-2

Latitude bins	8 bins of width 10°, between 40°S and 40°N
Viewing zenith angle bins	11 bins of width 10°, between -55° and 55°
Longitude limit	180°E – 250°E
Filter criteria	• "effective cloud fraction" < 0.2 • No snow/ice scenes • SZA < 70° • RMS residual < 2e-3 • RMS residual < mean(RMS) + 2*std_dev(RMS) • VCD within 3 standard deviations of the mean VCD

	• SCD_liquid_water) < median(SCD_liquid_water) + std_dev(SCD_liquid_water) • No backscan pixels

For the GOME-2 instruments, we split the observations in the refence sector into latitude and viewing zenith angle (VZA) bins $(i,j), i = 1 \dots N_{\text{lat}}, j = 1 \dots N_{\text{VZA}}$. In a first step, we compute a VZA-dependent offset: for each VZA bin j, we compute the mean difference of the observed SCD and the reference SCD, for the observations from all latitude bins inside the equatorial range 20°S-20°N:

$$\Delta_{\text{VZA}}(j) = \frac{1}{\text{N}_{\text{obs}}} \sum_{obs\ in\ bins\ with\ |\text{lat}|<15,\ \ VZA\ bin\ j} \left(\text{SCD}(\text{obs}) - \text{SCD}^{\text{ref}}(obs)\right) \qquad \textbf{Eq. 3-21}$$

Next, we compute the remaining latitude-dependent offset after subtracting the VZA-dependent offset for the corresponding VZA bin from each SCD. For each latitude bin i, we compute the mean offset over all VZA bins:

$$\Delta_{\text{lat}}(i) = \frac{1}{N_{\text{obs}}} \sum_{obs\ in\ lat\ bin\ i,\ \text{all VZA bins}} \left(\text{SCD}(\text{obs}) - \Delta_{\text{VZA}}(j_{\text{obs}}) - \text{SCD}^{\text{ref}}(obs)\right) \qquad \textbf{Eq. 3-22}$$

Where j_{obs} is shorthand for "the VZA bin of the current observation".

We then compute correction factors for every latitude and viewing zenith angle by fitting a continuous function through these discrete offsets. We use a cubic spline interpolation $\Delta_{\text{VZA}}(\theta)$ for the VZA-dependent correction, and a linear fit $\Delta_{\text{lat}}(l)$ for the latitude-dependent correction, extrapolating for latitudes outside of the reference sector, and correct every SCD as follows:

$$\text{SCD}^{\text{BC}} = \text{SCD} - \Delta_{\text{VZA}}(\theta) - \Delta_{\text{lat}}(l) \qquad \textbf{Eq. 3-23}$$

where θ and l are the corresponding viewing zenith angle and latitude, respectively.

OMI

Latitude bins	4 bins of width 20°, between 40°S and 40°N
Longitude limit	180°E – 250°E
Filter criteria	• Cloud fraction < 0.2 • No snow/ice scenes • SZA < 70° • RMS residual < 1.5e-3 • RMS residual < mean(RMS) + 2*std_dev(RMS) • VCD within 3 standard deviations of the mean VCD • SCD_liquid_water) < median(SCD_liquid_water) + std_dev(SCD_liquid_water)

	• Abs(Radiance_shift) < 0.005nm (to filter pixels affected by the OMI row anomaly)

For OMI, we split the observations in the reference sector into to latitude and detector row bins $(i,r), i = 1 \dots N_{\text{lat}}, r = 1 \dots 60$. The first step consists of computing a row-dependent offset, or destriping correction: for each detector row r, we compute the mean difference of the observed SCD and the reference SCD, for all observations in the latitude bins inside the equatorial range 20°S-20°N:

$$\Delta_{\text{stripe}}(r) = \frac{1}{N_{\text{obs}}} \sum_{\text{obs in bins with } |lat|<15,\ \text{row } r} \left(\text{SCD}(\text{obs}) - \text{SCD}^{\text{ref}}(\text{obs})\right) \quad \textbf{Eq. 3-24}$$

Next, we compute the remaining latitude-dependent offset after subtracting the stripe correction for the corresponding row from each SCD. For each latitude bin i, we compute the mean offset over all rows:

$$\Delta_{\text{lat}}(i) = \frac{1}{N_{\text{obs}}} \sum_{\text{obs } in\ lat\ bin\ i,\ \ all\ rows} \left(\text{SCD}(\text{obs}) - \Delta_{\text{stripe}}(r_{\text{obs}}) - \text{SCD}^{\text{ref}}(\text{obs})\right) \quad \textbf{Eq. 3-25}$$

where r_{obs} is shorthand for the detector row of the current observation. Using these offsets per row and latitude bin, we correct each slant column as follows:

$$\text{SCD}^{\text{BC}} = \text{SCD} - \Delta_{\text{stripe}}(r) - \overline{\Delta_{\text{lat}}} \quad \textbf{Eq. 3-26}$$

where $\overline{\Delta_{\text{lat}}}$ is the average correction over all latitude bands.

TROPOMI

Latitude limit	20°S – 20°N
Longitude limit	165°E – 220°E
Fiter criteria	• Cloud fraction < 0.2 • No snow/ice scenes • SZA < 70° • RMS residual < 1.5e-3 • RMS residual < mean(RMS) + 2*std_dev(RMS) • VCD within 3 standard deviations of the mean VCD

For TROPOMI, we find that the retrieved SCD's contain artifacts which we cannot correct using only information from the equatorial reference sector. When averaging the retrieved SCD's per detector row and per scanline for a complete 16-day orbit repeat cycle, a persistent pattern emerges, showing SCD offsets depending on the detector row ("cross-track") and scanline ("along-track"), as shown in Figure 3-7). Along the cross-track dimension, the pattern exhibits short-scale variations ("stripes") as well as broader features. Along the orbit scanline dimension, the pattern varies mostly over large length scales. The strong row-dependence of

the pattern points to an instrumental issue which affects the retrieved SCD's, as the only physical pattern we would expect is a large-scale variation along the scanline dimension, representing the variation of the mean global glyoxal background depending on latitude and solar zenith angle. When averaging over a complete orbit repeat cycle, we obtain the global average slant column as observed by every detector row, so variations across the detector rows should be dominated by the random noise on the averaged retrieved SCD's, and not exhibit highly structured patterns. It is not clear whether the observed pattern is caused by an issue in the L1B data, or due to a spectral calibration issue, related to the inclusion of (partially) clouded spectra in the mean radiance reference spectrum used in the fit.

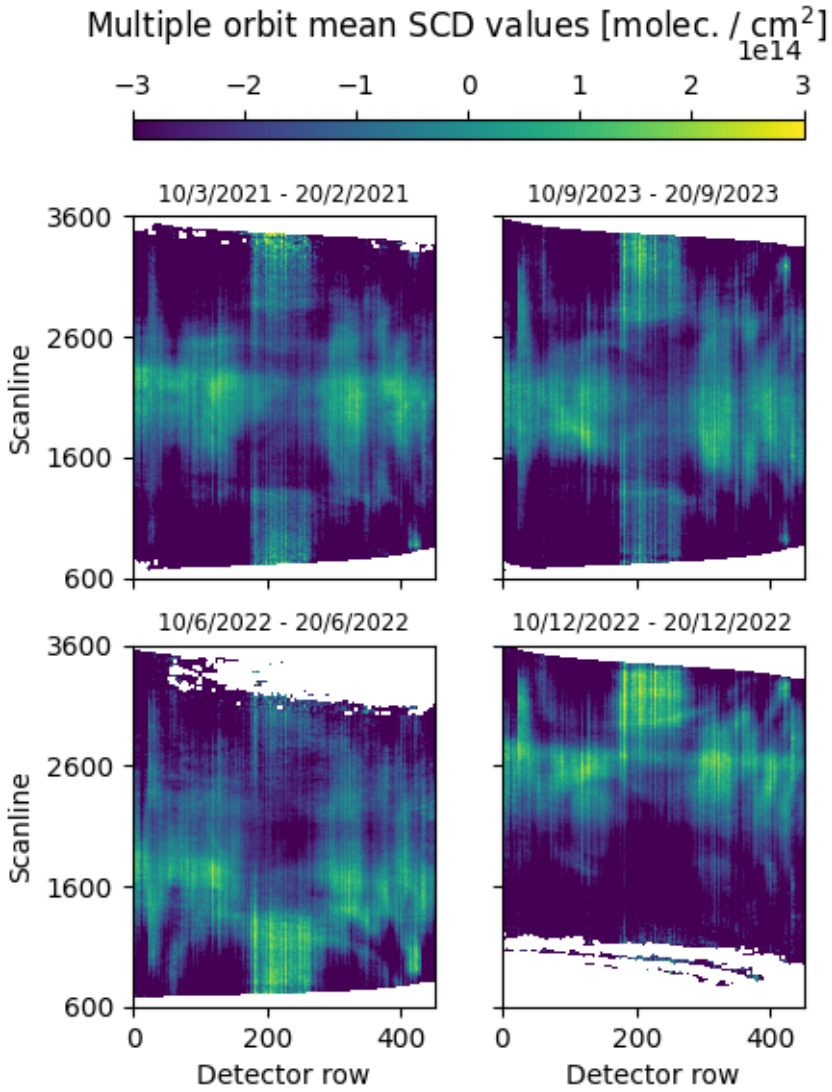

Figure 3-7: Mean Glyoxal SCD patterns recurring across different years and seasons.

The background correction for TROPOMI consists of three steps:

1. Correction for persistent artifacts using the grid of mean SCD's.
2. De-striping using a combined wavelet-Fourier filtering method.
3. Adjustment with respect to the reference sector VCD.

To remove the artifacts illustrated in Figure 3-7, we calculate $\mathrm{SCD}_{\mathrm{i,j}}^{\mathrm{mean}}$, the mean SCD per scanline i and detector row j for a rolling 16-day window centered on the current day of observations, for every day of the dataset. Only retrievals with a good QA value (>0.5) are included in the average. To separate the row-dependent artifacts from the smooth overall dependence on latitude and solar zenith angle, we also take the average of the 16-day mean SCD per scanline for all rows. The row-dependent artifacts at scanline i and row j are then given by the difference:

$$\boldsymbol{\Delta_{i,j}^{\mathrm{mean}}} = \mathrm{SCD}_{\mathrm{i,j}}^{\mathrm{mean}} - \sum_{\boldsymbol{k=1..450}} \mathrm{SCD}_{\mathrm{i,k}}^{\mathrm{mean}} \qquad \textbf{Eq. 3-27}$$

For those pixels (i,j) where no retrievals with a good QA value are found and therefore no mean SCD can be calculated, we set $\Delta_{i,j}^{\mathrm{mean}}$ to the mean value for all valid pixels of the detector row j. The first step of the background correction procedure is to subtract the correction $\Delta_{i,j}^{\mathrm{mean}}$ from the retrieved SCD for every pixel:

$$\mathrm{SCD}_{\mathrm{i,j}}^{(1)} = \mathrm{SCD}_{\mathrm{i,j}} - \Delta_{i,j}^{\mathrm{mean}} \qquad \textbf{Eq. 3-28}$$

In addition to the persistent artifacts present in the mean slant column density, we also observe stripe patterns which vary per orbit. To reduce these striping artifacts as well, we further correct $\mathrm{SCD}^{(1)}$ using a combined wavelet and Fourier filtering technique (Münch et al., 2009, Schneising et al, 2023).

The two-dimensional discrete wavelet transform applies a pair of matching low- and high-pass filters to the along-track and cross-track dimensions to decompose the grid of SCD's into a low-frequency approximation (low-pass filtering along both dimensions), and vertical (low-pass along-track, high-pass across-track), horizontal (high-pass along-track, low-pass across-track) and diagonal (high-pass along both dimensions) detail components. By iteratively applying this decomposition to the low-frequency component obtained in the previous step, we obtain a multi-level wavelet decomposition with approximation, horizontal, vertical and diagonal coefficients $c_{l,m,n}^{A}, c_{l,m,n}^{H}, c_{l,m,n}^{V}, c_{l,m,n}^{D}, l = 1 \dots L$, where coefficients at higher levels represent image features at increasingly larger scales.

The striping artifacts we want to correct for, are contained in the vertical detail coefficients $c_{l,m,n}^{V}$. Too reduce the stripes, we can apply a suitable transformation to these vertical detail coefficients, and use the inverse wavelet transform to obtain a corrected SCD grid. A "perfect" stripe, in the sense of a constant offset of the SCD's at a given row j, would lead to a constant contribution to the corresponding vertical detail coefficients at a given cross-track position n, for all along-track indices m. We can remove such stripes by subtracting the "along-track" mean of the vertical coefficients at every cross-track position:

$$c_{l,m,n}^{\prime V} = c_{l,m,n}^{V} - \frac{1}{M}\sum_{i} c_{l,i,n}^{V} \qquad \textbf{Eq. 3-29}$$

However, we find that the stripe artifacts do not always correspond to a constant offset: we observe stripes where the magnitude, or even the sign of the offset with respect to adjacent

rows changes along the orbit. We regard any vertical detail features which are constant or vary over very long scales in the along-track dimensions as artifacts and use the combined wavelet-Fourier filtering approach from Münch et al. to filter such features. Using the fast Fourier transform, we obtain coefficients $\hat{c}^{V}_{l,m,n}$, the frequency domain representation of the vertical detail coefficients, and then attenuate the components with a frequency around 0 in the along-track dimension with a gaussian kernel:

$$\hat{c}'^{V}_{l,m,n} = \hat{c}^{V}_{l,m,n} \cdot (1 - e^{-\frac{m^2}{2\sigma^2}}) \qquad \textbf{Eq. 3-30}$$

where the parameter σ controls the width of the impacted frequency band. This is a more general form of equation Eq. 3-30, where a range of low frequencies is suppressed, instead of just the constant component. More stripes are removed when we use a larger value of σ, at the risk of losing more physical information as well. We choose maximum decomposition level $L = 6$ and frequency filter width $\sigma = 25$. After correcting the vertical detail coefficients in this way, we apply the inverse Fourier and wavelet transforms to obtain the de-striped slant columns $\mathrm{SCD}^{(2)}_{i,j}$. An important detail is that we only use SCD's with a QA-value > 0.5 to determine this correction. For all other pixels, we add the mean of the correction $\mathrm{SCD}^{(2)}_{\mathrm{i,j}} - \mathrm{SCD}^{(1)}_{\mathrm{i,j}}$ obtained for the valid pixels of the same detector row j.

In the final step of the background correction, we account for the background concentration in the equatorial reference sector. We calculate a correction $\Delta\mathrm{SCD}^{\mathrm{ref}}$ based on the mean difference between the de-striped slant column $\mathrm{SCD}^{(2)}$ and the "reference SCD" for all observations matching our reference selection criteria for the same day:

$$\Delta\mathrm{SCD}^{\mathrm{ref}} = \frac{1}{N_{\mathrm{obs}}} \sum_{\mathrm{obs\ in\ ref\ sector}} \mathrm{SCD}^{(2)}_{\mathrm{obs}} - \mathrm{VCD}^{\mathrm{ref}} \cdot \mathrm{AMF}_{\mathrm{obs}} \qquad \textbf{Eq. 3-31}$$

We obtain the background-corrected SCD for all observations by subtracting $\Delta\mathrm{SCD}^{\mathrm{ref}}$ from the de-striped slant columns:

$$\mathrm{SCD}^{\mathrm{BC}} = \mathrm{SCD}^{(2)} - \Delta\mathrm{SCD}^{\mathrm{ref}}$$

3.4.3. Information content and uncertainty estimate

Many factors contribute to the retrieved glyoxal tropospheric column uncertainty: detector noise as well as systematic errors affecting fitted the slant columns, uncertainties on a priori information such as profile shapes and the reference sector background concentration, errors in auxiliary data such as surface albedo, or radiative transfer modelling errors. Table 3-18 provides an overview of the different contributions and their typical order of magnitude. We refer to the End-to-End ECV Uncertainty Budget document for a detailed analysis of the uncertainties affecting glyoxal retrievals.

Table 3-18: Glyoxal tropospheric vertical column density retrieval uncertainty components

Error source	Order of magnitude [molec. cm^{-2}]
Slant column retrieval random error	6 x 10^{14} – 1 x 10^{15} (TROPOMI)

Slant column retrieval systematic uncertainty	$5 \times 10^{13} – 1 \times 10^{14}$
Air mass factor uncertainty	$1 \times 10^{13} – 1 \times 10^{14}$
Background correction uncertainty	$5 \times 10^{13} – 1 \times 10^{14}$
Total systematic uncertainty	$1 \times 10^{14} – 3 \times 10^{14}$

3.5. Carbon monoxide (L2-CO)

3.5.1. Overview

Our objective is to generate a homogenized and merged CO L3 CDR dataset.

For that, we will use satellite data from two instruments as input: IASI and MOPITT. The IASI CO L2 data consist in a reprocessed dataset, performed by EUMETSAT in 2021.

In cycle one of WP 304, we produced an intermediate product: we post-processed IASI CO L2 data (in two steps: outliers filtering + reformating and then cloud filtering) and averaged Metop-A, B and C data in order to get a new IASI CO L3 product: multi-platform monthly grids (L3). At the time of writing this document, this new intermediate dataset has been sent to BIRA for validation.

In cycle two of WP 304, we will work on merging this new IASI dataset and MOPITT V9T data (using corrective factors) in order to build a homogenized and merged CO L3 CDR dataset.

We summarized the different steps in Figure 3-8.

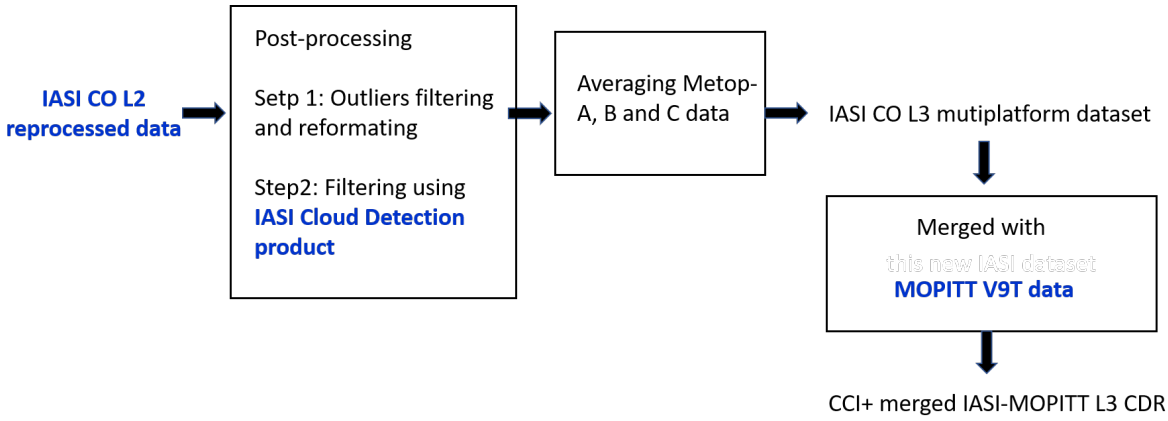

Figure 3-8: Graphic representation of the processing steps. Satellite input data are in blue.

In this section we will describe the different input satellite data and their corresponding algorithms. The description of L3 production will be given in section 3.5.

3.5.2. Algorithm description

IASI and MOPITT CO L2 products

In this work, we use the IASI L2 CO reprocessed data from EUMETSAT, called Climate Data Record (CDR) for Metop A and Metop B. In fact, EUMETSAT reprocessed the whole IASI CO data record between 2020 and 2021 and the CO CDR are available until December 2021. This was done to process the L1C IASI data with the most recent version of the auxillary IASI data used as input (temperature, humidity and cloud information; all EUMETSAT products) with

the latest FORLI version. The whole time series of IASI-CO, for the first time, has been made homogeneous. Metop C data (2019 onwards) is running with the latest algorithm.

Note that the EUMETSAT IASI L2 CO reprocessed are called IASI CO Climate Data Record (CDR). It should not get mixed up with CCI CO CDR which is the final product that will be produced within the project, that is a homogeneous and merged IASI-MOPITT L3 product.

IASI CO L2 data have been retrieved using the Fast Optimal/Operational Retrieval on Layers for IASI (FORLI), a dedicated radiative transfer and retrieval software for IASI. It was developed at the Université Libre de Bruxelles (ULB; Hurtmans et al., 2012) in collaboration with LATMOS/IPSL, with the objective to provide global concentration distributions of atmospheric trace gases. For the inversion step, it relies on a scheme based on the widely used Optimal Estimation theory (Rodgers, 2000). The software has been set-up to process IASI level 1C radiances for vertical profile retrievals of CO and has been implemented at EUMETSAT. The FORLI CO Algorithm Theorical Basis Document is available online (Astoreca et al., 2014).

IASI L2 CO product has been extensively validated. Validation Report of the reprocessed IASI L2 CO CDR can be found on the AC SAF website (Langerock 2023).

MOPITT v9T data

MOPITT (Measurements of Pollution in the Troposphere) is a gas correlation radiometer instrument on the NASA Terra satellite which permits retrievals of CO vertical profiles using both thermal-infrared (TIR) and near-infrared (NIR) measurements. MOPITT instrument has been in operation since 2000 (Drummond et al., 2016), resulting in a long-term data record. CO retrievals are obtained by using a maximum a posteriori method that incorporates a priori information of the physical and statistical variability of the trace gas distribution in the atmosphere. For this study we use MOPITT V9T data. The MOPITT CO Algorithm Theorical Basis Document is available on line (Francis et al., 2017). MOPITT L2 CO data have been extensively validated (Deeter et al., 2022).

IASI Cloud Detection Product

The “IASI Cloud Detection” product is a new cloud mask available at the IASI pixel level (L2) that was developed by Simon Whitburn at ULB, for climate applications purposes. It is a different product from the EUMETSAT Cloud product used when retrieving IASI CO L2 with FORLI. It combines a high sensitivity to cloud detection, a very good consistency over time and between the three IASI instruments and simplicity in its parametrization. The method is based on the use of a supervised neural network using the version 6.5 of the operational IASI L2 cloud product as a reference dataset. As input parameters, it relies on IASI radiance information only. The consistency over time is ensured by careful selection of the IASI input channels, avoiding especially the spectral regions affected by long-lived absorbers and water vapor. The IASI Cloud Detection algorithm’s description and validation are presented in Whitburn et al. (2022). In the project, this independent improved cloud product will be used a posteriori on the IASI CO data (already filtered with a EUMETSAT cloud product), in order to get a “cleaner” product if possible.

3.5.3. Uncertainty estimate

For this section, we refer to the E3UB document where an analyse of the CO uncertainty on global and local scale is presented. On global scale, mean uncertainty for daytime measurements is 1.4 10^{17} molecules/cm^2 with a standard deviation of 0.1 10^{17} molecules/cm^2 for both Metop-A and Metop-B. For nighttime, the mean uncertainty is larger: 1.7 10^{17} molecules/cm^2 [std: 0.1 10^{17} molecules/cm^2]. Uncertainty time series for the whole globe is shown in Figure 3-9.

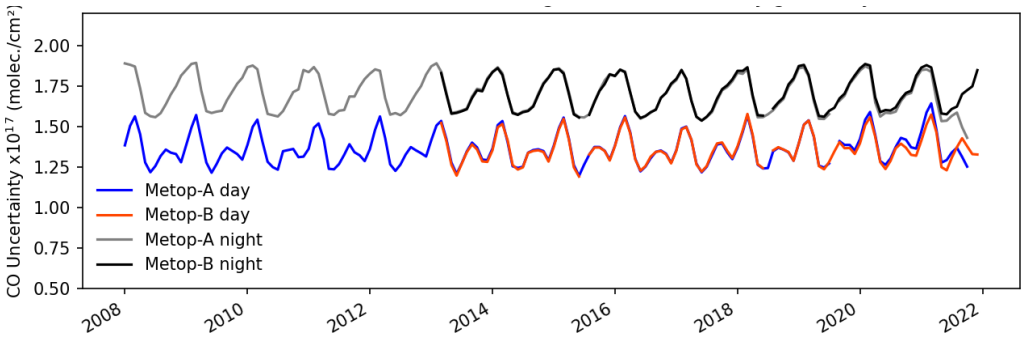

Figure 3-9: CO uncertainty time series for the globe, for day time and night time measurements, for both Metop-A and Metop-B.

3.6. Ammonia (L2-NH_3)

This section describes the ANNI v4 NH_3 retrieval algorithm (level 2) for IASI onboard Metop-A, B, and C, developed at the ULB. The retrieval algorithm is part of a chain of retrieval algorithms called the ANNI (Artificial Neural Network for Infrared Atmospheric Sounding Interferometer, IASI) retrieval framework, for the retrieval of short and medium long-lived trace gases, see Franco et al. (2018). The historical development, theoretical basis and background has been documented in a series of papers: Whitburn et al. (2016), Van Damme et al. (2017), Franco et al. (2018), Van Damme et al. (2021) and Clarisse et al. (2023). Most of the text and some figures below are taken from these publications. Some material is also taken from Clarisse et al. (2019), and some is original.

3.6.1. Retrieval overview

A schematic overview of the ANNI retrieval is presented in Figure 3-10. The actual calculation of the columns (red boxes in Figure 3-10) relies on two computational steps:

1. The calculation for each IASI observation of a hyperspectral range index (HRI). This quantity is a very sensitive, broadband spectral index that quantifies the signal strength of a target absorber in a radiance spectrum.
2. The conversion of the HRI into a total column abundance via an artificial feedforward neural network (NN).

In addition to the HRI, the NN relies on a series of auxiliary parameters related to the state of the atmosphere and of the surface. Perturbations to the input data of the NN allows quantification of the uncertainties associated with single pixel retrieved columns. The neural network is also employed for the calculation of total column averaging kernels. Appropriate filtering of the data (before and after the retrieval) removes cloudy scenes and observations with limited or no sensitivity to the target trace gas. Finally, in general (for most species in the ANNI retrieval framework), a calibration offset is added to the retrieved columns to account for the constant, climatological background column of the target gas in the atmosphere (green box in Figure 1). However, this last step is not done for NH_3, as background concentrations are extremely low and below the detection limit of IASI.

While the retrieval itself is simple and fast, the initial setup (blue and red boxes in Figure 3-10) of the HRI and NN is nontrivial. In particular, both rely on weight constants that must be determined with care beforehand from a data set of real (for the HRI) and synthetic (for the NN) IASI spectra. The setup of the HRI and NN and the training of these weight constants are detailed in sections 3.6.2 and 3.6.3. The calculation of the AVKs is detailed in section 3.6.4.

Running the NN relies on a series of (meteorological) input data that is different for each observation. The ANNI v4 NH_3 product exists in two flavours, depending on the origin of this input data. Whereas the baseline product (also called near-real time (NRT) product) uses operational IASI Level 2 (L2) information on the pressure, humidity and temperature profiles and a climatology characterizing the boundary layer height, the reanalysed product uses ERA5 model output for these parameters (Hersbach et al., 2020), interpolated in time and space to match the observations. The resulting product is temporally more consistent as it removes the effect of the several changes that occurred in the L2 products throughout the years. Both NH_3

products include several empirical corrections to counter small differences observed between the three IASI instruments and small biases that occurred because of sporadic changes to the IASI instrument or in the L0 to L1c processing of the spectra. The actual retrieval is presented in section 3.6.5., which also includes information on pre and post filtering flags, and uncertainty calculation. Examples are presented in 3.6.6. Section 3.6.7 summarizes the main advantages of the retrieval algorithm. Finally, we present a comparison of the ANNI retrieval with an OEM retrieval.

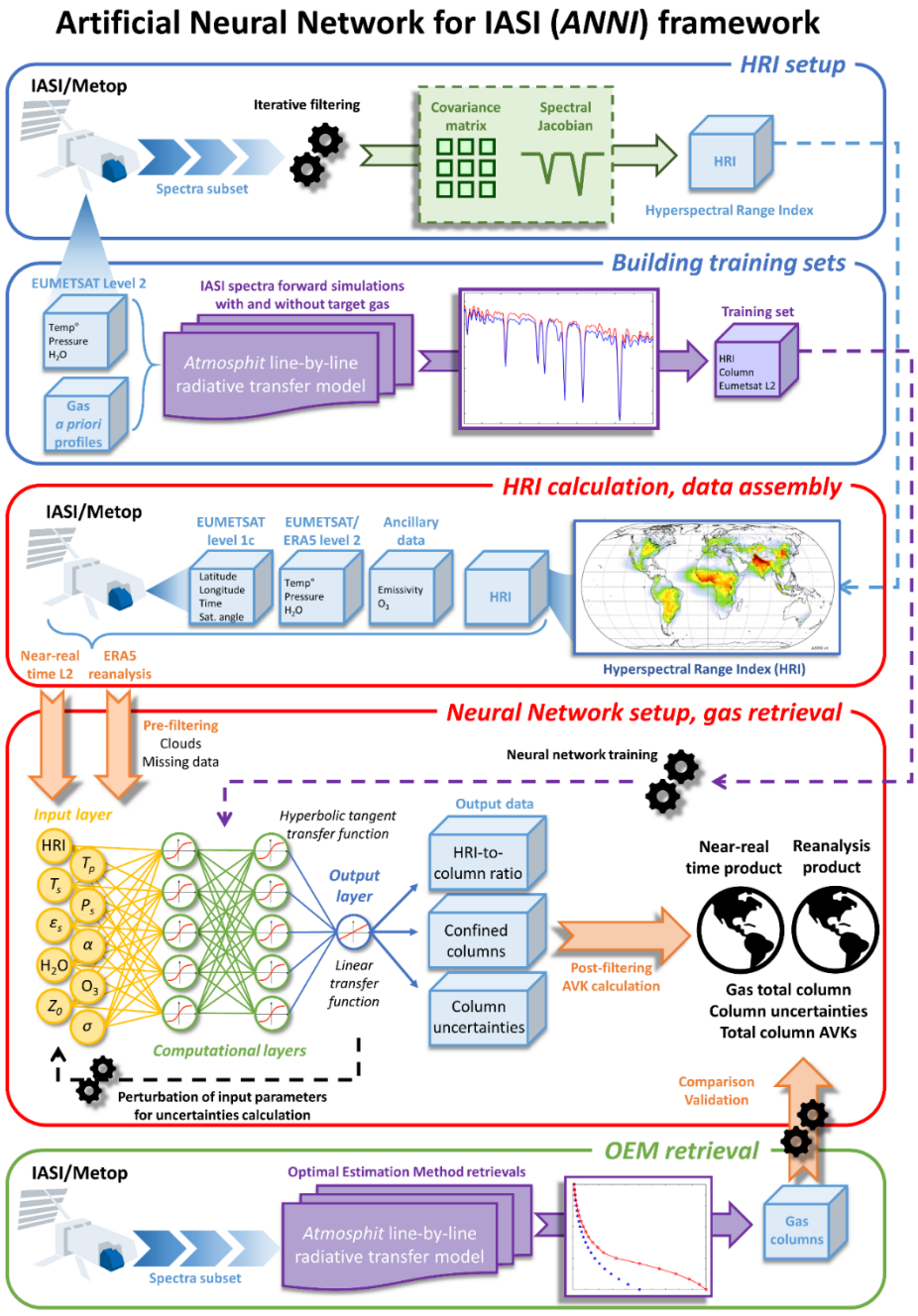

Figure 3-10: Conceptual flowchart of the ANNI retrieval method for NH_3.

3.6.2. HRI

Definition

Proposed by Walker et al. (2011), the HRI is a dimensionless index that quantifies the strength of the spectral signature of a target gas in an observed spectrum y:

$$\mathrm{HRI} = \frac{K^T S_y^{-1}(y-\bar{y})}{\sqrt{K^T S_y^{-1} K}} \frac{1}{N} \qquad \textbf{Eq. 3-32}$$

where K is a spectral Jacobian, S_y a covariance matrix, and $\bar{y}$ the mean spectrum generated from a representative data set of background spectra associated with a climatological column of the target gas, and N an extra normalization factor (see further). The HRI is conveniently normalized to have a mean of zero and a standard deviation of one when calculated on the data set of background spectra. The HRI is particularly suitable for the detection of highly variable infrared absorbers, like NH_3, which are not observed in every spectrum. In this case, the climatological column amount is close to zero and the background spectra are those without observable signature of NH_3. The HRI can encompass spectral ranges of up to several hundred cm^{-1} to exploit all the channels in which the target species is absorbing. This results in a substantial gain of sensitivity over other detection methods and makes it highly suitable for the detection of broadband absorption features, as demonstrated with the detection of a series of aerosol types in Clarisse et al. (2013).

Spectral range and Jacobian

Larger spectral ranges lead in principle to a more sensitive HRI. However, this is true only in the linear regime in which the covariance matrix describes a normal distribution. In practice, it can be advantageous to exclude spectral ranges where nonlinearity prevails. For instance, the spectral range 1,100–1,200 cm^{-1} can exhibit pronounced spectral surface emissivity features over deserts. In addition, it might be useful to avoid a spectral interval in which another species with a similar spectral signature is absorbing. For NH_3 the range was set to 812–1,126 cm^{-1} that exploits the strongest lines from its ν_2 vibrational band. A wider spectral range was chosen to minimize interferences with surface emissivity features. The Jacobian K is the derivative of the radiance spectrum with respect to the column abundance of the target species, and this was generated by the line-by-line radiative transfer model Atmosphit (Coheur et al., 2005) for a standard atmosphere.

Characterization of mean and covariance

For each target species, the HRI calculation also depends on a generalized covariance matrix S_y and an associated background spectrum $\bar{y}$. The covariance matrix determines the weight of each spectral channel, and ideally expresses the variability and covariance of all interfering species, but explicitly not that of the target species (Walker et al., 2011). Such a matrix can be obtained from a representative set of IASI spectra with a constant, climatological column amount of the target species. For short-lived trace gas absorbers like NH_3, the pair (S_y, $\bar{y}$) can straightforwardly be constructed from spectra with no observable signature of the gas (the associated climatological column is then close to zero). To select such spectra, an iterative

approach can be followed (Clarisse et al., 2013). The approach goes like this. First, a representative set of IASI spectra is built, consisting of all the spectra from the fifteenth of each month of 2013 but sampled to yield a spatially uniform distribution (to avoid over-representing polar regions). This entire set is then used for the generation of a first (S_y, $\bar{y}$) pair. This allowed the production of a first set of HRI, which in turn was used to remove the spectra with detectable signatures of the trace gas (typically with an HRI above 3 or 4; see below). The reduced set of spectra allows the calculation of a better (S_y, $\bar{y}$) pair. Repeating this process several times (typically at least 10 times) leads to convergence of the set of spectra, of the corresponding (S_y, $\bar{y}$), and of the HRI.

An even more sensitive HRI could be constructed by considering only the spectra with an HRI below one. Using such a low threshold removes much more spectra, including those with spectral signatures barely above the instrumental noise and even spectra without detectable gas quantities. This is obvious for NH_3, where spectra above remote oceans frequently exhibit HRIs below one. Nevertheless, removing such spectra leads to a more sensitive HRI and does not generate anomalies (e.g., false detections). There is, however, a side effect, in that the initial normalization of the HRI is not preserved in the iterative process. This is the reason why an additional normalization factor (N) is needed in the calculation of the HRI. Note that this factor N needs to be recalculated at each iteration. The normalization factor N was calculated as the standard deviation of the HRI over a remote ocean area, where no NH_3 is expected.

In total 24 iterations were carried out for the construction of the covariance matrix. In addition to all observations with an HRI below one, also observations over selected desert regions were included at each iteration, these include most notably, the Saharan Desert, Arabian desert, and parts of the Great Simpson, as no NH_3 is expected for those, and to make the HRI more robust for the emissivity features found over deserts.

Pseudoinverse

The generalized error covariance matrix S_y plays a key role in the calculation of the HRI. As a symmetric matrix, S_y has real eigenvalues λ_i and can be decomposed as:

$$S_y = \sum_{i=1}^{n} \lambda_i \vec{s_i} \, \vec{s_i^T} \qquad \text{Eq. 3-33}$$

with all $\vec{s_i}$ orthogonal to each other. It follows that its inverse can be written as:

$$S_y^{-1} = \sum_{i=1}^{n} \frac{1}{\lambda_i} \vec{s_i} \, \vec{s_i^T} \qquad \text{Eq. 3-34}$$

The distribution of the eigenvalues of the covariance matrix used for the NH_3 HRI (with a spectral range covering 812 to 1126 cm^{-1}) is shown in Figure 3-11. Three domains can be distinguished: (i) the 30 highest values, corresponding to the principal components, (ii) around 1200 values corresponding mainly to instrumental noise and (iii) around 20 very small eigenvalues. These smallest eigenvalues are of the order of the numerical precision at which the covariance matrix is calculated, and in essence correspond to directions not occurring in

IASI spectra. While random instrumental noise would be expected to occur in all directions, apodization and L1 post-processing remove some. Such directions carry the most weight in S_y^{-1} but as they are not found in real spectra they do not contribute much to the total HRI (as can easily be verified numerically).

However, small changes to the instrument calibration or post-processing can alter the contribution of these directions in the IASI spectra, and because they carry such a large weight in the HRI, they can affect its value considerably. This explains why the HRI in the past has been found to be very sensitive to such changes. It also explains the occurrence of (small) biases between the different instruments. The solution is fortunately simple (Rodgers et al., 2003; Eaton, 2007), and is obtained by disregarding the terms corresponding to the very small eigenvalues. As we will show in the next section, using such a pseudoinverse does not eliminate the effects of L1C changes completely, but reduces their magnitude considerably.

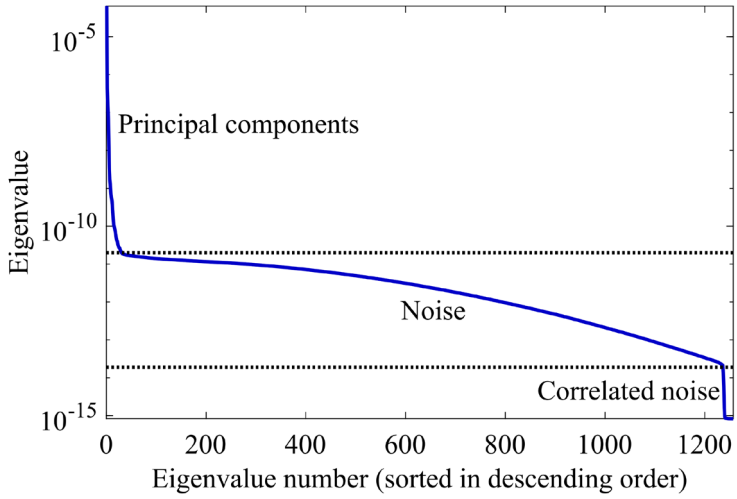

Figure 3-11: Eigenvalue spectrum of the covariance matrix S_y used for the calculation of the HRI of NH_3. The eigenvalues are ordered from largest to smallest.

Detrending and anomaly corrections

As the mean spectrum and covariance matrix that are used for the HRI are calculated from spectra measured within one reference year (2013), long-term changes in atmospheric composition that affect the spectral region of interest, can have unwanted effects on the HRI. This was first noted in Van Damme et al. (2021), where a spurious trend was seen in the HRI NH_3 data over remote regions. It was attributed to the increase in global carbon dioxide (CO_2) concentrations, because of the presence of a weak CO_2 absorption band in the 920-990 cm^{-1} spectral region (Whitburn et al., 2021) where NH_3 has its strongest absorption. A linear correction on the HRI of the order of 0.03 per year was introduced to compensate for this effect. However, because of seasonal variations, and possible temperature dependence of the interference, an HRI which is less sensitive to CO_2 changes is preferable. One option is to build the covariance matrix from spectra spanning the entire period of IASI measurements.

An alternative approach is to account directly for the effects of CO_2 in the calculation of the HRI. The HRI formula is related to generalized least squares estimation and can be expanded

to include multiple variables that are simultaneously estimated (Walker et al., 2011; Theys et al., 2022). In our case, the Jacobian vector becomes a two-column matrix, one column corresponding to NH_3 and the other to CO_2. The HRI formula remains formally identical (with only the first component of the two-element HRI vector of interest).

The stability of the HRI was evaluated over ten remote regions, where only background columns of NH_3 are expected. Their average monthly HRI is shown in Figure 3-12. for the three IASI instruments separately. The top panel shows the average as obtained with the HRI setup as described above, i.e., with pseudoinverse and with a CO_2 Jacobian. As with previous versions of the product, a spurious linear trend is observed, but thanks to the introduction of the CO_2 Jacobian, its magnitude is reduced to about 0.01 per year, compared to 0.03 per year previously. A slightly steeper decrease is observed for Metop B. We correct for these trends by adding a time-dependent offset as in Van Damme et al. (2021). The result after correction is shown in the second panel of Figure 3-12.

A detailed analysis was made of this time series to detect offsets between the different instruments and shifts that coincide with known changes in the IASI L1C data. The largest of these is the offset of 0.11 seen between IASI-C and the two other instruments. Small offsets in the HRI time series of IASI-A were found in 2010, 2015 and 2017 and in the HRI of IASI-B in 2015. For each of these, offset corrections were calculated in the range of 0.01-0.03. Thanks to the pseudoinverse, their magnitude is drastically reduced (previously, offsets as large as 0.6 were observed). The resulting corrected time series is shown in the third panel. This time series is temporally stable and shows an excellent consistency between the three instruments, but exhibits a weak seasonal cycle, likely due to the combined effect of seasonal changes in the concentrations of H_2O and volatile organic compounds that absorb in the same spectral range as NH_3. To remove this seasonality an offset depending on latitude and month of the year was calculated from 2012-2014 IASI-A data and applied on all data. The HRI after correction is shown in the bottom panel of Figure 3-12. Thanks to the improved setup of the HRI, and the new cloud product, the magnitude and therefore also uncertainty of all these corrections is lower than in the previous product, which in the end results in much improved temporal consistency.

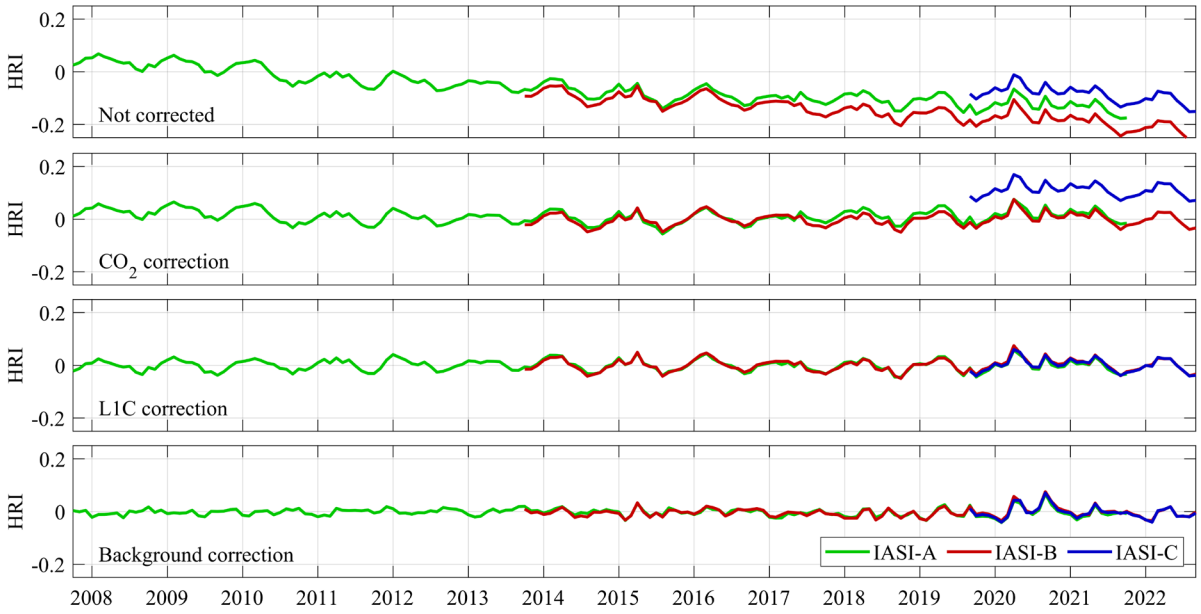

Figure 3-12: Monthly average HRI time series over 10 remote regions for the three IASI instruments separately. The top panel shows the uncorrected timeseries, and the other panels, from top to bottom, show the effects of the corrections that are applied consecutively.

3.6.3. The neural network

The spectral signature (the HRI) of a target gas is a complex function of the species abundance and of all the other parameters entering the radiative transfer, such as the state of the atmosphere (thermodynamic parameters) and surface, interfering species, and the viewing angle. The main idea of the ANNI retrieval approach is to use a neural network (NN) to approximate the complex inverse function that maps the HRI and the auxiliary parameters to a column abundance. In particular, the measured HRIs are related to estimates $\hat{X}^a$ of the true NH_3 total columns X, via a scaling factor SF^a

$$\hat{X}^a = \frac{\mathrm{HRI}}{\mathrm{SF}^a} \qquad \textbf{Eq. 3-35}$$

In the retrieval, a specific vertical profile is assumed for NH_3, but otherwise the retrieval is entirely unconstrained. The superscript "a" refers to this vertical profile assumption. In particular, we assume that the total column $\hat{X}^a$ is vertically distributed according to an a priori vertical partial column profile:

$$a_z = \frac{\hat{X}_z^a}{\hat{X}^a} \qquad \textbf{Eq. 3-36}$$

with $\sum_z a_z = 1$.

Training set assembly

The scaling factors are thus calculated in the ANNI retrieval framework with a NN. A NN consists of interconnected nodes (small mathematical functions) organized in layers, as illustrated in Figure 3-10 (lower red box). The weights of the nodes are trained to best fit the complex analytical relationships that bind any set of input variables feeding the network, to

the corresponding output variable. NNs learn from the presentation of examples, and so training sets are required consisting of matching input (auxiliary parameters, column abundance) and output data (IASI spectrum and associated HRI).

The performance of a NN depends largely on the quality of the training set, which should be as comprehensive and representative as possible. This means that in our case, the set should cover a large range not only of the column abundances of the target trace gas (and associated HRI) but also of the auxiliary parameters on the state of the atmosphere and surface. Each IASI observation (L1C radiance spectra) is distributed operationally with corresponding Level 2 data consisting of a temperature, pressure, H_2O profile, and surface temperature (August et al., 2012). These were used here as input for the auxiliary parameters of the training data set. We selected approximately 500,000 IASI L2 data over the year 2013, regularly sampled in space and time to ensure a comprehensive and representative data set.

As the surface temperature and emissivity vary more over land than over oceans, 66 % of the data were chosen to be associated with land observations. Additional data were added for the higher and lower thermal contrasts TCs (defined as the temperature difference between the surface and the air layer located just above) to ensure that extreme TCs are sufficiently represented within the training data set. Finally, a random column of the target trace gas was associated with each sample in the data set. These random columns were generated by randomly scaling a vertical profile of the gas for a wide range of total columns (Figure 3-13, left). Figure 3-14 illustrates the spatial distribution of the resulting data set as well as the sampling as a function of thermal contrast and total column. IASI spectra were simulated for each sample in this data set using Atmosphit. Due to small remaining forward model errors, it was found that HRI values produced by Atmosphit can be biased. For this reason, a spectrum was simulated for each sample with and without the target trace gas. The HRI of the simulation without the target gas was then used to offset the HRI of the other simulation, in such a way that an HRI value of zero always corresponds to the absence of the trace gas. Note that since Atmosphit does not simulate the clouds, the resulting training data set is cloud-free.

As discussed in Whitburn et al. (2016), the vertical profile of NH_3 is parameterized with a Gaussian function as:

$$\mathrm{VMR}(z) = \mathrm{VMR}(z_0)e^{-\frac{(z-z_0)^2}{2\sigma^2}} \qquad \textbf{Eq. 3-37}$$

with z the altitude about ground level, z_0 the peak altitude and σ the width of the profile. This parametrization was found to be sufficiently flexible to characterize the vast majority of GEOS-Chem simulated NH_3 profiles (see Figure 3-15). The NN was trained with peak altitudes ranging from 0 to 20 km and σ from 100 m to 3 km (Figure 3-15, right). In this way, the NN is fully flexible, and the retrieval is not limited to a specific vertical profile but can be changed according to the needs of the user. Note that a larger number of scenes were generated with a value of 100 m, as these are used for the generation of averaging kernels (see section 3.6.4).

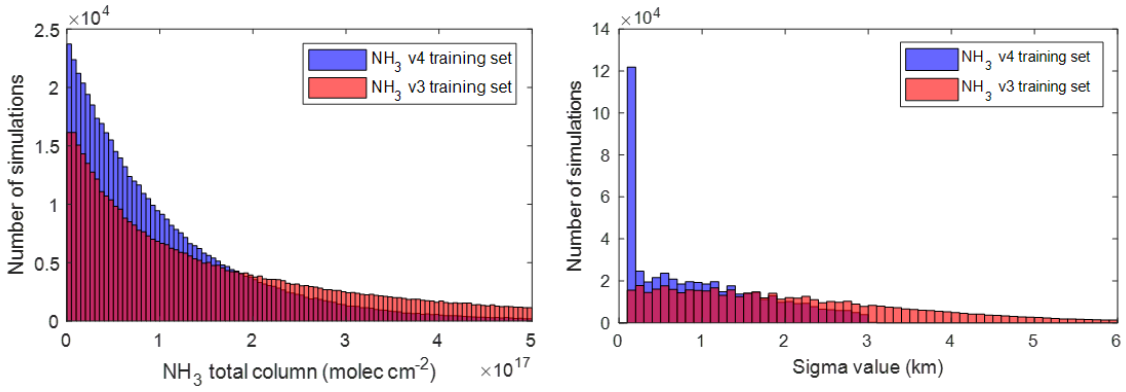

Figure 3-13: Frequency distribution of NH3 total columns (left) and σ (right) values in the v3 and v4 training set.

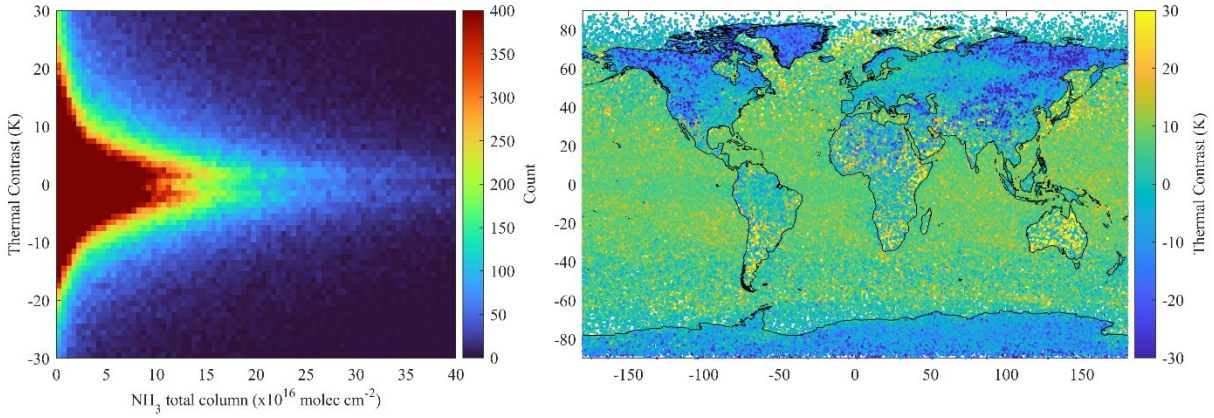

Figure 3-14: Summary statistics on the training set: distribution of thermal contrast vs NH_3 total columns (left), and spatial distribution vs thermal contrast (right).

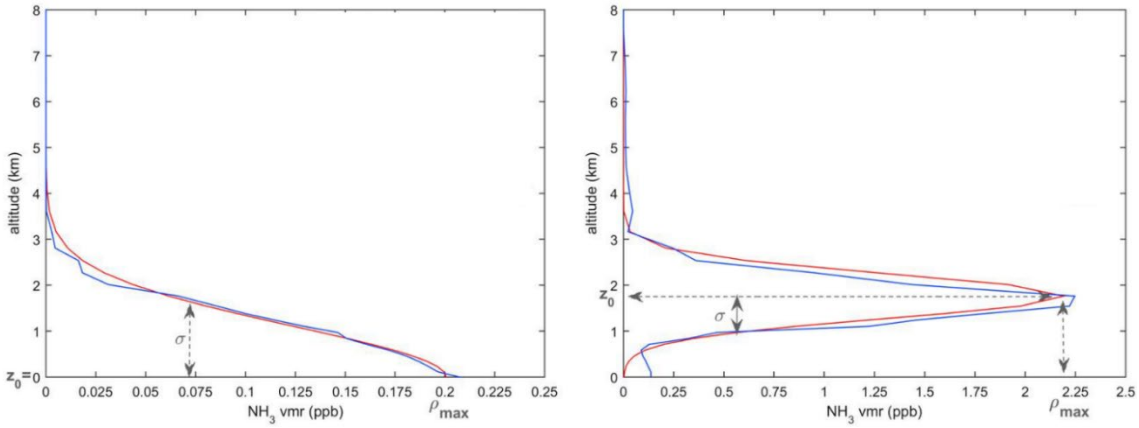

Figure 3-15: Example of GEOS-Chem model (blue) and fitted (red) profiles (left) above a source area and (right) for transported NH_3.

Network setup, training and evaluation

In theory, the input parameters could consist of all the variables used for the forward simulation of the spectra. However, this would result in a very large and difficult data set to train NNs. Instead, it is advantageous to keep the size of the NN as small as possible by only

taking into account the parameters that affect most the output variable. A satisfactory network performance was achieved by training with the following input parameters:

- HRI
- temperature profile (T_{prof}) at 0, 0.5, 1, 1.5, 2, 2.5, 3, 5, 7, 10, 13, 16, 19, 25 and 30 km
- skin temperature (T_{skin})
- surface pressure (P_{surf})
- surface emissivity (ε_{surf}): average over selected channels in the atmospheric windows
- H_2O partial column profile (H_2Oprof) between 0-1, 1-2, 2-3, 3-5, 5-7, 7-10 and 10-30 km
- satellite viewing angle (Z)
- peak NH_3 altitude (z_0)
- Spread of the NH_3 profile (σ)

The HRI-to-column ratio was adopted as output of the NN instead of the gas column itself. The rationale behind this is explained in detail in Van Damme et al. (2017) and Whitburn et al. (2016). In brief, using the ratio allows (1) for a better training of the NN owing to its smaller dynamic scale and (2) to translate the instrumental noise—which is part of the HRI—in a linear way to the retrieved column. In particular, this guarantees that the retrieval on noisy HRI does not lead to a biased product.

Based on the training performances, a NN that consists of two computational layers was setup with each 12 nodes. A multilayer NN is usually better at tackling nonlinearities than a many-node, single-layer network. We have evaluated and improved the setup of the different NNs using 2-D error plots. These summarize the performance of the NN on the training set in terms of relative error and biases as a function of gas total column and thermal contrast. The performance plots are presented in Figure 3-16. Note that normally distributed noise was added to all the input data to evaluate the performances as realistically as possible. The final NNs are seen to be practically unbiased for positive TC. For the non-background gas abundance, the relative errors range from 10% to 50%, with the highest errors found for the low gas columns. The relative errors increase for lower background columns (top panel in Figure 3-16) where the columns approach the IASI detection threshold. However, since the biases remain low (bottom panel), most of these errors can be averaged out by considering multiple observations (thus by averaging the retrieved columns in time or space). In addition, as can be expected, the NNs do not perform optimal for observational scenes with low negative TC.

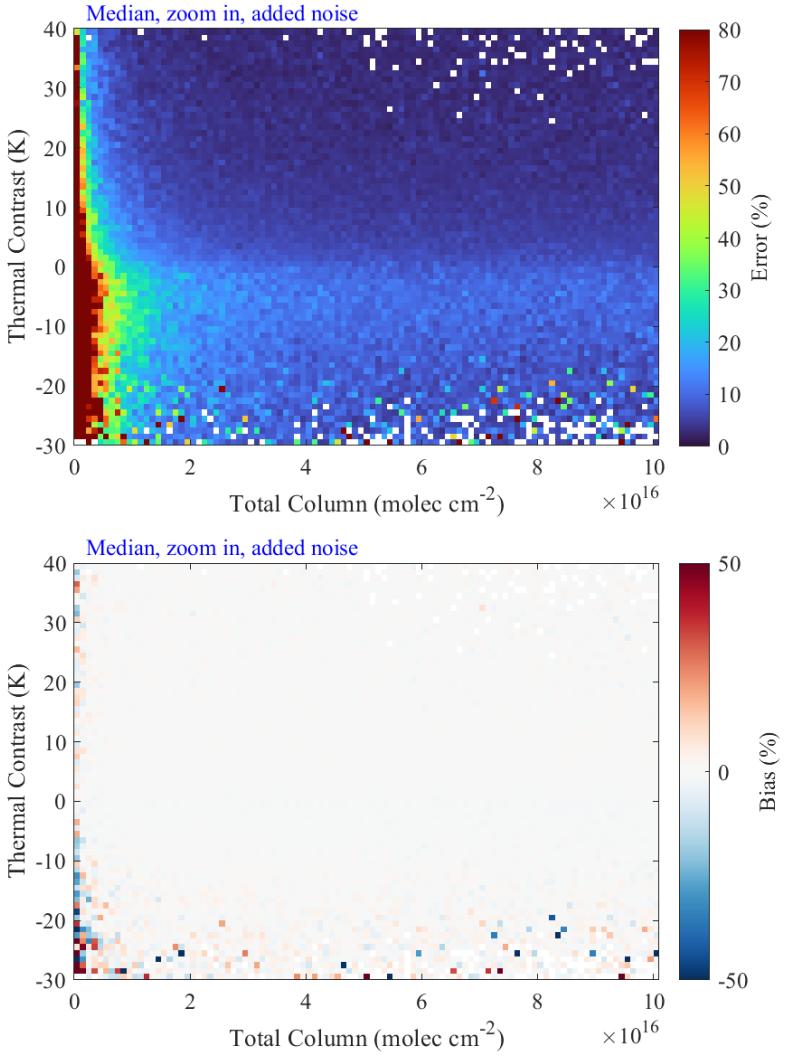

Figure 3-16: Performance evaluation of the neural network, with added noise. The median value is shown in each grid box, which removes the effect of outliers to better reflect the real performance of the network.

3.6.4. Averaging kernels

Linearity and additivity of the HRI

The main assumption on which the AVK formalism, which was introduced in ANNI v4, is based, is that the HRI is approximately linear (proportional to column) and additive, i.e., can be split up in different layer HRIs as $\mathrm{HRI} = \sum_z \mathrm{HRI}_z$, each linked with a scaling factor SF_z to the partial columns X_z:

$$\mathrm{HRI}_z = \mathrm{SF}_z X_z \qquad \textbf{Eq. 3-38}$$

We refer to Clarisse et al. (2023) for a discussion on linearity and additivity of the HRI, and why it is valid in the optical thin limit. A graphical demonstration is provided in Figure 3-17.

For the AVK calculation the SF_z are required, and we calculated these by exploiting the flexibility of the NN. Namely, we can calculate the scaling factor $\mathrm{SF}^{|z}$ corresponding to the

scenario where all NH_3 is presumed to be located in a narrow layer around z using the input parameters $z_{peak} = z$ and $\sigma = 100\,m$ for the Gaussian profile. For this calculation, an HRI input parameter is also required, and the choice was made to use the observed HRI. Note that the corresponding column satisfies:

$$\hat{X}^{|z} = \frac{\mathrm{HRI}}{\mathrm{SF}^{|z}} \qquad \textbf{Eq. 3-39}$$

The scaling factor $\mathrm{SF}^{|z}$ is used a good approximation for SF_z.

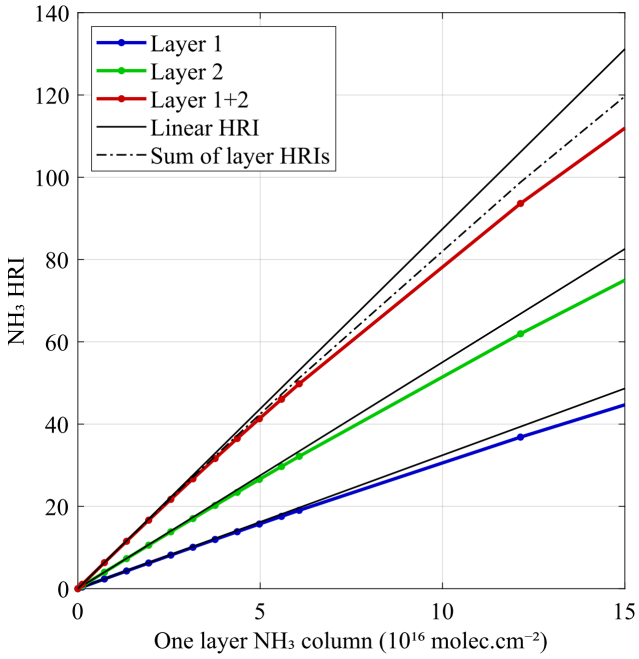

Figure 3-17: Numerical demonstration of the linearity and additivity of the HRI as a function of a change in partial column. In the blue and green scenario, NH_3 was varied at one fixed altitude. In the red scenario, partial columns in both layers were varied simultaneously. The black solid lines represent linearity, whereas the dash dotted line, being the sum of the green and blue curve, represents additivity.

Averaging kernel calculation

The averaging kernel is the matrix A which maps X_z to $\hat{X}^a$

$$\hat{X}^a = \sum_z A_z^a X_z \qquad \textbf{Eq. 3-40}$$

and can be shown to be equal to (Clarisse et al., 2023)

$$A_z^a = \frac{\mathrm{SF}_z}{\mathrm{SF}^a} \approx \frac{\hat{X}^a}{\hat{X}^{|z}} \qquad \textbf{Eq. 3-41}$$

with as before $\hat{X}^{|z}$ a column retrieval assuming that the entire column enhancement is confined to layer z. This way of defining the AVK is setup is fully self- consistent, when

$$\mathrm{SF}^a = \sum_z \mathrm{SF}_z a_z \qquad \textbf{Eq. 3-42}$$

However, to account for slight non-linearities the NN the SF^a are calculated directly, and not through the different SF_z. Consequently, the above equation is only approximately valid, and the factor $N = \sum_z A_z^a a_z$ is not exactly one. A fully consistent AVK can be calculated as:

$$A_z^a = \frac{1}{N}\frac{\hat{X}^a}{\hat{X}^{|z}} \qquad \textbf{Eq. 3-43}$$

And this is how the AVK is calculated in practice. The normalization factor also guarantees that applying the averaging kernels on the a priori vertical profile returns the retrieved column.

3.6.5. Retrieval, uncertainty, and post-filtering

Retrieval overview

The retrieval proceeds in six steps:

1. Observations are pre filtered based on valid L0, L1C and L2 availability, and a cloud flag (Section 3.6.5.2)
2. HRI is calculated and corrected where needed (Section 3.6.2).
3. Other input data to the neural network is gathered (Section 3.6.5.3)
4. Single-pixel uncertainties are calculated (Section 3.6.5.4)
5. Averaging kernels are calculated (Section 3.6.4)
6. Post-filter flags are calculated (Section 3.6.5.5)

We now detail these elements.

Pre-filtering and cloud flags

The pre-filter removes observations with invalid L1C or missing geolocation data. Scenes with a cloud fraction above 25% are also not further processed. For the near-real time product, the cloud fraction originates from the IASI L2. For the reanalysis product the cloud fraction originates from the NN-based cloud product is presented in detail in Whitburn et al. (2022). Trained with data from the latest version (v6.5) of the official L2 cloud product, it inherits all its advantages as a proven and well-validated product. The NN utilises carefully selected IASI channels as input (excluding channels affected by long-lived tracers CO_2, N_2O, CH_4, CFC-11 and CFC-12) and was shown to be temporally consistent, and coherent across the three IASI instruments. The network presented in Whitburn et al. (2022) was trained to distinguish completely clear scenes (0% cloud cover) from the rest. For the NH_3 processing, two additional networks were trained to distinguish scenes with a cloud cover below 10% and 25% respectively. With this, three cloud flags are available and these are integrated in the v4 of the reanalysed ANNI-NH_3 product.

Retrieval input data

The actual retrieval consists first of collecting the required input data, that is, the HRI of the observed spectrum and the matching auxiliary data. Most of the auxiliary data is directly taken from the IASI L2 or from ERA5, depending on the version of the product (near-real time or reanalysis). Exceptions are the surface emissivity, which originates from Zhou et al. (2013), the

HRI which is calculated from the IASI L1C data and the viewing angle, which is also part of the IASI L1C. For ERA5, all parameters are obtained via interpolation of the model's spatial and temporal grid to the exact IASI coordinates (latitude, longitude, and time). One exception is the surface temperature, which is spatially and temporally too variable for model output to be representative for an IASI footprint at a given time. Like the cloud product, a separate NN was trained for the retrieval of surface temperatures, based on the latest IASI L2. Using the output of this network ensures a temporal consistent surface temperature product. As for the NH_3 vertical profile, over ocean, the peak altitude is set to 1.4 km with a σ of 0.9 km (see Whitburn et al., 2016 for a justification). Over land, the peak altitude is set at the surface, with a width σ equal to the boundary layer height. For the near real time product, the boundary layer height is either taken from a monthly day/night climatology (but with the minimum capped at 100 meters, see Figure 3-18). The latter was built based on over 10 years of ERA5 data (from October 2007 to December 2018). The origin of the input par

Table 3-19: Summary of the origin of the ANNI input parameters for NH_3.

	Near-real time	**Reanalysis**
HRI	Calculated from L1C	Calculated from L1C
Satellite viewing angle	L1C	L1C
Surface emissivity	Zhou et al., (2013)	Zhou et al., (2013)
Atmospheric T and H_2O	IASI L2	ERA5
Surface pressure	IASI L2	ERA5
Skin temperature	IASI L2	Dedicated NN
Spread of the NH_3 profile (σ) over ocean	0.9 km	0.9 km
Spread of the NH_3 profile (σ) over land	ERA5 PBL climatology	ERA5
Peak NH_3 altitude (z_0) over ocean	1.4 km	1.4 km
Peak NH_3 altitude (z_0) over land	Surface height	Surface height

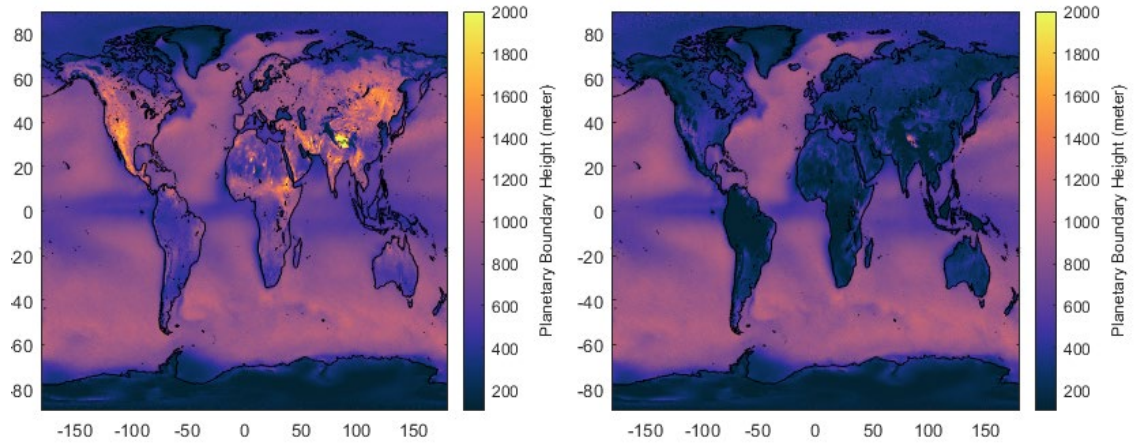

Figure 3-18: Example ERA5 climatology of the planetary boundary layer for April, morning (left) and evening (right).

Uncertainty

In the ANNI retrieval framework, per pixel uncertainty is calculated via propagation of uncertainty of the input parameters, allowing the discrimination of random and systematic uncertainties, with and without consideration of uncertainty related to the vertical profile. The treatment of uncertainties is detailed in the End-to-End ECV Uncertainty Budget (E3UB) document (D2.2).

Post filtering

As the retrieval does not use an a priori, it is poorly constrained in case of low sensitivity. Fortunately, the corresponding measurements can quite readily be filtered out. The post-filter flags retrievals with limited or no sensitivity to the measured quantity

$$\frac{1}{|\mathrm{SF}|} > 1.5 \cdot 10^{16}\ \mathrm{molec.cm^{-2}}$$

and retrievals whose HRIs are either too noisy or for which the assumed vertical profile is incompatible with the measured HRI:

$$|\mathrm{HRI}| > 1.5 \quad \text{and} \quad \hat{X}^a < 0.$$

Note on negative columns

The retrieval, by construction can return negative columns (inherited from negative HRIs and the fact that the neural network outputs the HRI-to-column ratios). While these clearly lack a clear physical interpretation, they are an integral part of the product and are not meant to be removed systematically. The use of negative physical quantities in satellite data is not new. They can for instance be found in MODIS AOD data starting from the Collection 5 (Levy et al., 2007). In this paper the authors call such negative values “statistically imperative” for creating an unbiased data set. For IASI observations of NH_3, which are expected to be measurable only in part of the data (i.e., in large areas and or certain periods, the retrieval should ideally average to 0), the necessity of having negative retrievals for an unbiased product becomes even more important. Our retrieval setup deals automatically and in a natural way with the instrumental noise through the output of HRI-to-column ratios. As long as the HRI’s are unbiased, an unbiased product is guaranteed, and the NN does not need to worry about instrumental noise and can assume that the measurements are noise-free.

It is however recommended to remove negative columns from time or space averaged data (an average over a large area, or a seasonal average), as these are not expected to exhibit important negative columns on average.

3.6.6. Examples

Single overpass

Example retrievals of the columns and associated uncertainties are shown in Figure 3-19 for a morning and evening overpass over Europe respectively. In the morning overpass, thanks to a good thermal contrast, the post filter does not remove many observations (apart from a few large negative ones). This contrasts with the evening overpass, where most observations are removed because of lack of sensitivity.

Seasonal climatology

An NH_3 seasonal climatology, based over 15 years of IASI measurements is shown in Figure 3-20.

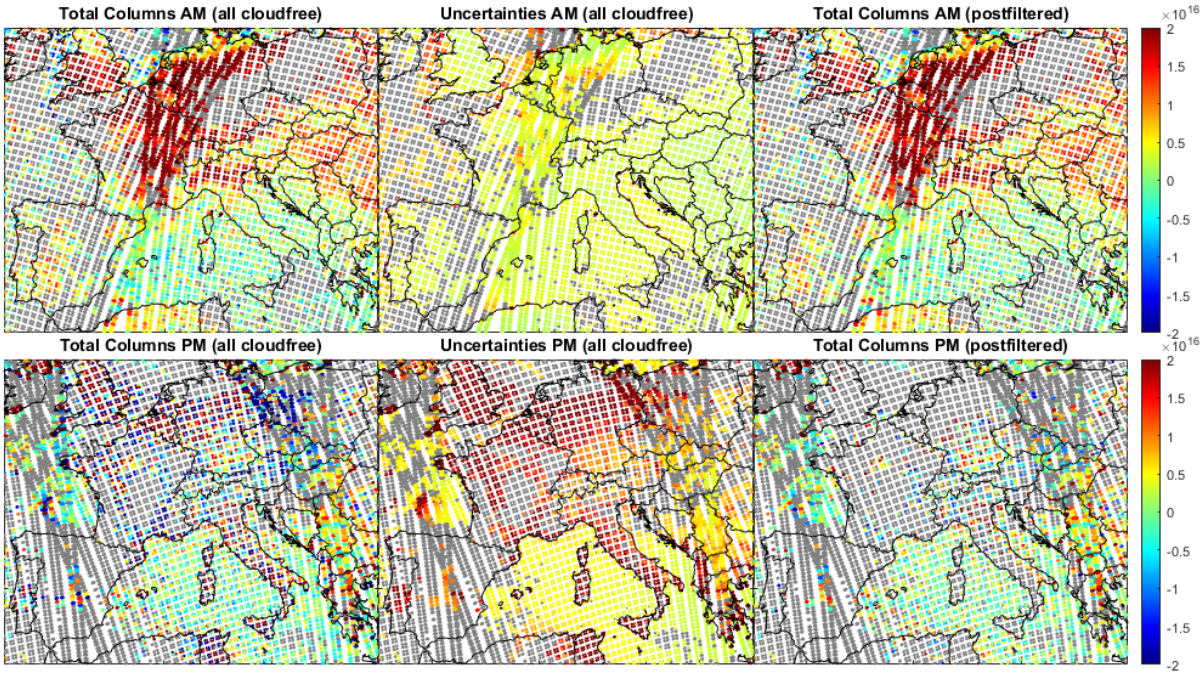

Figure 3-19: Example NH_3 retrievals from IASI-B on 24 April 2020 (AM, top; PM, bottom). Grey pixels are either cloudy or pixels that do not pass the post filter.

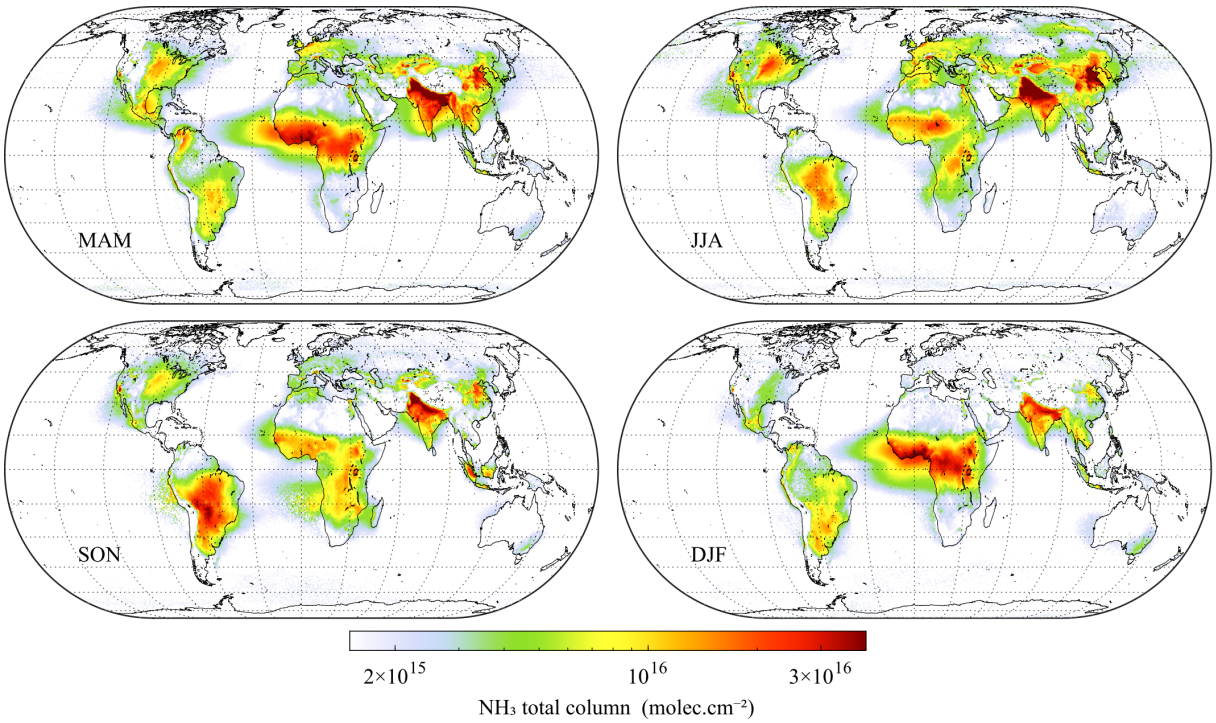

Figure 3-20: NH_3 seasonal average, derived from 0.5° by 0.5° monthly averages of the reanalysis product of ANNI v4. Data includes all measurements from IASI-A (October 2007 to December 2019), IASI-B (March 2013 to September 2022) and IASI-C (September 2019 to September 2022), with a cloud fraction below 10 %.

3.6.7. Advantages of the retrieval algorithm

Computational Efficiency. The only parameter retained from the measurement is the HRI value. Calculating these is straightforward and computational time is negligible. Calculating the neural network function is equally straightforward.

Full Spectral Range. The HRI takes into account a wide spectral range, which contains all the important NH_3 lines in the infrared, and thereby takes full advantage of the thermal infrared.

Low Dependency on the Forward Model. The forward model is only of secondary importance for the calculation of the Jacobians in the HRI and for the HRI calculated from the NN training data.

No A Priori Information. No a priori information on the column is used. This means that all the information from the final measurement comes from the spectral measurement (but potentially with very large associated uncertainties). Therefore, in contrast to optimal estimation approaches, no averaging kernel needs to be applied when carrying out comparison with other measurements/models. A priori information on the vertical profile shape is used but can be undone with averaging kernels.

Full Atmospheric State. Because the number of input parameters is not limited in the NN, the full temperature, humidity, and pressure profiles can be taken into account. This property is shared with the spectral fitting approaches.

Full Uncertainty Analysis. By perturbing the input parameters, a full uncertainty characterization can be made of how the uncertainty of each of the input parameters

propagates to the final result. This analysis can be carried out on a per-pixel basis and allows separating of systematic and random uncertainty contributions.

Reduced Bias. Rather than mapping the input parameters directly to a NH_3 column, the output of the NN is a scaling factor, which after multiplication with the HRI gives the column. In this way, the instrumental error on the HRI is translated in a linear way in an error on the column, and negative columns become possible. At the same time, this implies that the algorithm itself is relatively unbiased by design (this is assuming that the HRI values are not biased).

3.6.8. Comparison with an OEM retrieval

Here, we present the results of an independent intercomparison that was conducted between the ANNI v4 retrieval output and that of an optimal estimation approach which relies on spectral fitting.

For the optimal estimation retrieval, the Atmosphit forward and inverse model was used (Coheur et al., 2005), which is the same tool whose forward model is used for the construction of the ANNI training database. The optimal estimation was set up as follows. The retrieval range was set to 900 to 975 cm^{-1}. Total columns of NH_3 were retrieved with a fixed vertical profile, using the same parametrization as in ANNI NRT. The NH_3 variance was set to 1000%, corresponding to an almost unconstrained retrieval. Together with NH_3, H_2O was retrieved in 10 partial columns, with the a priori coming from the IASI L2. Total columns of CO_2, O_3 and CFC-12 were retrieved as well as the surface temperature. Spectral emissivity was taken from Zhou et al. (2013). Before presenting the results, it should be emphasized that despite the similarities in both retrieval approaches (same input parameters, vertical profiles, forward model), no perfect agreement is expected because of: (1) use of a narrower spectral range in the optimal estimation retrieval; (2) different propagation of instrumental noise to the retrieval result; (3) limitations of the fitting model (e.g. with respect to fitting water vapour or surface emissivity); (4) errors related to the imperfect training of the neural network.

For the comparison, two days were selected, one over Europe and one over North America, with relatively high NH_3 columns. The results are shown in Figure 3-21. Intercepts, mean, and median differences are all in the order of 10^{15} molec.cm^{-2} or below. Regression slopes, calculated using iteratively reweighted least squares to remove the impact of outliers, are 0.97 and 1.05. While the scatter around the 1--1 lines is not negligible (with standard deviation of the differences around 3-4 10^{15} molec.cm^{-2}), these numbers demonstrate the overall consistency of both retrieval approaches and do not indicate a significant bias.

The last detailed global validation of the IASI NH_3 product was based on a comparison of ground-based FTIR measurements of NH_3 with the LUT-based NH_3 product, where a low bias around 35% was found (Dammers et al., 2016). Since then, two independent validation studies have been conducted. One study (Guo et al., 2021) compared IASI ANNI v3 with in situ measurements in Colorado, U.S. and found regression slopes ranging from 0.78 to 1.1, and intercepts of the order of 1 to 2 10^{15} molec.cm^{-2}. A second study (Wang et al., 2020) compared IASI NH_3 columns with columns obtained from FTIR measurements in Hefei, China. Here, mean differences around 3.5 10^{15} molec.cm^{-2} (IASI being lower) were found and regression slopes close to one. Given the results of the comparison with the optimal estimation method, we do

not expect any significant bias in ANNI v4 for columns above 10^{16} molec.cm^{-2} in comparisons that correct for the vertical profile assumption of the retrieval.

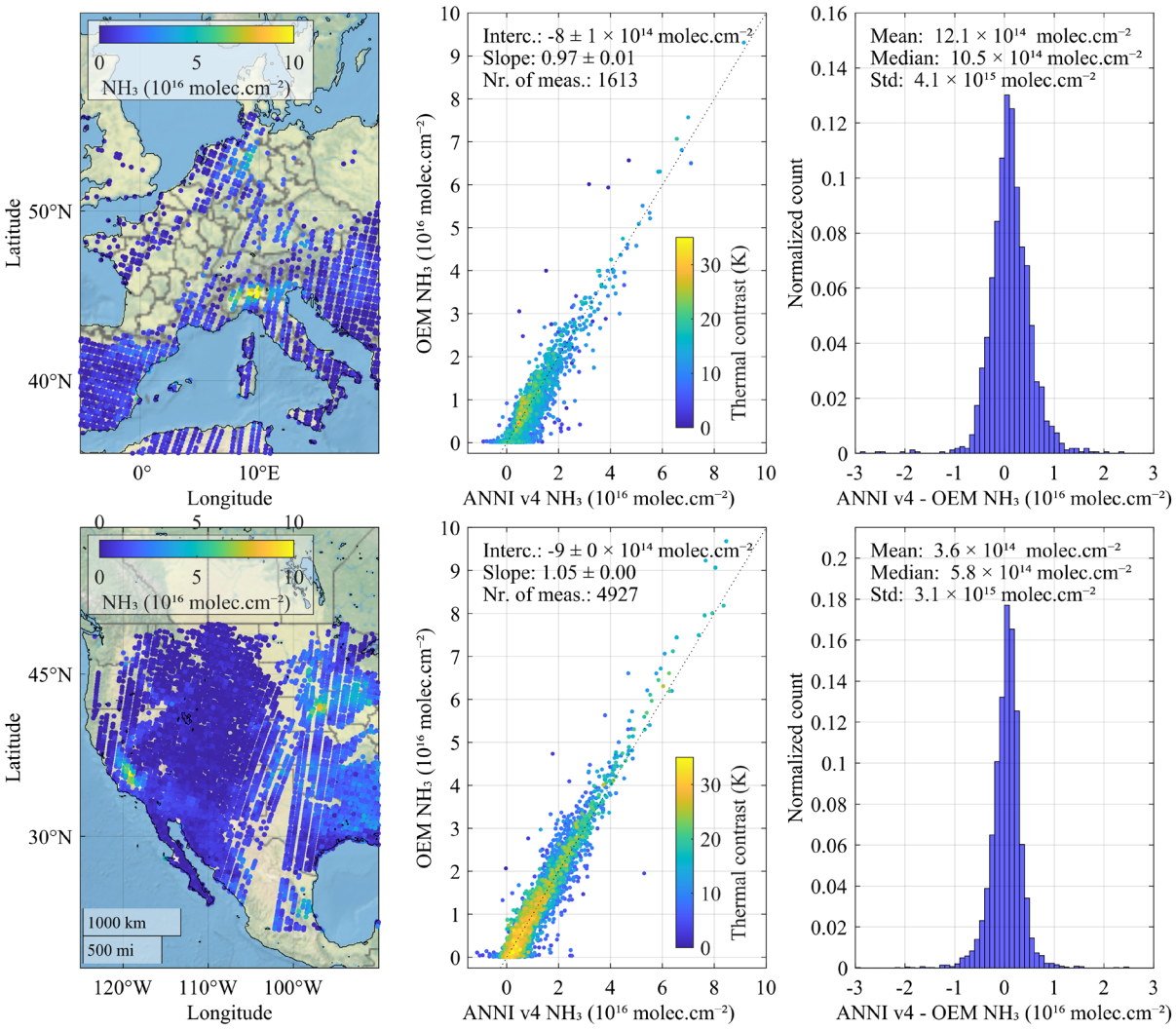

Figure 3-21: Comparison between ANNI v4 NH_3 columns and retrievals based on optimal estimation for two scenes, one over Europe (top panels, 18 April 2013, Metop A morning overpass) and North America (bottom panels, 6 May 2021, Metop B morning overpass). The left panels depict the optimal estimation retrieved columns. The middle panels are scatter plots between the two retrievals, where each observation is colour coded according to thermal contrast (brightness temperature of the surface minus the temperature at half the boundary layer height). The right panels summarize the comparison by means of histograms of the differences.

4. Level-3 algorithms

4.1. Tropospheric nitrogen dioxide (L3-NO_2) from OMI and TROPOMI

4.1.1. Overview

The L3 NO_2 data products for OMI and TROPOMI are developed with the aim of providing user-friendly datasets that support both scientific analysis, such as long-term trend analysis and low-frequency climate variability and address public interest. Generating L3 NO_2 data requires binning of L2 data onto a regular two-dimensional latitude-longitude grid in a specified temporal period, i.e. over a day or a month.

In this project, we utilize OMI L2 NO_2 data from the QA4ECV v1.1 product (Boersma et al., 2018) available on www.temis.nl/airpollution/no2col/no2regioomi_qa.php and TROPOMI L2 NO_2 data v2.3.1 available on https://data-portal.s5p-pal.com/browser/. Table 4.1 summarizes the key characteristics of all morning sensor instruments and their L2 processors. The gridding and uncertainty calculation for L3 processing are described in the following sections.

Table 4.1: Summary of characteristics of the morning sensor instruments and L2 data products.

Instrument	Operational period	Ground-pixel resolution	Equator crossing time	Global coverage	L2 processor
OMI	2004 – 2021	24 x 13 km^2	13:45 LT	1-2 days	QA4ECV v1.1
TROPOMI	2018 – 2021	5.5 x 3.5 km^2	13:30 LT	1 days	v2.3.1

4.1.2. Data gridding approach

The OMI and TROPOMI L3 data are generated in a 2-step approach:
In the first step, *daily* NO_2 retrieval are gridded onto so-called superobservations. To calculate the superobservations, only retrievals with qa-values of >0.75 were used, which corresponds to good-quality retrievals over (nearly) cloud-free scenes. Moreover, the retrievals made in the descending part of the orbit are removed, as these showed a different distribution in retrievals likely due to these observations not being included in the data assimilation in the TM5-MP chemistry transport model to retrieve the stratospheric column (see Glissenaar et al. (2025)). The superobservations represent the best estimate of the NO_2 fields at regular grid resolution and are comparable to model simulations of NO_2 columns at that grid resolution at the overpass time of the sensor. Details of the superobservation approach, and associated superobservation uncertainties can be found in Rijsdijk et al. (2025).

In the second step, monthly means are being calculated from the daily superobservations. These spatial averages are aggregated over time and averaged, leading to the desired L3 product. Figure 4.1 below gives a schematic example of the procedure applied to generate the OMI and TROPOMI L3 NO_2 monthly means.

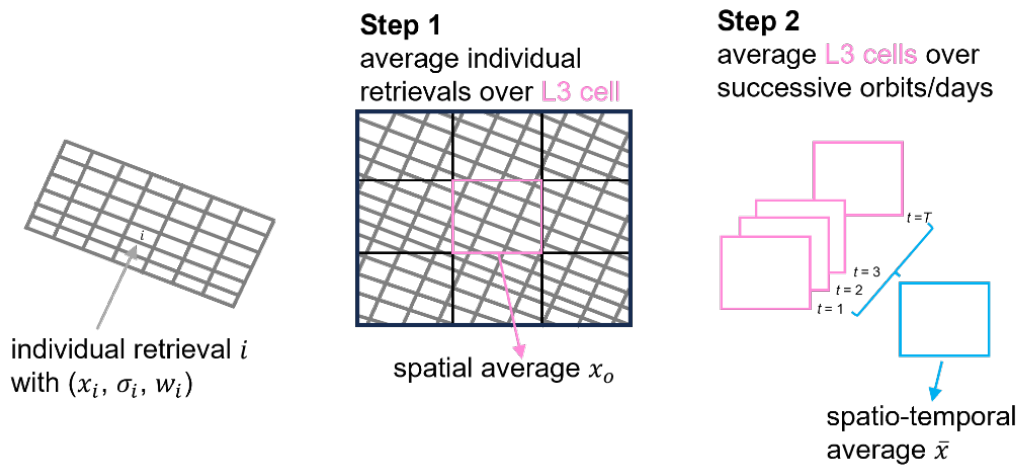

Figure 4-1: Schematic example of the procedure to calculate spatio-temporal (gridded) averages of retrieved NO_2 columns for OMI and TROPOMI.

Step 1 concerns the spatial averaging, sometimes called tiling, of valid retrieved values of the individual pixels (x_i) with weights (w_i) that represent the pixel area (a_i) spatially overlapping with the L3 grid cell ($w_i = a_i$). This results in a best estimated ('tile' or 'superobservation') $x_{o,t}$ of the gridded L3 column:

$$x_{o,t} = \frac{\sum_{i=1}^{N}(w_i x_i)}{\sum_{i=1}^{N} w_i} \qquad \textbf{Eq. 4-1}$$

with N the number of valid observations in the L3 cell. We take an area-weighted averaging approach, because the retrieval provides column densities (x_i) that hold for pixels with variable area sizes that (partially) overlap the grid cell the spatial average is taken on (see Figure 4-1). The total number of NO_2 molecules accumulated over valid pixels should thus be weighted by the pixel area overlapping with the L3 grid cell (a_i).

The spatial average is determined on a (regular) grid on a per-orbit basis. The spatial average for a grid cell is only determined if the combined individual retrievals x_i cover at least 30% of the grid cell following Rijsdijk et al. (2025).

Step 2 averages the gridbox-mean values $x_{o,t}$ obtained in step 1 over time, again in a weighted fashion to account for different degrees of representativity ($w_{o,t} = 1 - r$). r is high for superobservations with a large representativity uncertainty and low for superobservations with almost no representativity uncertainty. This representativity value depends on coverage – higher coverage results in a smaller representativity error – but also other factors such as sensitivity to systematic sampling. For more detail on the representativity error on how this is calculated, we refer to the End-to-end uncertainty budget document (D2.2 issue 2, Precursors_cci+_D2.2_E3UB_02_03). Taking a weighted average like this means that superobservations with a low representativity error get more weight in the temporal average than superobservations with a high representativity error. This results in the following estimate of the spatially and temporally averaged L3 column $\bar{x}$:

$$\bar{x} = \frac{\sum_{t=1}^{T}(w_{o,t}x_{o,t})}{\sum_{t=1}^{T} w_{o,t}} \qquad \textbf{Eq. 4-2}$$

with T the total number of valid superobservations in the period over which the averaging is performed.

The spatial resolution for the L3 gridding has been selected such, that multiple L2 pixels fall in one cell on one day, irrespective of whether these pixels are valid or not. In practice this means that the following grid resolutions are considered practical for OMI and TROPOMI NO2:

	0.2°x0.2°	0.5°x0.5°	1.0°x1.0°	2.0°x2.5°
TROPOMI	✓	planned	✓	✓
OMI	✓	planned	✓	✓

For OMI, the data product with spatial resolution 0.2° x 0.2° is a tentative one, which does not include the spatial representativity component in the calculation of the L3 data and uncertainties, because the grid cell is generally smaller than a single OMI pixel.

Key gridded variables

From the L2 products, the key gridded variable is the tropospheric NO_2 column. In line with user requirements, the L3 products also include several detailed intermediate results (slant columns, clear and cloudy-sky air mass factors, averaging kernels, etc.). Additionally, input data (surface albedo, cloud properties, vertical a priori profiles, etc.) are included. Furthermore, NO_2 tropospheric column uncertainties are provided that were estimated using a detailed uncertainty propagation described in **E3UB**.

Examples of the TROPOMI and OMI monthly mean tropospheric NO_2 columns for January and June 2019 are shown in Figure 4-2. Generally, the two instruments show good agreement on NO_2 column levels, as well as the spatial distribution. OMI shows significantly less spatial coverage than TROPOMI. This is mainly due to the Row Anomaly phenomenon which has affected OMI since 2007, and several rows of the orbit have invalid retrievals. Moreover, OMI has higher uncertainties than TROPOMI due to its reduced spatial coverage, larger pixel size, instrument degradation in the later years, and TROPOMI's improved slant column uncertainties.

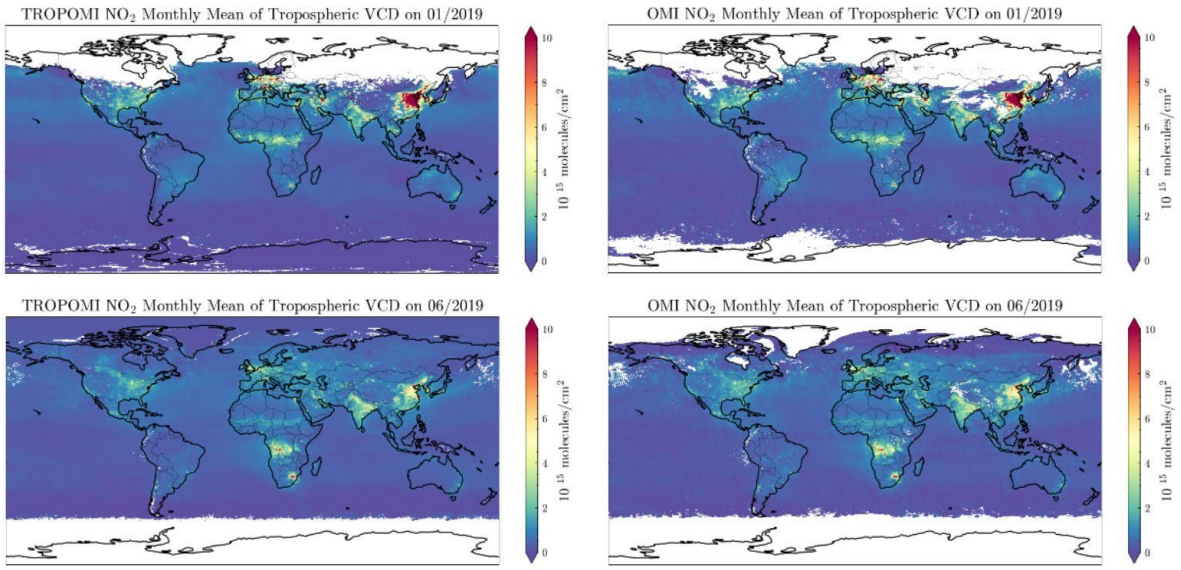

Figure 4-2: Monthly mean tropospheric NO_2 columns from L3 products of OMI and TROPOMI for January and June 2019, as well as the total uncertainty for June 2019.

OMI Row Anomaly

OMI has been affected by the so-called Row Anomaly, wherein several rows show abnormal radiances and irradiances making the retrievals invalid. The phenomenon started in 2007 and stabilized in 2014, and after 2014 it affects about 57% of the north part and about 30% of the south part of the orbit. The rows affected are in the middle of the orbit track, meaning that most valid retrievals are performed at higher viewing angles. To exclude row anomaly related trends, and to ensure higher consistency we sample OMI and TROPOMI following the row anomaly pattern. Specifically, we sample OMI throughout the mission period (2004-2021 here) excluding all rows affected later by the row anomaly, and during the overlapping period of the two instruments we sample TROPOMI only when OMI has a valid observation over the same location. Figure 4-3 shows the OMI and TROPOMI NO_2 monthly mean timeseries over the remote Pacific and over the 1x1 pixel over Beijing. Row anomaly sampled OMI shows larger NO_2 columns over the Pacific between 2004-2007 that better match with the monthly mean NO_2 levels in later years. Apparently, sampling OMI NO_2 is viewing zenith angle-dependent, especially in this pristine region where NO_2 is very low. This VZA-dependency of the OMI L2 NO_2 data is under investigation and is likely associated with the usage of the LER surface reflectivity climatology rather than the directional surface reflectivity climatology (DLER) in the AMF calculation of the QA4ECV v1.1. data. The effect is less prominent over polluted regions or hotspots, possibly because sampling differences there are more driven by the strong variability in polluted NO_2 (which depends on wind direction and differences in emissions and NO_2 lifetimes). Co-sampling OMI and TROPOMI has a small effect for large uniform regions but over hotspots, such as Beijing, where NO_2 varies throughout the month TROPOMI NO_2 agrees better with OMI when co-sampling.

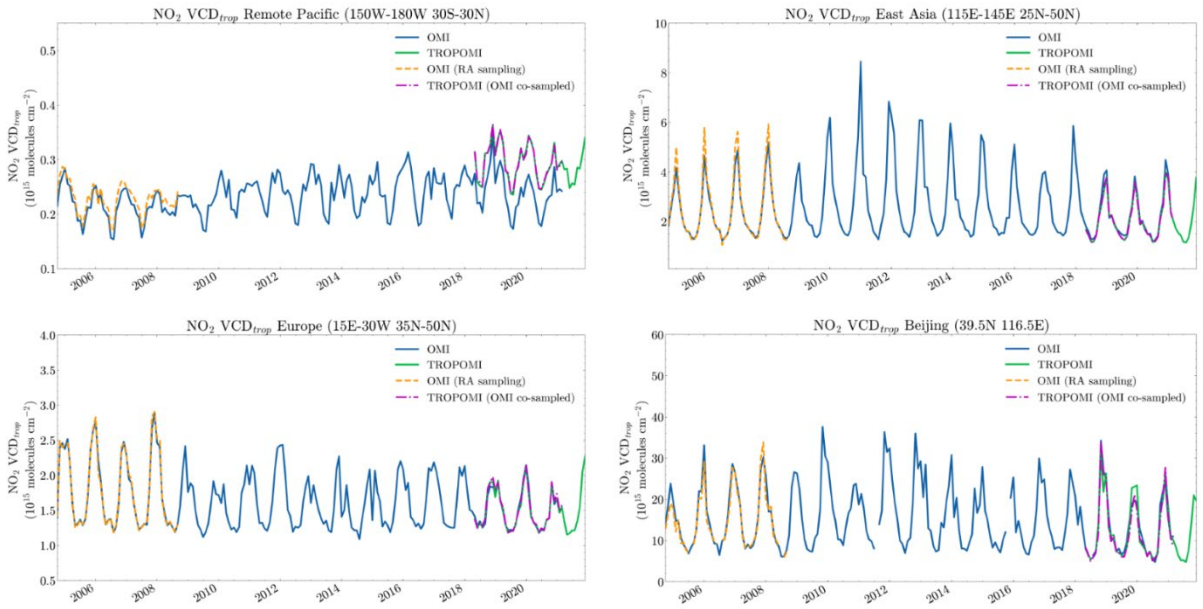

Figure 4-3: Timeseries of OMI and TROPOMI L3 monthly NO_2 tropospheric columns, as well as OMI sampled excluding row anomaly affected rows, and TROPOMI co-sampled with OMI over a remote Pacific region, East Asia, Europe and Beijing.

Vertical dimension

Gridded full averaging kernels are provided for each grid cell as well as total and tropospheric air mass factors, and the tropopause layer index. Using these gridded variables, the tropospheric averaging kernel can be derived, which can be used by modellers to ensure a fair comparison with the satellite retrieved L3. The sensitivity of satellite measurements to trace gases (e.g. NO_2, HCHO, SO_2) varies vertically. More specifically, satellite retrievals are less sensitive to these trace gases when they reside close to Earth's surface. The averaging kernel is proportional to this measurement sensitivity profile and provides the relation between the retrieved quantities and the true tracer profile. For a fair comparison between a modelled column and the satellite retrieval this sensitivity should be accounted for, which can be done by applying the averaging kernel to the modelled vertical distribution. This allows users to "interpret" the model column as the satellite would retrieve it were it the true column.

The averaging kernel is provided in the 34 vertical layers of the TM5 model, and the pressure for the upper and lower interface levels of each layer can be calculated using the surface pressure and the TM5 hybrid A and B coefficients. The gridded averages of these are also provided in the data product. The vertical profile should be adjusted to be in the same pressure grid, and the NO_2 units should be the same as in the L3 file. Figure 4-4 presents an example of the tropospheric and full averaging kernel over Beijing for January and July 2019.

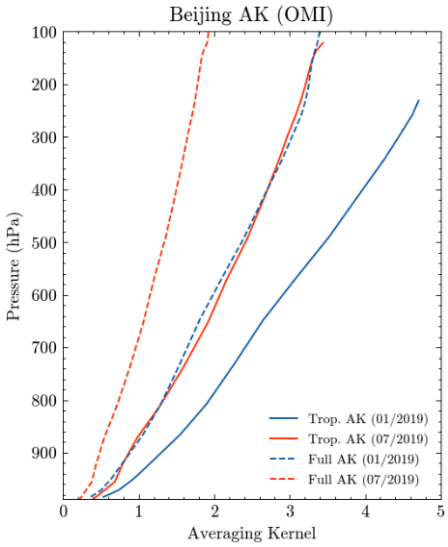

Figure 4-4: Tropospheric and full averaging kernel over Beijing for January and July 2019 from OMI L3.

Effective date and effective fractional day

For monthly averages, the day of the month is also gridded to provide an effective date. This gives an indication of the time coverage of the provided monthly means. The effective fractional day of each observation is also added in the grids, in local solar time. This gives an indication of the averaged overpass time of the provided means.

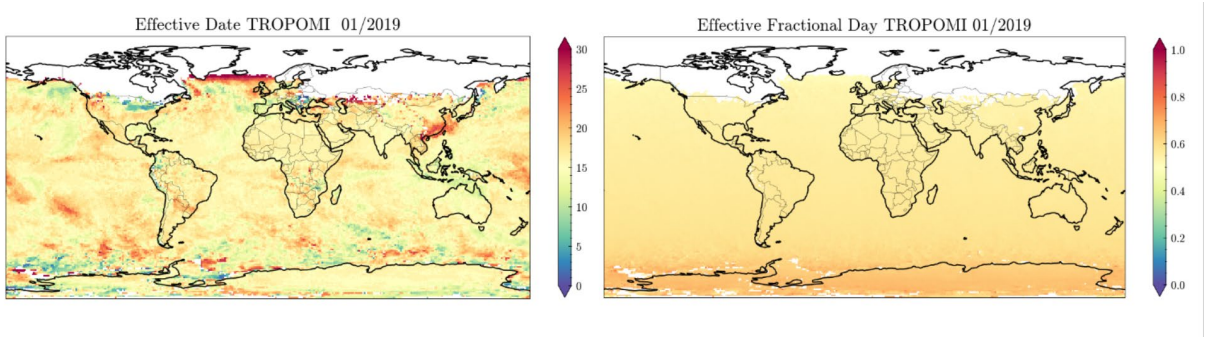

Figure 4-5: Effective date (day of the month) and fractional day for January 2019 for TROPOMI L3.

Observation geometry

All the gridded variables in each grid cell are averaged using many ground pixels, with sometimes different observation conditions. We provide cloud and surface properties that are angle dependent to support the interpretation of the results, however, we do not provide averages of solar and viewing angles in the L3 data product.

Global attributes

In addition to the netcdf conventions, several additional information is provided in the product global attributes, such as

- The list of L2 files used to calculate the L3 file.
- The L1 and L2 versions (SCD, AMF).
- The L3 and gridding software version
- The L2 data selection criteria

4.2. Tropospheric nitrogen dioxide (L3-NO_2) from GOME, SCIAMACHY and GOME-2

4.2.1. Overview

The L3 NO_2 data products for morning sensors are developed with the aim of providing user-friendly datasets that support both scientific analysis, such as long-term trend analysis and low-frequency climate variability, and address public interest. Generating L3 NO_2 data requires binning of L2 data onto a regular two-dimensional latitude-longitude grid in a specified temporal period, i.e. a day or a month.

In this project, we utilize GOME and SCIAMACHY L2 NO_2 data from the QA4ECV v1.1 product (Boersma et al., 2018), as well as GOME-2/MetOp-ABC L2 NO_2 data from the AC-SAF prototype product. Table 4-1 summarizes the key characteristics of all morning sensor instruments and their L2 processors. The gridding and uncertainty calculation for L3 processing are described in the following sections.

Table 4-1: Summary of characteristics of the morning sensor instruments and L2 data products.

Instrument	Operational period	Ground-pixel resolution	Equator crossing time	Global coverage	L2 processor
GOME	1995 – 2003	320 x 40 km^2	10:30 LT	3 days	QA4ECV v1.1
SCIAMACHY	2002 – 2012	60 x 30 km^2	10:00 LT	6 days	QA4ECV v1.1
GOME-2A	2007 – 2021	80 x 40 km^2; 40 x 40 km^2 [(5)]	09:30 LT	1 day	AC-SAF prototype
GOME-2B	2013 – present	80 x 40 km^2	09:30 LT	1 day	AC-SAF prototype
GOME-2C	2019 – present	80 x 40 km^2	09:30 LT	1 day	AC-SAF prototype

4.2.2. Data gridding approach

Our L3 processing for morning sensor NO_2 utilizes a HARP data harmonization toolkit https://atmospherictoolbox.org/harp/), developed by the European Space Agency for handling scientific earth observation data. For the L3 NO_2 product from morning sensors, only forward-scan pixels are used in the gridding process. Cloudy measurements, where most of tropospheric NO_2 resides below the cloud layer, are excluded since satellite observations could not detect NO_2 columns beneath clouds, resulting in significant uncertainties. Therefore, these cloudy measurements (cloud radiance fraction > 0.5) are not included in the L3 data processing. However, for stratospheric NO_2 columns, no cloud filtering is applied. Additionally, low-quality data with high spectral fitting errors are excluded from the L3 processing to ensure the accuracy of the resulting data products.

Morning sensors, including GOME, SCIAMACHY, and GOME-2, have larger ground pixel sizes compared to afternoon sensors such as OMI and TROPOMI. This can lead to significant grid effects if each measurement is assigned to a single grid cell based solely on the centre

[(5)] Since tandem operation with GOME-2B on 15 July 2013.

coordinates of the ground pixel, without accounting for the pixel geometry and extension. To address this, the gridding process considers the overlapping area between the satellite ground pixel and the latitude-longitude grid. For grid cells that partially overlap with a satellite pixel, a weighting factor is applied based on the ratio of overlap (a satellite pixel fully covering an entire grid cell is considered to have 100 % overlap). The weighting and count vectors are used to apply this weighted average consistently on the L3 spatial gridding to calculate the mean value and uncertainty as Eq. 4-3:

$$x_g = \frac{\sum_{i=1}^{N_{eff}} x_i \times w_i}{\sum_{i=1}^{N_{eff}} w_i} \qquad \textbf{Eq. 4-3}$$

where x_g is the gridded column, while x_i represents each individual measurement overlapping within the grid cell. The weighting is denoted w, which is the percentage of the grid cell covered by the satellite pixel, and N_{eff} is the effective population size, determined by the number of available observations of sensors within the L3 grid resolution.

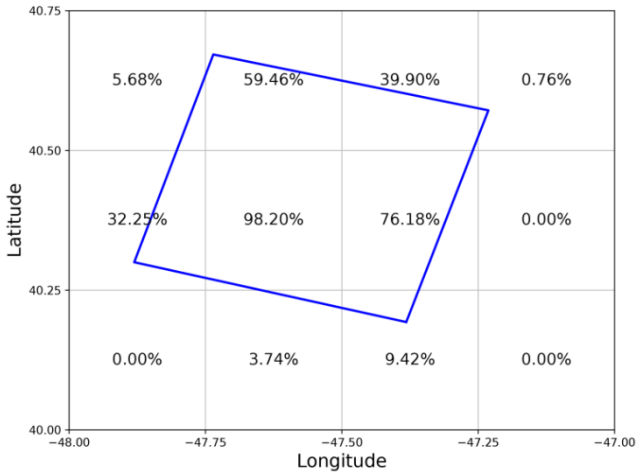

Figure 4-6: An example of GOME-2A ground pixel (blue) overlaid on a 0.25° x 0.25° latitude-longitude grid (grey). The percentage of overlap (weighting, w) for each grid box is denoted. (image credit: Chan et al., 2023)

Selecting an appropriate resolution for the latitude-longitude grid is essential for processing the L3 products. The L3 product should retain the original spatial features captured in the L2 data, which typically has higher spatial resolution. However, it is also important to maintain a reasonable file size to ensure the data remains user-friendly. To select the best spatial resolution for the L3 product, we have analysed the binning results with different resolutions. We looked into the spatial smoothing/averaging effect over polluted regions such as Northeast Asia, as this region is expected to show strong spatial gradients of tropospheric pollutions.

For GOME-2, the results show that gridding data at a higher spatial resolution better preserves the original instrument footprint, while a rather strong smoothing/averaging effect is observed when data is gridded at a lower spatial resolution (i.e. 0.5° x 0.5°, 1° x 1°). While gridded data at a 0.2° x 0.2° resolution exhibit some smoothing/averaging effects, they

capture spatial variations reasonably well. The difference between data gridded at 0.1° x 0.1° and 0.2° x 0.2° resolution show small differences. However, 0.5° x 0.5° resolution data show a relatively underestimation of tropospheric NO_2 columns over polluted hotspots. The comparison of GOME-2 data gridded at different spatial sampling resolutions indicates that 0.2° x 0.2° resolution is a balance, preserve the satellite resolution as well as capturing the spatial variations of NO_2. In addition, the absolute values of L3 data show consistent with the L2 data. Therefore, we concluded that 0.2° x 0.2° resolution is a suitable choice for GOME-2 L3 products.

For SCIAMACHY, which has a nadir pixel size of 30 x 60 km^2, comparable to GOME-2 (40 x 80 km^2), L3 products on 0.5° x 0.5° resolution grid show spatial distributions and values similar to those of L2 products. Therefore, 0.5° x 0.5° resolution was selected for SCIAMACHY L3 products, following the same gridding approach as for GOME-2 to ensure consistency. However, the difference in global coverage time between SCIAMACHY and GOME-2 should be noted. While SCIAMACHY takes 6 days to achieve global coverage, GOME-2 provides daily global measurements. This discrepancy in global coverage time leads to differences in data sampling for the monthly L3 products during their overlapping period, resulting in slight variations in the NO_2 climate data records between two instruments.

GOME overlaps operationally with SCIAMACHY for ~ 1 year (August 2002-June 2003), although there is a gap of 3.5 years between GOME and GOME-2. Both GOME and SCIAMAHY L2 datasets from QA4ECV v1.1 are derived using calibrated L1 data and state-of-the art retrieval algorithms with consistent ancillary data inputs. However, since GOME has a relatively low spatial resolution of 320 x 40 km^2 compared to SCIAMACHY and GOME-2, its L3 spatial resolution should be carefully evaluated to ensure creation of consistent NO_2 climate datasets. To assess the impact of the differences in the ground pixel area between GOME and SCIAMACHY measurements, we compared the original GOME and SCIAMACHY data with spatially down-sampled SCIAMACHY measurements, using only the data points collected by both instruments on the same day. The spatial resolution of GOME approximated using SCIAMACHY measurements corresponds to an average of approximately five adjacent pixels. We explicitly corrected for the difference in ground pixel size between GOME and SCIAMACHY by applying the appropriate ratio grid of correction factors.

When projecting large footprints onto a finer grid (oversampling), measurement information is inevitably spread across multiple L3 grid cells, leading to smoothing and potential aliasing effects, where information from outside a given grid cell can influence its value. Also, the L2 averaging kernel shape and footprint extent are not fully preserved in the L3 gridding process, which can dampen fine-scale spatial features. To mitigate these effects, the L3 NO_2 product from morning sensors applies the area-weighted gridding approach based on the actual shape and orientation of the satellite footprints (see eq. 4.2-1 and Fig. 4-6). This method helps to partially address the oversampling and redistribution issues inherent in the gridding process.

Furthermore, to maintain consistency across datasets, we use the same L3 spatial resolution for morning sensors as for afternoon sensors (e.g. OMI, TROPOMI), although the latter have finer native resolutions. This ensures a harmonised framework for analysing NO_2 observations across multiple instruments and different times of day.

4.2.3. Datasets

We describe below the key variables and provide details about specific information of L3 Morning NO2 CDR products calculated using HARP functionalities.

Key gridded variables

From the L2 products, the key gridded variables are total, stratospheric, and tropospheric NO_2 columns. In line with user requirements, the L3 products also include several detailed intermediate results (slant columns, clear and cloudy-sky air mass factors, averaging kernels, etc). Additionally, input data (surface albedo, cloud properties, vertical a priori profiles, etc) and observation geometry are included. Furthermore, tropospheric NO_2 column uncertainties are provided that were estimated using a detailed uncertainty propagation described in the E3UB document. See example L3 output results below.

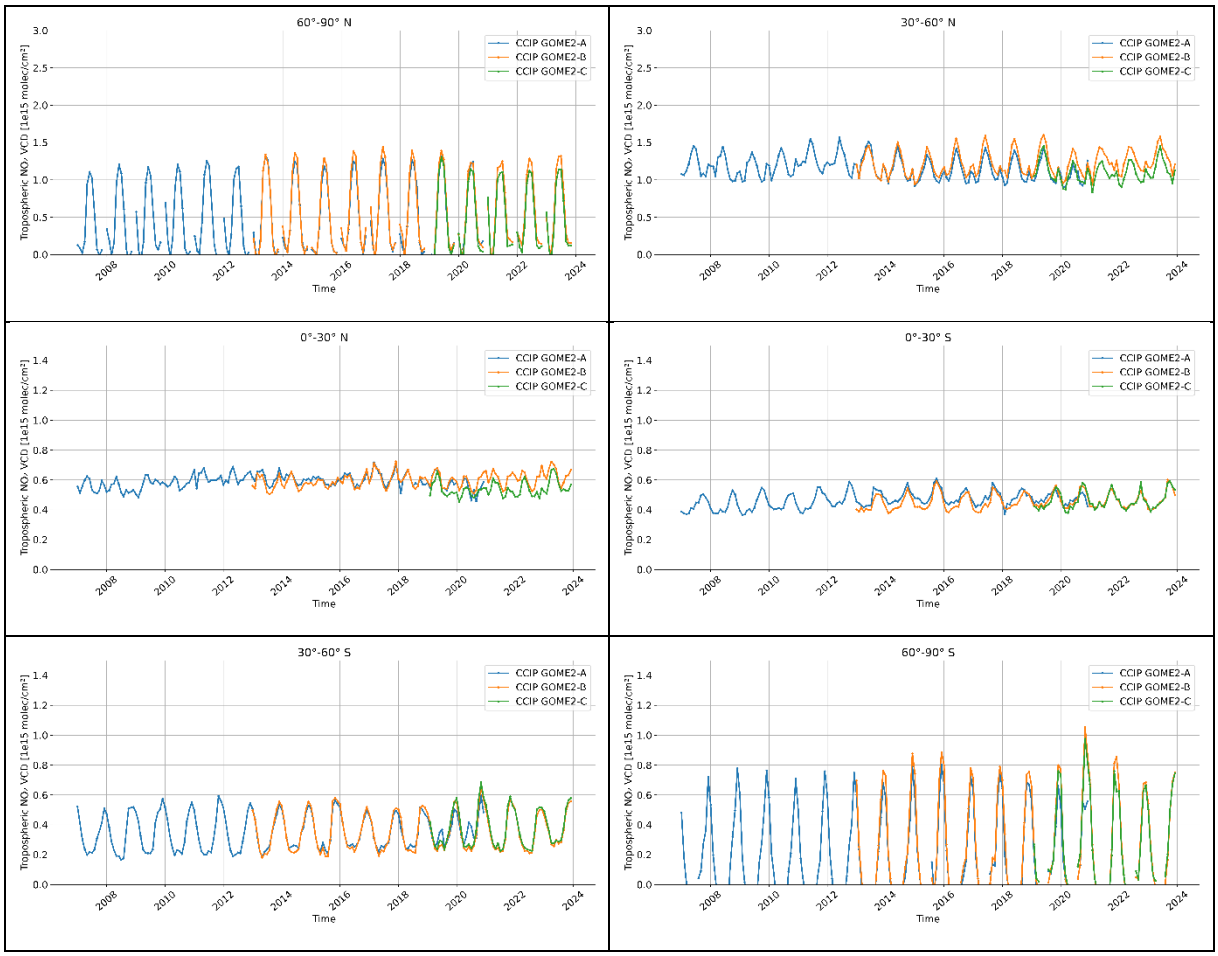

Figure 4-7: Time series of monthly zonal averages of tropospheric NO_2 columns from GOME-2A, GOME-2B and GOME-2C across different latitudinal bands from 2007 to 2023.

The consistency of the L3 product across the three GOME-2 sensors is investigated. Figure 4-7 presents the monthly mean time series of tropospheric NO2 vertical column densities for different latitudinal bands over the period from 2007 to 2023. Although small discrepancies among three GOME-2 instruments are observed, primarily due to differences in the instrument characteristics, L1 calibration, and sensor degradation, they generally exhibit good

agreement and consistency during overlapping periods as well as in the overall temporal trends.

The global maps of monthly L3 tropospheric NO_2 columns and tropospheric AMFs from GOME-2A, GOME-2B, and GOME-2C for February 2019 are presented in Fig. 4-8 and Fig. 4-9. Overall, the spatial distributions and values of tropospheric NO_2 columns and AMFs from the three sensors show good agreement. However, GOME-2A shows more missing data compared to GOME-2B and GOME-2C. This is mainly attributed to less spatial averaging and instrument degradation. The swath width of GOME-2A was reduced from 1920 km to 960 km in July 2013, while the swath widths of GOME-2B and GOME-2C remain unchanged. Additionally, the noise levels of GOME-2A are higher than those of GOME-2B and GOME-2C due to instrument degradation.

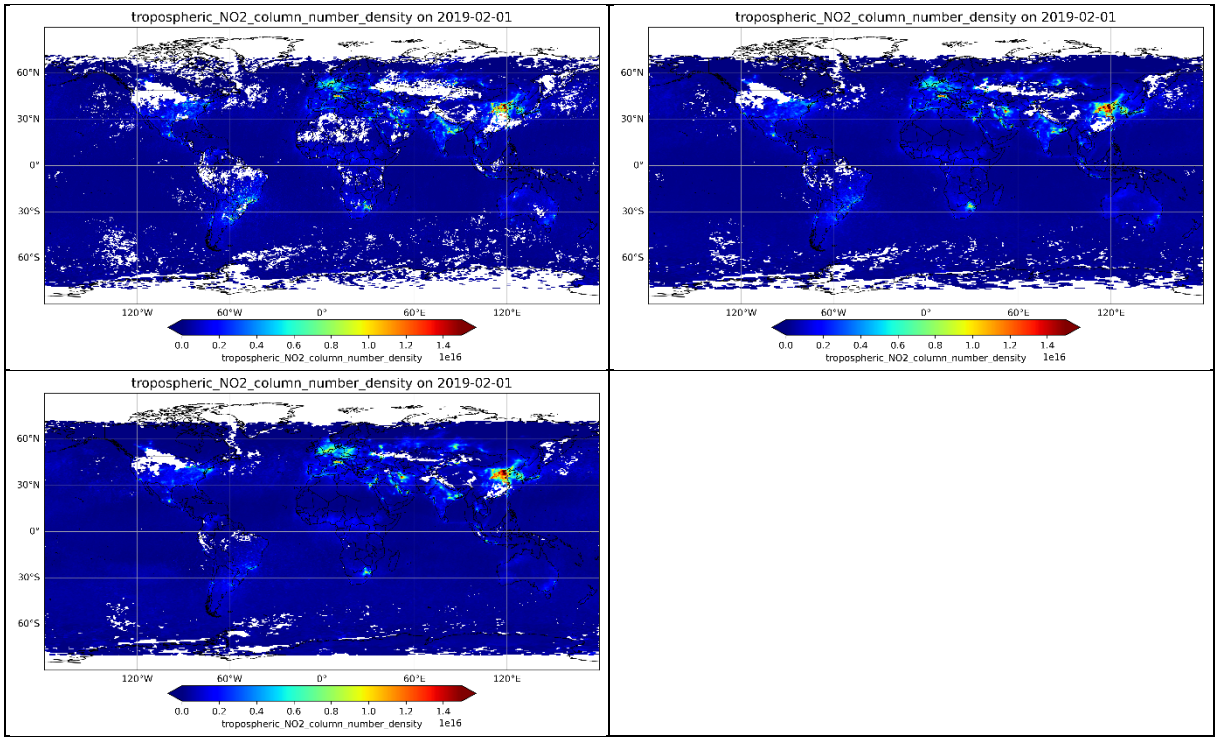

Figure 4-8: Monthly averaged tropospheric NO_2 columns at 0.2° × 0.2° resolution from L3 products of GOME-2A, GOME-2B and GOME-2 for February 2019.

To evaluate the consistency and long-term trends of tropospheric NO_2 columns from all morning sensors, including GOME, SCIAMACHY, and three GOME-2 instruments, we analysed time series covering the entire measurement period for six regions of interest worldwide using L3 NO_2 products (Figure 4-10). The selected regions are eastern China (25-45 °N, 105-125 °E), the Pacific Ocean (30 °S-30 °N, 180-210 °E), biomass burning regions in northern Africa (15 °S-0 °N, 10-35 °E), western Europe (35-50 °N, 10 °W-20 °E), the eastern cost of the United States (35-40 °N, 275-290 °E), and the Middle East (28-38 °N, 34-60 °E).

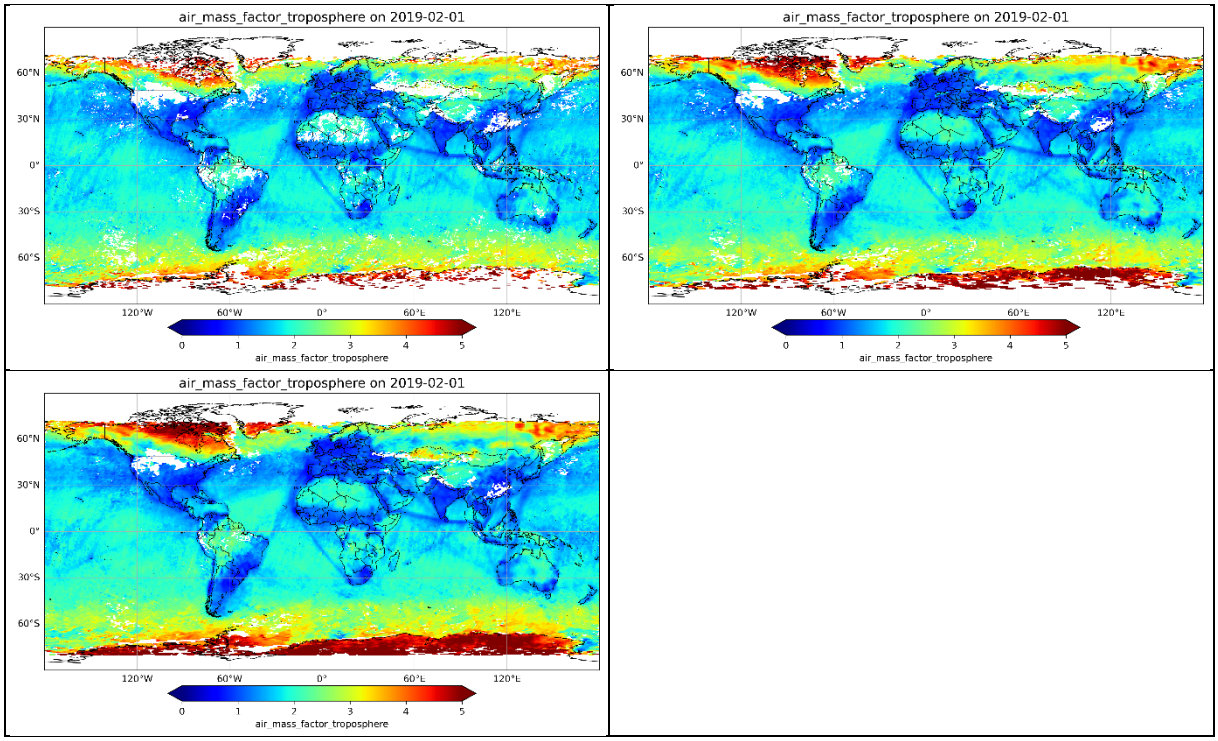

Figure 4-9: Monthly averaged tropospheric air mass factors at 0.2° × 0.2° resolution from L3 products of GOME-2A, GOME-2B and GOME-2 for February 2019.

Overall, tropospheric NO_2 columns from all morning sensors L3-NO2 CDR show a good level of agreement in monthly averages across most regions, confirming their suitability for long-term trend analysis (from 1995 to present).

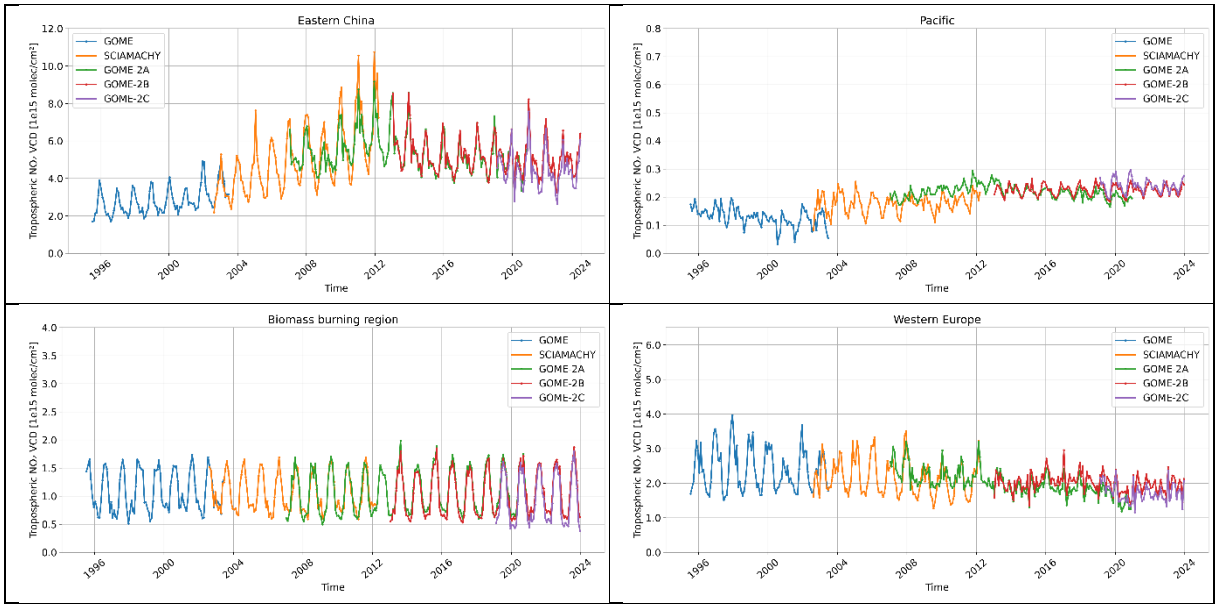

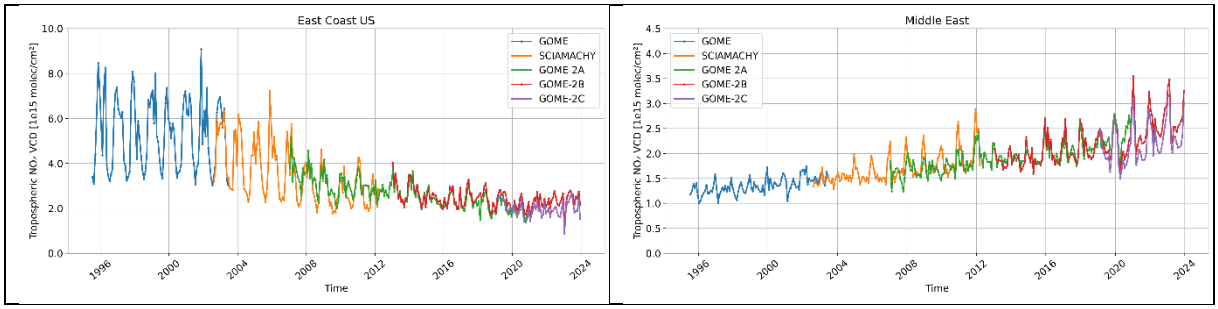

Figure 4-10: Time series of monthly average tropospheric NO_2 VCDs from all morning sensors (GOME/ERS-2, SCIAMACHY/ENVISAT, and GOME-2/MetOp-ABC) L3 NO_2 products, covering six source regions from 1995 to 2023.

Observation geometry

All the gridded variables in each grid cell are averaged using many ground pixels, with sometimes different observation conditions (solar and viewing angles, cloud and surface properties, *etc*). In the L3 data product, we provide average values of the angles, clouds and surface data to support the interpretation of the results. However, this information might be misleading at high latitudes, where orbits are overlapping. For more accurate computation, L2 data are more appropriate.

Global attributes

In addition to the netcdf conventions, several additional information is provided in the product global attributes, such as

- The list of L2 files used to calculate the L3 file.
- The L1 and L2 versions (SCD, AMF).
- The L3 and gridding software version
- The L2 data selection criteria

4.3. Formaldehyde (L3-HCHO)

4.3.1. Overview

The L3 gridding procedure is applied to the HCHO L2 data products described in section 3.2. The L2 versions used to produce the L3 CDR, and the corresponding L3 versions is detailed in the PUG [RD-12].

L3 products are available for each instrument separately. Two merged CDRs will also be provided separately for morning and afternoon observations.

- Morning sensors: GOME/ERS-2, SCIAMACHY/ENVISAT, GOME2/METOP-A, B, C
- Afternoon sensors: OMI/AURA, TROPOMI/S5P

Since the spatial resolution and signal-to-noise ratio of the sensors are different, and significantly better for the afternoon sensors, daily and monthly L3 files are provided for the afternoon sensors, while only monthly L3 files are provided for the morning sensors. The spatial resolution is chosen accordingly, see Table 4-3. The approach used to average the data in each grid cell is detailed in 4.3.2.

Table 4-2: Spatial resolution for morning and afternoon L3 products, at daily and monthly time resolution.

Spatial resolution/Grid size	Daily L3	Monthly L3
Morning CDR	-	From 0.25°x0.25° to 1°x1°
Afternoon CDR	0.25°x0.25°	0.125°x0.125°

The L3 product consists of HCHO tropospheric columns and associated random and systematic uncertainties, detailed intermediate results, and input data (see 4.3.3).

4.3.2. Data gridding approach

The core of the HCHO L3 gridding algorithm is based on the HARP atmospheric toolbox (https://atmospherictoolbox.org/harp/) and its spatial binning functionalities. We further develop on HARP to facilitate the gridding of daily and monthly data products from the different L2 products, and to include specific information and statistical estimates.

Data filtering

L2 pixels are filtered using the L2 qa_values recommended threshold of 0.5.

Spatial binning /gridding

Spatial binning grids the L2 data to a rectilinear latitude/longitude grid, using an area weighted average (see https://stcorp.github.io/harp/doc/html/algorithms/regridding.html). Per day/month, the selected L2 pixels are given a weight proportional to the fractional overlap of the given pixels with the grid cell, see Figure 4-8 for a schematic representation.

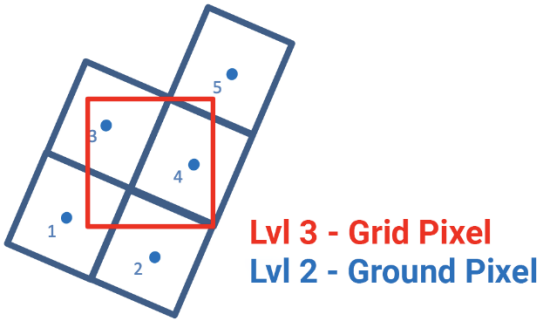

Figure 4-11: Schematic representation of L2 pixels (blue) gridded into a pre-defined grid cell (red).

The weight $w(i,j,k)$ determines the contribution of the source pixel *i* to the target grid cell *(j,k)*. With the calculated weights each variable is then regridded using:

$$y_t(j,k) = \frac{\sum_i w(i,j,k) y_s(i)}{\sum_i w(i,j,k)} \quad \text{Eq. 4-4}$$

The effective number of overlapping L2 pixels per grid cell for a given day/month is stored in a *count* variable.

4.3.3. Datasets

The complete list of parameters included in the L3 files is provided in the PUG [RD-12]. We describe below the key variables and provide more details about specific information and statistical estimates calculated on top of Harp functionalities.

Key gridded variables

From the L2 products, the key gridded variables are the HCHO tropospheric columns, with and without cloud correction ($\boldsymbol{N_v}$ and $\boldsymbol{N_{v,\ clear}}$). Additionally, following the user requirements [RD-9], several detailed intermediate results (slant columns, background-corrected slant columns, (clear) air mass factors, (clear) averaging kernels, etc.) are provided in the L3 products, as well as input data (surface albedo, cloud properties, vertical a priori profiles, etc…), observation geometry. See Figure 4-9 for an illustration of some provided variables. Furthermore, random and systematic uncertainties are provided using propagation of uncertainties, as well as statistical estimates (standard deviations in each grid cell). See E3UB document [RD-11] for more details.

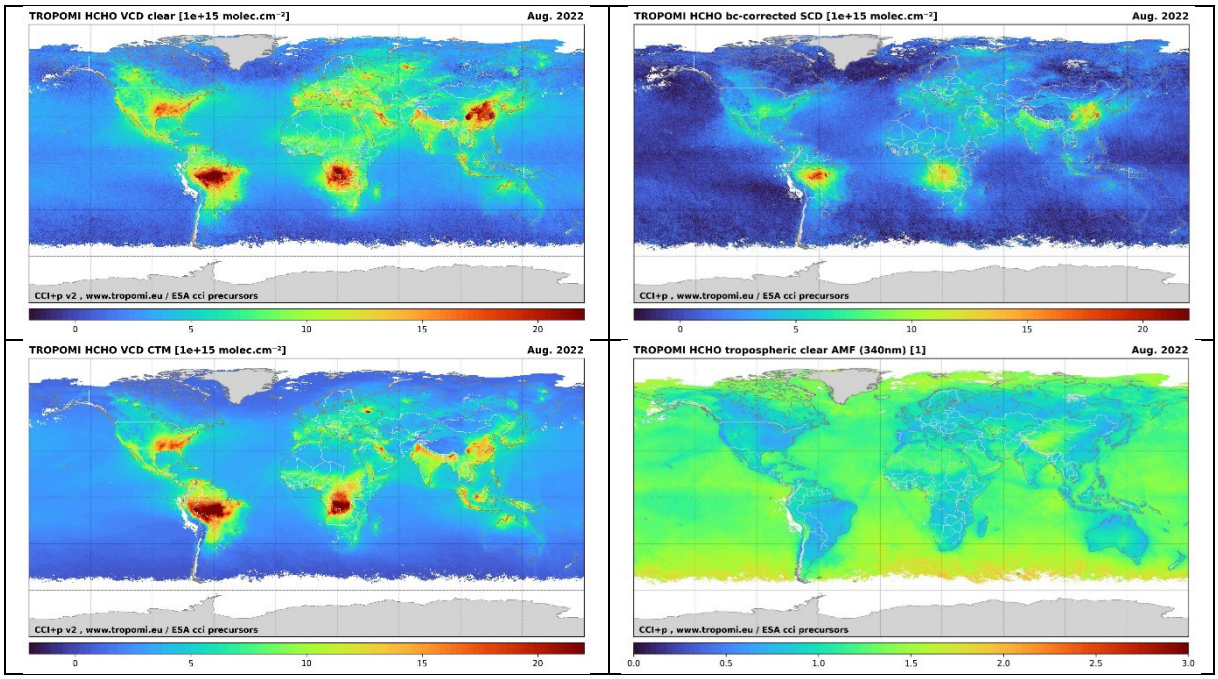

Figure 4-12: TROPOMI L3 gridded variables for August 2022: (a) HCHO clear VCD, (b) bc-corrected SCD, (c) a priori integrated HCHO column, (d) clear AMF.

Vertical dimension

Gridded averaging kernels and a priori vertical profiles are provided for each grid cell. Averaging kernels are provided with and without a cloud correction ($\boldsymbol{AK}$ and $\boldsymbol{AK_{clear}}$) and correspond respectively to tropospheric air mass factors with and without cloud correction ($\boldsymbol{M}$ and $\boldsymbol{M_{clear}}$).

Although the average of those quantities with a vertical dimension is not strictly correct, they can be used to re-calculate the provided L3 AMF with a good approximation (see Figure 4-10). To apply eq. 3.7, the altitude dependent air mass factors can be directly obtained from the AK and tropospheric air mass factor (eq. 3.9). The profiles need to be converted in partial columns. Surface pressure and model sigma values can be used to obtain the vertical layers in each grid cell. The user is invited to perform this test before going one step further by using alternative vertical profiles (an example of python script is provided in the PUG).

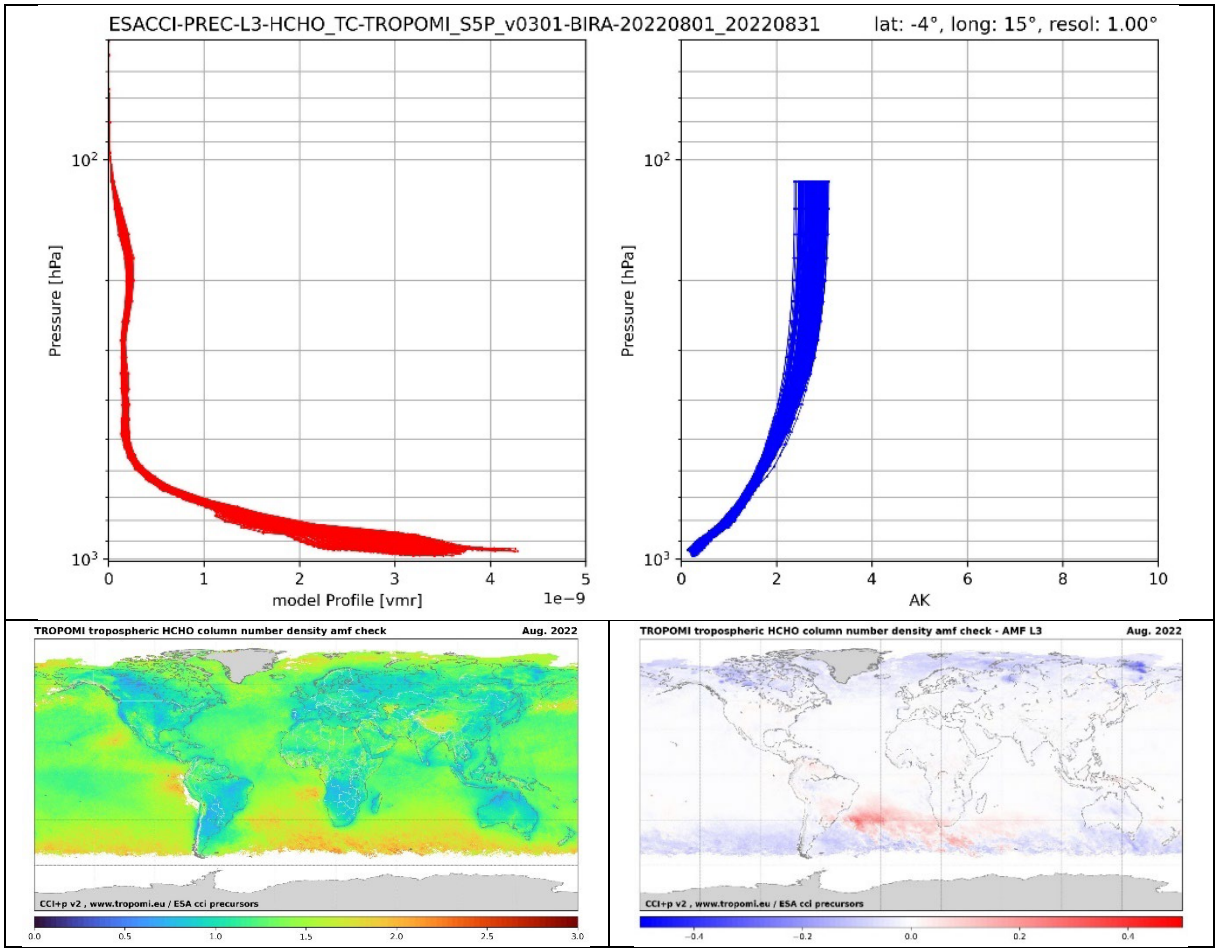

Figure 4-13: (a) L3 monthly gridded a priori profiles and averaging kernel (Aug. 2022) over RC Congo, (b) re-calculated AMF using only the L3 variables (AK, Profiles, surface pressure), (c) differences compared to the L3 gridded AMF.

Effective date and effective fractional day

For monthly averages, the day of the month is also gridded to provide an effective date. This gives an indication of the time coverage of the provided monthly means (but not on the spread of the dates). The effective fractional day of each observation is also added in the grids, in local solar time. This gives an indication of the averaged overpass time of the provided means.

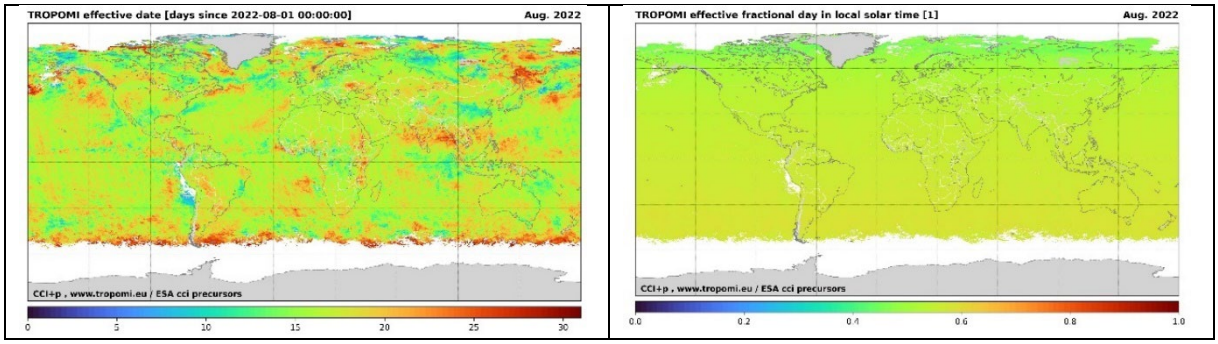

Figure 4-14: Effective date (day of the month) and fractional day gridded in August 2022 for TROPOMI.

Observation geometry

All the gridded variables in each grid cell are averaged using many ground pixels, with sometimes different observation conditions (solar and viewing angles, cloud and surface properties, *etc.*). We provide this information in the L3 data product to support the interpretation of the results. For more accurate computation, L2 data are more appropriate.

Global attributes

In addition to the netcdf conventions, several additional information is provided in the product global attributes, such as

- The list of L2 files used to calculate the L3 file.
- The L1 and L2 versions (SCD, AMF and BC).
- The L3 and gridding software version
- The L2 data selection criteria

4.4. Sulfur dioxide (L3-SO_2)

4.4.1. Overview

The L3 gridding procedure is applied to the SO2 L2 data products described in section 3.2. The L2 versions used to produce the L3 CDR, and the corresponding L3 versions is detailed in the PUG [RD-12].

L3 products are available for each instrument separately. One merged CDR will also be provided combining the GOME/ERS-2, SCIAMACHY/ENVISAT, OMI/AURA and TROPOMI/S5P sensors.

The L3 products are provided for two averaging time periods: daily and monthly averages. The spatial resolution is of 0.25°x0.25° for daily files and of 0.125°x0.125° for the monthly files. The approach used to average the data in each grid cell is the same as for HCHO and is detailed in Section 4.3.2.

The L3 product consists of SO_2 tropospheric columns and associated random and systematic uncertainties, detailed intermediate results, and input data (see 4.3.3).

4.4.2. Data gridding approach

See section 4.3.2 for a description of the gridding method.

4.4.3. Datasets

The list of parameters included in the L3 files is provided in the PUG (see [RD-12]). We illustrate below some key variables and provide more details about specific information and statistical estimates calculated on top of Harp functionalities.

Key gridded variables

From the L2 products, the key gridded variables are the SO_2 tropospheric columns, with and without cloud correction. Additionally, following the user requirements (URD, D1.1, [RD-9]**Error! Reference source not found.**), several detailed intermediate results (slant columns, (clear and cloud-corrected) air mass factors, averaging kernels, etc.) are provided in the L3 products, as well as input data (surface albedo, cloud properties, vertical a priori profiles, etc…), observation geometry. See Figure 4-12 for an illustration of some provided variables. Furthermore, random and systematic uncertainties are provided using propagation of uncertainties, as well as statistical estimates (standard deviations in each grid cell). See section 3.3 for more details. Note that all variables in the L3 data file are based on a data quality filtering using qa_value > 0.5. One exception is for total_SO2_column_number_density_box. This variable gathers the SO_2 vertical columns for box profiles at 1, 7, 15 km and is mostly useful to study volcanic plumes. To avoid masking useful data, the vertical columns for box profiles are filtered only for large SZA (>70°).

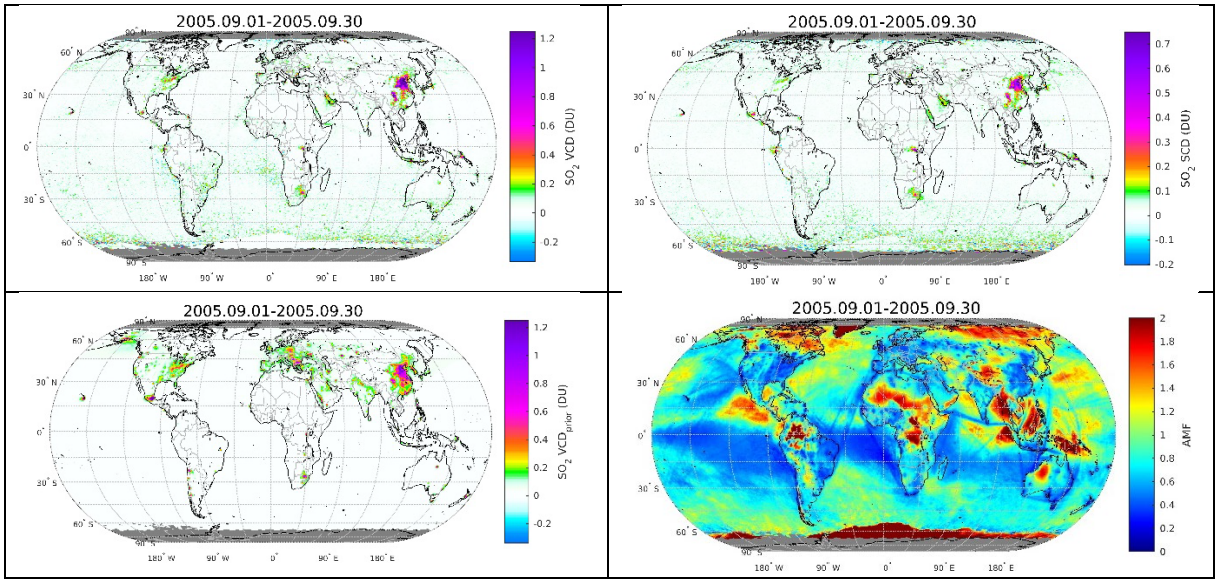

Figure 4-15: OMI L3 gridded variables for September 2005: (a) SO_2 VCD, (b) SO_2 SCD, (c) a priori integrated SO_2 column, (d) total AMF.

Effective date and effective fractional day

For monthly averages, the day of the month is also gridded to provide an effective date. This gives an indication of the time coverage of the provided monthly means (but not on the spread of the dates). The effective fractional day of each observation is also added in the grids, in local solar time. This gives an indication of the averaged overpass time of the provided means.

Observation geometry

All the gridded variables in each grid cell are averaged using many ground pixels, with sometimes different observation conditions (solar and viewing angles, cloud and surface properties, *etc.*). In the L3 data product, we provide average values of the angles, clouds and surface data to support the interpretation of the results. However, this information might be misleading at high latitudes, where orbits are overlapping. For more accurate computation, L2 data are more appropriate.

Global attributes

In addition to the netcdf conventions, several additional information is provided in the product global attributes, such as

- The list of L2 files used to calculate the L3 file.
- The L1 and L2 versions (SCD, AMF).
- The L3 and gridding software version
- The L2 data selection criteria

4.5. Glyoxal (L3-CHOCHO)

4.5.1. Overview

We generate separate level 3 gridded data products for each instrument, based on the level 2 products described in section [RD-12]. Additionally, we create a morning CDR from the merged observations of the GOME2 instruments on METOP-A, B and C platforms, and an afternoon CDR from merged OMI/AURA and TROPOMI/S5P observations.

Compared to the GOME2 sensors, OMI and TROPOMI have a significantly better signal-to-noise ratio and a higher spatial resolution. Therefore, we provide daily grids as well as high-resolution monthly grids for these afternoon sensors, whereas we only calculate monthly grids for the morning sensors.

Table 4-3: Spatial resolution for morning and afternoon L3 products, at daily and monthly time resolution.

Sensor	Daily L3 resolution	Monthly L3 resolution
GOME2/METOP-A, B, C	-	0.25° x 0.25°
OMI/AURA, TROPOMI/S5P	0.25° x 0.25°	0.125° x 0.125°

4.5.2. Data gridding approach

Glyoxal L3 data for a given grid cell is obtained by averaging the corresponding values from all overlapping L2 pixels with QA value equal to or above 0.5, where the contribution of each level 2 pixel is weighted by the overlap area with the target grid cell. The L3-CHOCHO gridding algorithm is based on the spatial binning functionality provided by the HARP toolkit, using the same approach as the HCHO gridding algorithm described in section 4.3.2. We refer to sections 4.3.2 and 4.3.3 for a detailed description of the spatial binning algorithm and the calculation of uncertainty estimates.

4.5.3. Datasets

We refer to the PUG [RD-12] for a full overview of the variables contained in each L3 data set. We describe the key variables below.

Key gridded variables

The key variable in the glyoxal L3 data is the tropospheric glyoxal vertical column density. Intermediate results and auxiliary input data which may help in the interpretation or analysis of results are also gridded and included the L3 files, such as slant column densities, the background correction, air mass factors and averaging kernels, a priori profiles and surface albedo. As observations with a cloud fraction above 20% are excluded by the QA value filtering, we only provide air mass factors and averaging kernels for cloud-free scenes. We refer the user to section 4.3.3 for a discussion on the use as well as the limitations of these gridded averaging kernels and profiles. A few examples of gridded variables are shown in Figure 4-13.

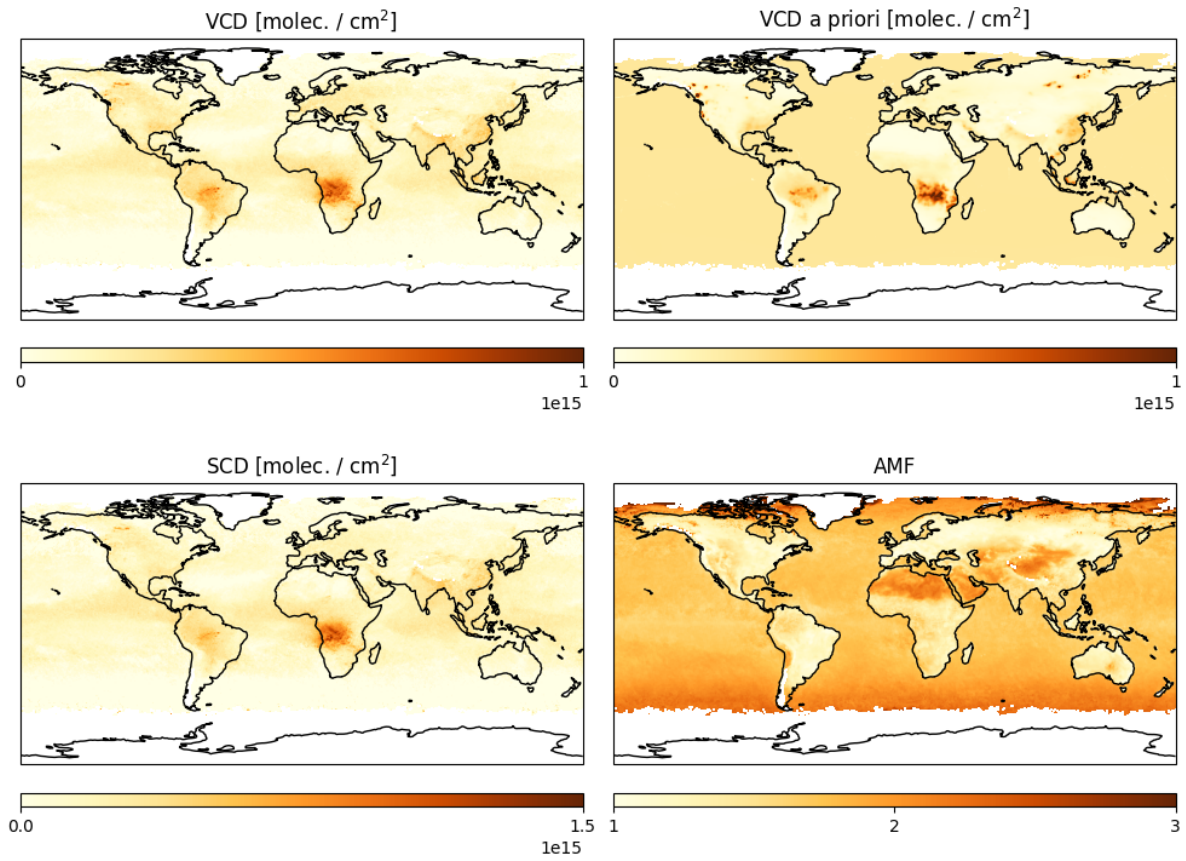

Figure 4-16: August 2023 CHOCHO-L3 VCD, a priori VCD, SCD and AMF

4.6. Carbon monoxide (L3-CO)

4.6.1. Overview

We generate a monthly Climate Data Record (CDR) Level 3 Carbon Monoxide (CO) product from IASI and MOPITT monthly L3 datasets. It consists in monthly grids for daytime and nighttime measurements. The objective is to produce a harmonized dataset that combines the strengths of both instruments while minimizing uncertainties.

The merged product incorporates data from a IASI non-public intermediate multiplatform dataset as well as MOPITT V9T data, processed with a weighted averaging approach. During cycle 1, we generated the IASI non-public intermediate multiplatform dataset averaging cloud free data from Metop-A, Metop-B, and Metop-C. This intermediate IASI dataset has been validated by BIRA. The input data are described in Section 3.5.

The merged dataset spans from January 2008 to November 2023. We stopped in November 2023 as MOPITT V9T data are delivered in beta version from December 2023. The merged dataset provided in netcdf files includes monthly grids for CO total column, corresponding uncertainty grids, surface altitude grids, flag grids indicating the data sources used as well as metadata.

4.6.2. Methodology

For the first time, we generated a dataset from IASI and MOPITT monthly L3 data. We used the official MOPITT data available online from the NASA Earthdata portal. As monthly grids are 1°x1° grids, we choose this grid resolution as it is perfectly suited for carbon monoxide grids. Therefore, our IASI intermediate product, as well as the CDR merged product are at 1° x 1° resolution, with latitude ranging from −89.5° to +89.5° and longitude from −179.5° to +179.5°. Monthly grids are created separately for daytime and nighttime observations.

The input datasets (described in Section 3.5) are:

- IASI multiplatform (Metop-A, B and C) CO total column and uncertainty monthly grids calculated from L2 total column CO Climate Data Record processed at EUMETSAT.
- MOPITT V9T monthly grids for CO total column, prior CO total column and total uncertainty estimates.

The merging process combines the CO total column data from both instruments using weighted averaging. The steps are as follows:

1. *Calculation of MOPITT total column/prior ratio and weight grids*

To account for the strength of CO signature in the MOPITT measurement, the ratio total column/prior is first calculated. This ratio indicates how much the retrieved MOPITT value deviates from its prior estimate. The ratio is compared to predefined thresholds (e.g., 0.9 and 1.1). If the retrieved total column is 10% larger or smaller than the prior, the weight assigned to MOPITT data is increased from 0.5 to a 0.65. Otherwise, MOPITT is assigned a neutral weight of 0.5. The IASI weight is then determined as the difference between 1 and the MOPITT weight. Total weight sums to 1. The ratio and weight grids are calculated separately for daytime and nighttime observations.

2. *Weighted averaging of CO total columns*

The merged CO total column for each grid point is calculated as the weighted average of IASI and MOPITT total columns, using the weights previously calculated:

$X_{merged} = w_{MOPITT} X_{MOPITT} + w_{IASI} X_{IASI}$

Where:

- X_{MOPITT} and X_{IASI} are the input grids.

- w_{MOPITT} and w_{IASI} are the weights associated with each grid, and $w_{MOPITT} + w_{IASI} = 1$.

3. Uncertainty *grids calculation corresponding to the merged CO product*

The uncertainty for the merged CO column is calculated using a weighted root-mean-square approach. The formula for the propagated uncertainty in the weighted mean is:

$$\sigma_{merged} = \sqrt{w_{MOPITT}^2 \, \sigma_{MOPITT}^2 + w_{IASI}^2 \, \sigma_{IASI}^2}$$

Where:

- σ_{merged} is the uncertainty associated with the weighted mean grid X_{merged}.

- σ_{MOPITT} is the uncertainty grid corresponding to the MOPITT CO total column grid.

- σ_{IASI} is the uncertainty grid corresponding to the IASI CO total column grid.

- w_{MOPITT} and w_{IASI} are the weights associated with each grid.

Handling missing data:

IASI and MOPITT monthly grids can include NaN cells. This is due to cloud filtering or quality filtering to generate the L3 from the L2 data. Or this can be due to the availability of the data, depending of the time of the year and the time of the day: see Figure 4-14 for one month of July where there is no data for the high latitude cells during daytime and for the low latitude cells during nighttime. Grid points with no data from either instrument are flagged and assigned a missing value (NaN). When only one instrument's data is available for a grid, the merged value defaults to the available instrument's value. The following rules are applied to handle missing data:

1. Both IASI and MOPITT are available (non-NaN): The weighted average of the two values is calculated.
2. Only IASI data is available: The merged value is set to the IASI value.
3. Only MOPITT data is available: The merged value is set to the MOPITT value.
4. Neither IASI nor MOPITT data is available: The grid point is assigned a missing value (NaN).

This approach ensures that the merged grid retains data where at least one instrument provides observations while prioritizing a weighted combination when both sources are

available. The benefit of this choice can be appreciated in Figure 4-17, where the merged plot provides a better spatial coverage than the two individual input data plots.

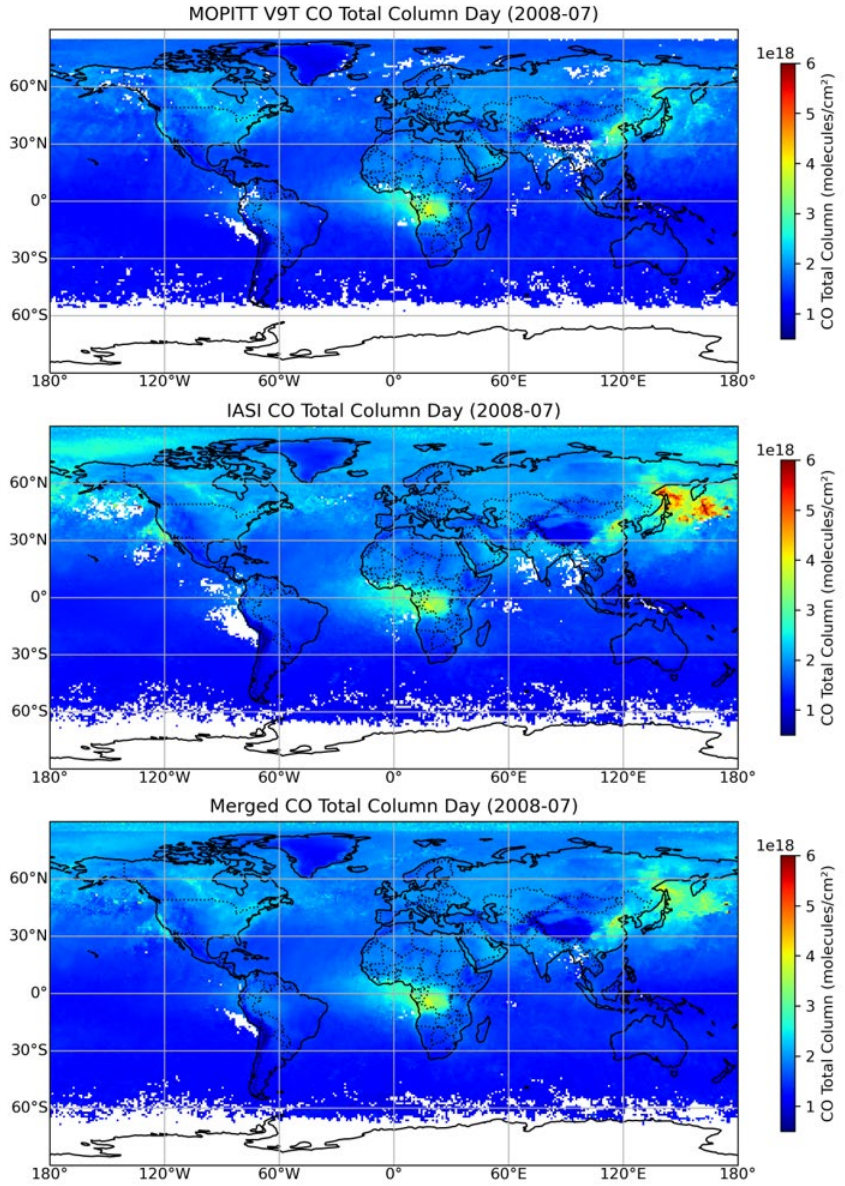

Figure 4-17: MOPITT, IASI and CCI+ MERGED CO grids for July 2008 (daytime). White areas are cell grids with no data.

We provide flag grids indicating the source(s) of the data. Each grid point can take the following values:

- 3: Both IASI and MOPITT data were used.
- 2: Only IASI data was used.
- 1: Only MOPITT data was used.
- 0: No data available.

4.6.3. Dataset

We refer to the PUG [RD-12] for a full overview of the variables contained in each monthly netcdf file. The key variables are 1° x 1° grids plotted in Figure 4-18: CO total column monthly averages, uncertainty corresponding to the CO total column, flag for data source identification and surface altitude. All these variables are given for daytime and nighttime.

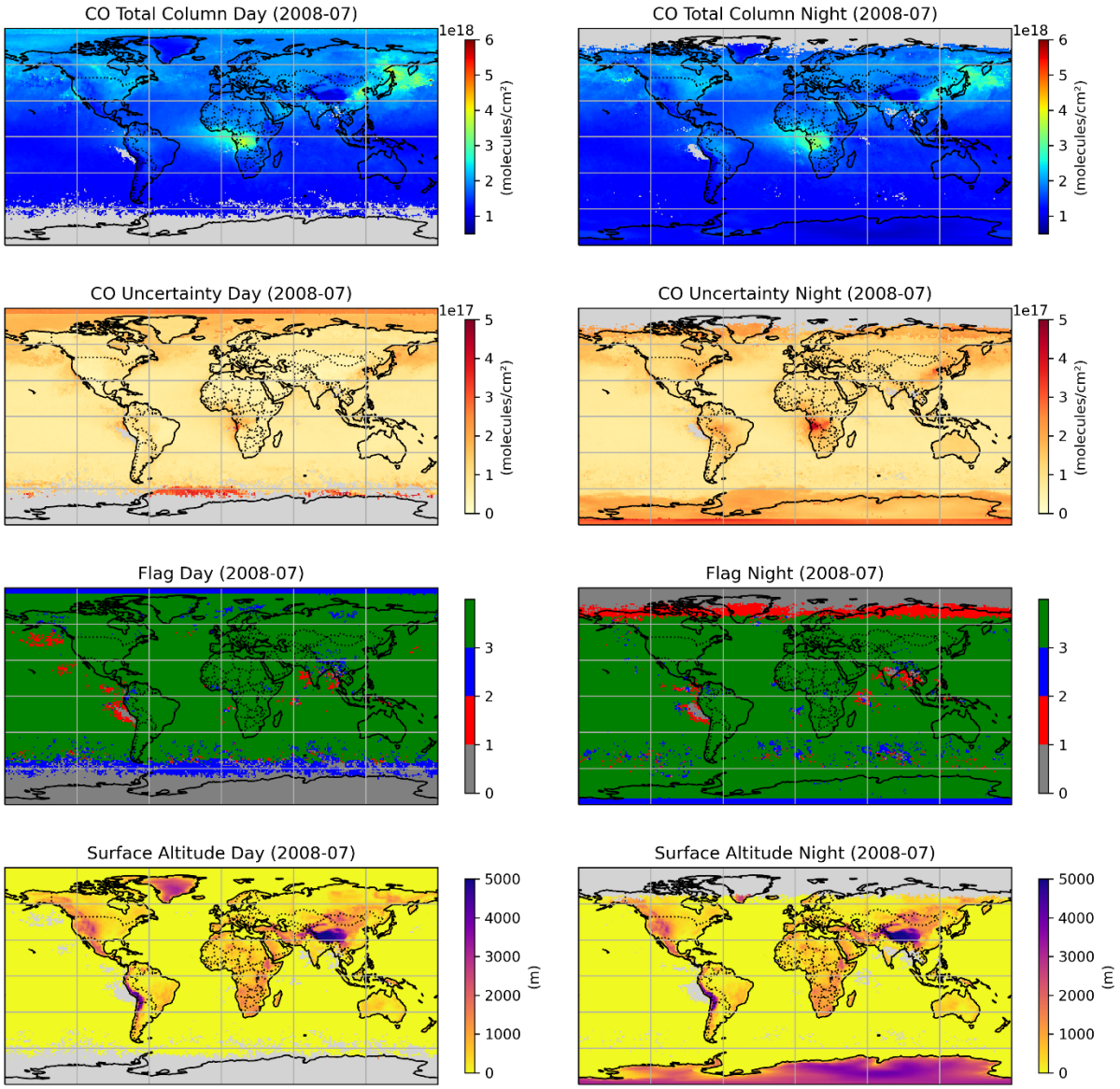

Figure 4-18: Key variables of CCI+ CO merged monthly L3 product from IASI and MOPITT. Example for July 2008. CO total column (line 1), associated uncertainty (line 2), data source flags (line 3), and surface altitude (line 4), for both daytime (left) and nighttime (right) observations. Flags identify sources: 3 = both IASI and MOPITT, 2 = IASI only, 1 = MOPITT only, 0 = no data.

4.6.4. L3 uncertainty estimate

For this section, we refer to the E3UB document. On global scale, mean uncertainty for daytime merged product is 1.1 10^{17} molecules/cm^2 with a standard deviation of 0.7 10^{17} molecules/cm^2. For nighttime, the mean uncertainty is slightly larger: 1.3 10^{17} molecules/cm^2 [std: 0.7 10^{17} molecules/cm^2]. CO uncertainty time series for the merged product, as well as for IASI and MOPITT V9T, for the [20°N-60°N] latitude band and for daytime, are shown in Figure 4-19.

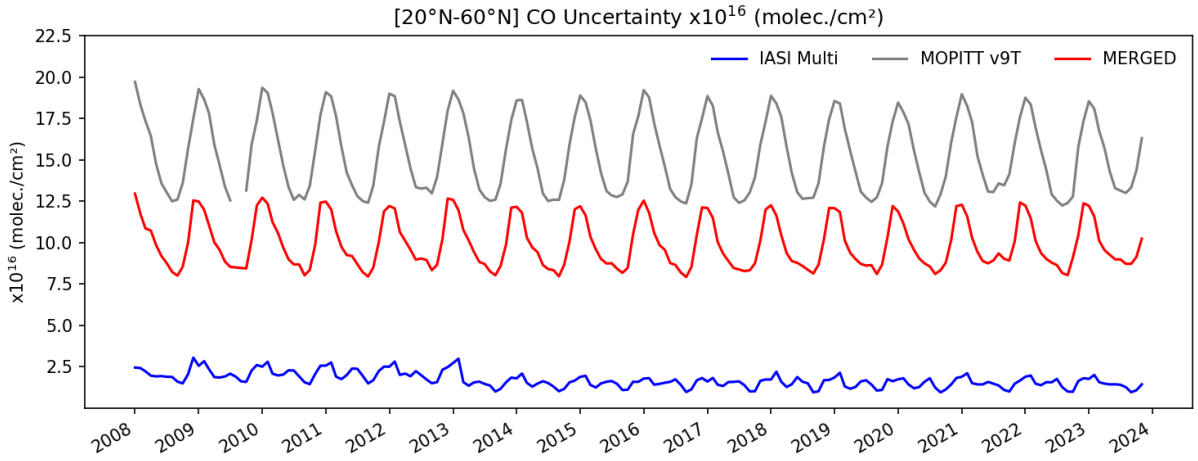

Figure 4-19: CO uncertainty time series for the [20°N-60°N] latitude band, for daytime measurements. The new merged CO CCI+ product is represented in red, IASI in blue and MOPITT in grey.

4.7. Ammonia (L3-NH_3)

4.7.1. Overview

The L3 gridding procedure is applied to the NH_3 L2 data products described in section 3.6. The L2 versions used to produce the L3 CDR, and the corresponding L3 versions is detailed in the PUG [RD-12].

Monthly L3 products are available for each instrument separately. These correspond to the entire timeseries of available L1C data. A merged CDRs for the period 2008–2024 is also available which is made up of data from Metop-A (2008–2013), Metop-B (2014–2019) and Metop-C (2020–2024). In each case, a separate L3 is available for the IASI morning overpass, for the evening overpass, and for both overpasses taken together. The spatial resolution is 0.2° × 0.2°. The approach used to average the data in each grid cell is detailed in the following section. The L3 product consists of NH_3 total columns, associated random and systematic uncertainties, and auxiliary data (see 4.6.3).

4.7.2. Data gridding

Data filtering

L2 observations are filtered using the recommended post-filter included in the L2 NH_3 data.

Spatial binning /gridding

Using a subgrid of 0.025° × 0.025°, the fractional overlap of the native IASI footprint on ground with the 0.2° × 0.2° L3 grid is calculated (see Figure 4-17). The code for this is publicly available at https://squares.ulb.be/NH3-IASI.html, see also Clarisse et al. (2019). The L3 averages for a single grid cell are calculated as

$$\bar{X} = \frac{\sum_{i=1}^{n} x_i w_i}{\sum_{i=1}^{n} w_i}$$

with x_i all the observations that intersect with the given grid cell, and w_i the associated fractional overlap. This formula is used for all L3 variables, except for the average random uncertainty, which is calculated as

$$\sigma_{r\bar{X}}^2 = \frac{\sum_{i=1}^{n} \sigma_{rx_i}^2 w_i^2}{\left(\sum_{i=1}^{n} w_i\right)^2}$$

Note that the systematic uncertainty is calculated as normal. Averaged random (σ_r) and systematic (σ_s) uncertainties are available for each grid cell. If a total uncertainty is desired, this can be obtained from the square root of the sum of squares of the different terms:

$$\sigma^2 = \sigma_r^2 + \sigma_s^2$$

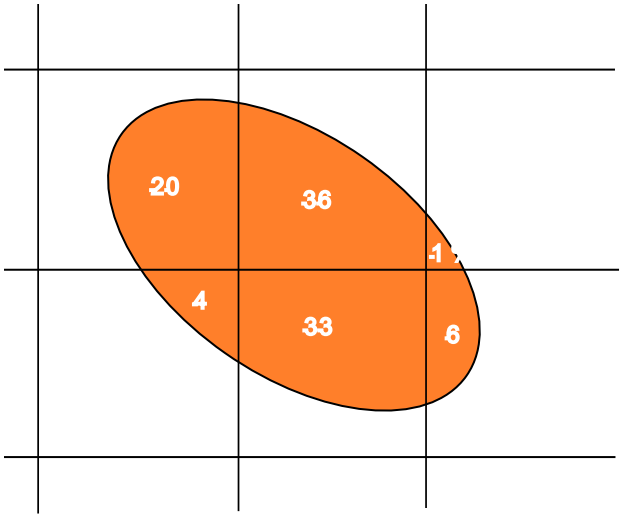

Figure 4-20: Illustration of the weight calculation of an IASI observation (orange ellipse), onto regular grid.

Effective date and effective fractional day

For monthly averages, the day of the month is also gridded to provide an effective date. This gives an indication of the time coverage of the provided monthly means. Note however, that this quantity does not provide an indication of spread (two observations on day 1 and 30 or two observations on day 15 and 16 have the same effective date). The effective fractional day of each observation is also provided, in local solar time. This gives an indication of the averaged overpass time of the provided means. It is calculated as:

$$\text{Effective fractional day} = (\text{UTChour} + \text{longitude}/15)/24$$

4.7.3. Example

Example distributions for six key variables are provided in Figure 4-18.

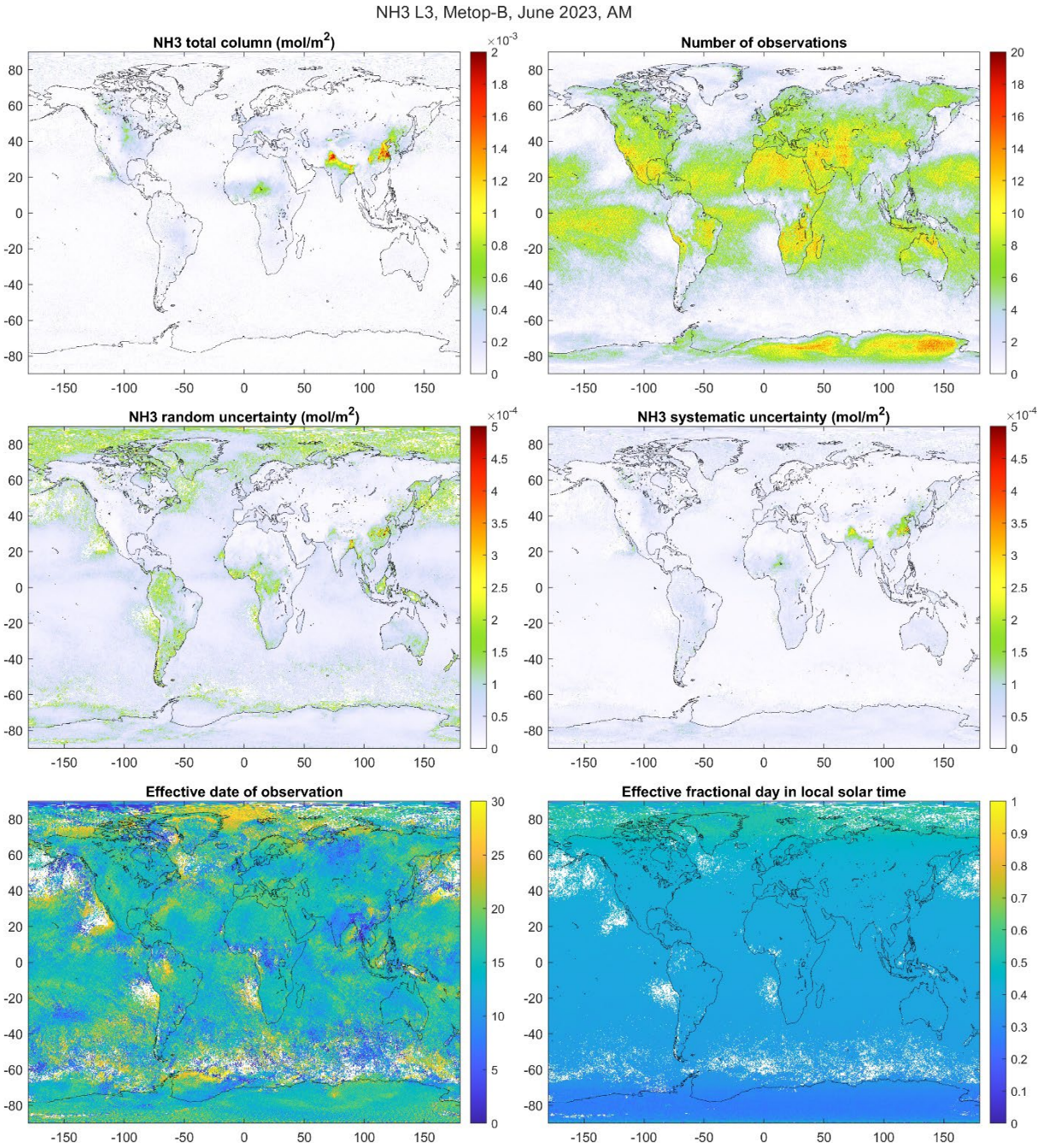

Figure 4-21: Illustration of six key variables in the NH_3 L3 datasets.

5. References

Alvarado, L. M. A., Richter, A., Vrekoussis, M., Wittrock, F., Hilboll, A., Schreier, S. F. and Burrows, J. P.: An improved glyoxal retrieval from OMI measurements, Atmos. Meas. Tech., 7(12), 4133–4150, doi:10.5194/amt-7-4133-2014, 2014.

August, T., Klaes, D., Schlüssel, P., Hultberg, T., Crapeau, M., Arriaga, A., O'Carroll, A., Coppens, D., Munro, R., & Calbet, X. (2012) IASI on Metop-A: Operational Level 2 retrievals after five years in orbit. Journal of Quantum Spectroscopy and Radiative Transfer 113, 1340–1371.

Barkley, M. P., González Abad, G., Kurosu, T. P., Spurr, R., Torbatian, S., and Lerot, C.: OMI air-quality monitoring over the Middle East, Atmos. Chem. Phys., 17, 4687–4709, https://doi.org/10.5194/acp-17-4687-2017, 2017

Beirle, S., Hörmann, C., Jöckel, P., Liu, S., Penning de Vries, M., Pozzer, A., Sihler, H., Valks, P., and Wagner, T.: The STRatospheric Estimation Algorithm from Mainz (STREAM): estimating stratospheric NO2 from nadir-viewing satellites by weighted convolution, Atmos. Meas. Tech., 9, 2753–2779, https://doi.org/10.5194/amt-9-2753-2016, 2016.

Beirle, S., Sihler, H., andWagner, T.: Linearisation of the effects of spectral shift and stretch in DOAS analysis, Atmos. Meas. Tech., 6, 661–675, https://doi.org/10.5194/amt-6-661-2013, 2013.

Boersma, K. F., Eskes, H. J., and Brinksma, E. J.: Error analysis for tropospheric NO2 retrieval from space, J. Geophys. Res., 109, D04311, doi: 10.1029/2003JD003962, 2004.

Boersma, K. F., Eskes, H. J., Dirksen, R. J., van der A, R. J., Veefkind, J. P., Stammes, P., Huijnen, V., Kleipool, Q. L., Sneep, M., Claas, J., Leitão, J., Richter, A., Zhou, Y., and Brunner, D.: An improved tropospheric NO2 column retrieval algorithm for the Ozone Monitoring Instrument, Atmos. Meas. Tech., 4, 1905–1928, https://doi.org/10.5194/amt-4-1905-2011, 2011.

Boersma, K. F., Eskes, H. J., Richter, A., De Smedt, I., Lorente, A., Beirle, S., van Geffen, J. H. G. M., Zara, M., Peters, E., Van Roozendael, M., Wagner, T., Maasakkers, J. D., van der A, R. J., Nightingale, J., De Rudder, A., Irie, H., Pinardi, G., Lambert, J.-C., and Compernolle, S. C.: Improving algorithms and uncertainty estimates for satellite NO2 retrievals: results from the quality assurance for the essential climate variables (QA4ECV) project, Atmos. Meas. Tech., 11, 6651–6678, https://doi.org/10.5194/amt-11-6651-2018, 2018.

Bogumil, K., Orphal, J., Homann, T., Voigt, S., Spietz, P., Fleischmann, O., Vogel, A., Hartmann, M., Bovensmann, H., Frerick, J., and Burrows, J.P.: Measurements of molecular absorption spectra with the SCIAMACHY Pre-Flight Model: instrument characterization and reference data for atmospheric remote-sensing in the 230-2380 nm region, Journal of Photochemistry and Photobiology A, 157, 167-184, 2003.

Camy-Peyret, C., & Eyre, J. (1998). The IASI Science Plan. Technical report, A Report From The IASI Sounding Science Working Group.

Chan Miller, C., Gonzalez Abad, G., Wang, H., Liu, X., Kurosu, T., Jacob, D. J. and Chance, K.: Glyoxal retrieval from the Ozone Monitoring Instrument, Atmos. Meas. Tech., 7(11), 3891–3907, doi:10.5194/amt-7-3891-2014, 2014.

Clarisse, L., Clerbaux, C., Franco, B., Hadji-Lazaro, J., Whitburn, S., Kopp, A. K., Hurtmans, D., and Coheur, P.-F.: A Decadal Data Set of Global Atmospheric Dust Retrieved From IASI Satellite Measurements, J. Geophys. Res. Atmos., 124, 1618–1647, https://doi.org/10.1029/2018jd029701, 2019.

Clarisse, L., Van Damme, M., Clerbaux, C., and Coheur, P.-F.: Tracking down global NH_3 point sources with wind-adjusted superresolution, Atmos. Meas. Tech., 12, 5457–5473, https://doi.org/10.5194/amt-12-5457-2019, 2019.

Clarisse, L., Coheur, P. F., Prata, F., Hadji-Lazaro, J., Hurtmans, D., & Clerbaux, C. (2013). A unified approach to infrared aerosol remote sensing and type specification. Atmospheric Chemistry and Physics, 13(4), 2195-2221.

Clarisse, L., Franco, B., Van Damme, M., Di Gioacchino, T., Hadji-Lazaro, J., Whitburn, S., Noppen, L., Hurtmans, D., Clerbaux, C., and Coheur, P.: The IASI NH_3 version 4 product: averaging kernels and improved consistency, Atmos. Meas. Tech. Discuss. [preprint], https://doi.org/10.5194/amt-2023-48, in review, 2023.

Clerbaux, C., Boynard, A., Clarisse, L., George, M., Hadji-Lazaro, J., Herbin, H., Hurtmans, D., Pommier, M., Razavi, A., Turquety, S., Wespes, C., & Coheur, P.-F.: Monitoring of atmospheric composition using the thermal infrared IASI/MetOp sounder. Atmospheric Chemistry and Physics, 9, 6041–6054, 2009.

Coheur, P.-F., Barret, B., Turquety, S., Hurtmans, D., Hadji-Lazaro, J., and Clerbaux, C.: Retrieval and characterization of ozone vertical profi les from a thermal infrared nadir sounder, J. Geophys. Res., 110, D24 303, https://doi.org/10.1029/2005JD005845, 2005.

Compernolle, S., Verhoelst, T., Pinardi, G., Granville, J., Hubert, D., Keppens, A., ... & Lambert, J. C. (2020). Validation of Aura-OMI QA4ECV NO2 climate data records with ground-based DOAS networks: the role of measurement and comparison uncertainties. Atmospheric Chemistry and Physics, 20(13), 8017-8045.

Dammers, E., Palm, M., Damme, M. V., Vigouroux, C., Smale, D., Conway, S., Toon, G. C., Jones, N., Nussbaumer, E., Warneke, T., Petri, C., Clarisse, L., Clerbaux, C., Hermans, C., Lutsch, E., Strong, K., Hannigan, J. W., Nakajima, H., Morino, I., Herrera, B., Stremme, W., Grutter, M., Schaap, M., Kruit, R. J. W., Notholt, J., Coheur, P.-F., and Erisman, J. W.: An evaluation of IASI-NH 3 with ground-based Fourier transform infrared spectroscopy measurements, Atmos. Chem. Phys., 16, 10 351–10 368, https://doi.org/10.5194/acp-16-10351-2016, 2016

Danckaert, T., Fayt, C., van Roozendael, M., De Smedt, I., Letocard, V., Merlaud, A. and Pinardi, G.: QDOAS software user manual. [online] Available from: http://uv-vis.aeronomie.be/software/QDOAS/QDOAS_manual.pdf, 2017

De Smedt, I., Pinardi, G., Vigouroux, C., Compernolle, S., Bais, A., Benavent, N., Boersma, F., Chan, K.-L., Donner, S., Eichmann, K.-U., Hedelt, P., Hendrick, F., Irie, H., Kumar, V., Lambert, J.-C., Langerock, B., Lerot, C., Liu, C., Loyola, D., Piters, A., Richter, A., Rivera Cárdenas, C.,

Romahn, F., Ryan, R. G., Sinha, V., Theys, N., Vlietinck, J., Wagner, T., Wang, T., Yu, H., and Van Roozendael, M.: Comparative assessment of TROPOMI and OMI formaldehyde observations and validation against MAX-DOAS network column measurements, Atmos. Chem. Phys., 21, 12561–12593, https://doi.org/10.5194/acp-21-12561-2021, 2021.

De Smedt, I., Theys, N., van Gent, J., Danckaert, T., Yu, H., and Van Roozendael, M.: S5P/TROPOMI HCHO ATBD, S5P-BIRA-L2-400F-ATBD, v2.4.1, 2022-06-22, Level-2 Algorithm Developments for Sentinel-5 Precursor.

De Smedt, I., Theys, N., Yu, H., Danckaert, T., Lerot, C., Compernolle, S., Van Roozendael, M., Richter, A., Hilboll, A., Peters, E., Pedergnana, M., Loyola, D., Beirle, S., Wagner, T., Eskes, H., van Geffen, J., Boersma, K. F., and Veefkind, P.: Algorithm theoretical baseline for formaldehyde retrievals from S5P TROPOMI and from the QA4ECV project, Atmos. Meas. Tech., 11, 2395–2426, https://doi.org/10.5194/amt-11-2395-2018, 2018.

De Smedt, I., Yu, H., Richter, A., Beirle, S., Eskes, H., Boersma, K. F., Van Roozendael, M., Van Geffen, J., Lorente, A., and Peters, E.: QA4ECV HCHO tropospheric column data from OMI (Version 1.1) [Data set], Royal Belgian Institute for Space Aeronomy, https://doi.org/10.18758/71021031, 2017.

Dirksen, R. J., Boersma, K. F., Eskes, H. J., Ionov, D. V., Bucsela, E. J., Levelt, P. F., and Kelder, H. M.: Evaluation of stratospheric NO2 retrieved from the Ozone Monitoring Instrument: Intercomparison, diurnal cycle, and trending, J. Geophys. Res., 116, D08305, doi:10.1029/2010JD014943, 2011.

Eaton, M.: Multivariate Statistics: A Vector Space Approach, Institute of Mathematical Statistics, Beachwood, Ohio, USA, 2007.

Eskes, H. J. and K. F. Boersma, Averaging kernels for DOAS total-column satellite retrievals, Atmos. Chem. Phys., 3, 1285-1291, 2003.

Franco, B., Clarisse, L., Stavrakou, T., Müller, J.-F., Van Damme, M., Whitburn, S., Hadji-Lazaro, J., Hurtmans, D., Taraborrelli, D., Clerbaux, C., and Coheur, P.-F.: A General Framework for Global Retrievals of Trace Gases From IASI: Application to Methanol, Formic Acid, and PAN, J. Geophys. Res. Atmos., 123, 13,963–13,984, https://doi.org/10.1029/2018jd029633, 2018.

Georgoulias, A. K., van der A, R. J., Stammes, P., Boersma, K. F., and Eskes, H. J.: Trends and trend reversal detection in 2 decades of tropospheric NO2 satellite observations, Atmos. Chem. Phys., 19, 6269–6294, https://doi.org/10.5194/acp-19-6269-2019, 2019.

Guo, X., Clarisse, L., Wang, R., Van Damme, M., Whitburn, S., Coheur, P.-F., Clerbaux, C., Franco, B., Pan, D., Golston, L. M., Wendt, L., Sun, K., Tao, L., Miller, D., Mikoviny, T., Müller, M., Wisthaler, A., Tevlin, A. G., Murphy, J. G., Nowak, J. B., Roscioli, J. R., Volkamer, R., Kille, N., Neuman, J. A., Eilerman, S. J., Crawford, J. H., Yacovitch, T. I., Barrick, J. D., Scarino, A. J., and Zondlo, M. A.: Validation of IASI satellite ammonia observations at the pixel scale using in-situ vertical profi les, J. Geophys. Res. Atmos., https://doi.org/10.1029/2020jd033475, 2021.

Hermans, C., Vandaele, A.C., and Fally, S.: Fourier transform measurements of SO_2 absorption cross sections: I. Temperature dependence in the 24 000–29 000 cm-1 (345–420 nm) region, J. Quant Spectrosc. Radiat. Transfer, 110, 756–765, doi: 10.1016/j.jqsrt.2009.10.031, 2009.

Hersbach, H., Bell, B., Berrisford, P., Hirahara, S., Horányi, A., Muñoz-Sabater, J., Nicolas, J., Peubey, C., Radu, R., Schepers, D., Simmons, A., Soci, C., Abdalla, S., Abellan, X., Balsamo, G., Bechtold, P., Biavati, G., Bidlot, J., Bonavita, M., Chiara, G., Dahlgren, P., Dee, D., Diamantakis, M., Dragani, R., Flemming, J., Forbes, R., Fuentes, M., Geer, A., Haimberger, L., Healy, S., Hogan, R. J., Hólm, E., 640 Janisková, M., Keeley, S., Laloyaux, P., Lopez, P., Lupu, C., Radnoti, G., Rosnay, P., Rozum, I., Vamborg, F., Villaume, S., and Thépaut, J.-N.: The ERA5 global reanalysis, Q. J. R. Meteorolog. Soc., 146, 1999–2049, https://doi.org/10.1002/qj.3803, 2020.

Hilton, F., August, T., Barnet, C., Bouchard, A., Camy-Peyret, C., Clarisse, L., Clerbaux, C., Coheur, P.-F., Collard, A., Crevoisier, C., Dufour, G., Edwards, D., Faijan, F., Fourrié, N., Gambacorta, A., Gauguin, S., Guidard, V., Hurtmans, D., Illingworth, S., Jacquinet-Husson, N., Kerzenmacher, T., Klaes, D., Lavanant, L., Masiello, G., Matricardi, M., McNally, T., Newman, S., Pavelin, E., Péquignot, E., Phulpin, T., Remedios, J., Schlüssel, P., Serio, C., Strow, L., Taylor, J., Tobin, D., Uspensky, A., & Zhou, D. (2012). Hyperspectral Earth Observation with IASI. Bulletin of the American Meteorological Society, 93(3), 347-370.

Inness, A., Ades, M., Agustí-Panareda, A., Barré, J., Benedictow, A., Blechschmidt, A.-M., Dominguez, J. J., Engelen, R., Eskes, H., Flemming, J., Huijnen, V., Jones, L., Kipling, Z., Massart, S., Parrington, M., Peuch, V.-H., Razinger, M., Remy, S., Schulz, M., and Suttie, M.: The CAMS reanalysis of atmospheric composition, Atmos. Chem. Phys., 19, 3515–3556, https://doi.org/10.5194/acp-19-3515-2019, 2019.

Kleipool, Q. L., Dobber, M. R., de Haan, J. F. and Levelt, P. F.: Earth surface reflectance climatology from 3 years of OMI data, J. Geophys. Res., 113(D18), D18308, doi:10.1029/2008JD010290, 2008.

Kleipool, Q., Rozemeijer, N., van Hoek, M., Leloux, J., Loots, E., Ludewig, A., van der Plas, E., Adrichem, D., Harel, R., Spronk, S., ter Linden, M., Jaross, G., Haffner, D., Veefkind, P., and Levelt, P. F.: Ozone Monitoring Instrument (OMI) collection 4: establishing a 17-year-long series of detrended level-1b data, Atmos. Meas. Tech., 15, 3527–3553, https://doi.org/10.5194/amt-15-3527-2022, 2022.

Langerock, Validation report of reprocessed IASI L2 CO CDR for Metop-A and B, https://acsaf.org/docs/vr/Validation_Report_IASI_CO_CDR_Nov_2023.pdf, 2023.

Lerot , C., Stavrakou, T., Van Roozendael, M., Alvarado, L.M.A. and Richter, A.: GLYoxal Retrievals from TROPOMI (GLYRETRO) – ATBD, 2021, available at https://data-portal.s5p-pal.com/product-docs/chocho/CHOCHO_ATBD_S5P+I_BIRA_v3.1.pdf

Lerot, C., Stavrakou, T., De Smedt, I., Müller, J. F., Van Roozendael, M., M̈uller, J. F. and Van Roozendael, M.: Glyoxal vertical columns from GOME-2 backscattered light measurements and comparisons with a global model, Atmos. Chem. Phys., 10(24), 12059–12072, doi:10.5194/acp-10-12059-2010, 2010.

Levy, R. C., Remer, L. A., Mattoo, S., Vermote, E. F., & Kaufman, Y. J. : Second-generation operational algorithm: Retrieval of aerosol properties over land from inversion of Moderate Resolution Imaging Spectroradiometer spectral reflectance. Journal of Geophysical Research: Atmospheres, 112(D13), 2007.

Liu, S., Valks, P., Pinardi, G., De Smedt, I., Yu, H., Beirle, S., and Richter, A.: An improved total and tropospheric NO2 column retrieval for GOME-2, Atmos. Meas. Tech., 12, 1029–1057, https://doi.org/10.5194/amt-12-1029-2019, 2019.

Liu, S., Valks, P., Pinardi, G., Xu, J., Argyrouli, A., Lutz, R., Tilstra, L. G., Huijnen, V., Hendrick, F., and Van Roozendael, M.: An improved air mass factor calculation for nitrogen dioxide measurements from the Global Ozone Monitoring Experiment-2 (GOME-2), Atmos. Meas. Tech., 13, 755–787, https://doi.org/10.5194/amt-13-755-2020, 2020.

Lorente, A., Folkert Boersma, K., Yu, H., Dörner, S., Hilboll, A., Richter, A., Liu, M., Lamsal, L. N., Barkley, M., De Smedt, I., Van Roozendael, M., Wang, Y., Wagner, T., Beirle, S., Lin, J.-T., Krotkov, N., Stammes, P., Wang, P., Eskes, H. J., and Krol, M.: Structural uncertainty in air mass factor calculation for NO2 and HCHO satellite retrievals, Atmos. Meas. Tech., 10, 759–782, https://doi.org/10.5194/amt-10-759-2017, 2017.

Loyola, D. G., Gimeno García, S., Lutz, R., Argyrouli, A., Romahn, F., Spurr, R. J. D., Pedergnana, M., Doicu, A., Molina García, V., and Schüssler, O.: The operational cloud retrieval algorithms from TROPOMI on board Sentinel-5 Precursor, Atmos. Meas. Tech., 11, 409–427, https://doi.org/10.5194/amt-11-409-2018, 2018.

Lutz, R., Loyola, D., Gimeno García, S., and Romahn, F.: OCRA radiometric cloud fractions for GOME-2 on MetOp-A/B, Atmos. Meas. Tech., 9, 2357–2379, https://doi.org/10.5194/amt-9-2357-2016, 2016.

Martin, R. V., et al., An improved retrieval of tropospheric nitrogen dioxide from GOME, J. Geophys. Res., 107(D20), 4437, doi:10.1029/2001JD001027, 2002.

Münch, B., Trtik, P., Marone, F., and Stampanoni, M.: Stripe and ring artifact removal with combined wavelet – Fourier filtering, Opt. Express, 17, 8567–8591, do:10.1364/OE.17.008567, 2009.

Oldeman, A. M.: Effect of including an intensity offset in the DOAS NO2 retrieval of TROPOMI, Internship report, R-1944-SE, Eindhoven University of Technology, Eindhoven, The Netherlands, 2018.

Palmer, P. I., Jacob, D. J., Chance, K. V., Martin, R. V., D, R. J., Kurosu, T. P., Bey, I., Yantosca, R. and Fiore, A.: Air mass factor formulation for spectroscopic measurements from satellites: Application to formaldehyde retrievals from the Global Ozone Monitoring Experiment, Journal of Geophysical Research, 106(D13), 14539-14550, doi:10.1029/2000JD900772, 2001.

Puķīte, J., Kühl, S., Deutschmann, T., Platt, U. and Wagner, T.: Extending differential optical absorption spectroscopy for limb measurements in the UV, Atmos. Meas. Tech., 3(3), 631–653, doi:10.5194/amt-3-631-2010, 2010.

Richter, A.: qa4ecv_no2_inhomogeneous_scenes_171221, in QA4ECV technical note, Treatment of inhomogeneous scenes., 2018.

Rodgers, C. D. and Connor, B. J.: Intercomparison of remote sounding instruments, J. Geophys. Res., 108, https://doi.org/10.1029/2002JD002299, 2003.

Rodgers, C. D.: Inverse Methods for Atmospheric Sounding, Theory and Practice, World Scientific Publishing, Singapore-New-Jersey-London-Hong Kong, 2000.

Schneising, O., Buchwitz, M., Hachmeister, J., Vanselow, S., Reuter, M., Buschmann, M., Bovensmann, H., and Burrows, J. P.: Advances in retrieving XCH4 and XCO from Sentinel-5 Precursor: improvements in the scientific TROPOMI/WFMD algorithm, Atmos. Meas. Tech., 16, 669–694, doi:10.5194/amt-16-669-2023, 2023.Seo, S., Valks, P., Boersma, K. F., De Smedt, I., Pinardi, G., Liu, S., Richter, A., and Loyola, D.: Development and evaluation of a long-term NO2 data recored from GOME-2 observations, in preparation, 2023.

Theys, N. et al., S5P/TROPOMI SO_2 ATBD, 2023. Available at: https://sentinel.esa.int/web/sentinel/technical-guides/sentinel-5p/products-algorithms.

Theys, N., De Smedt, I., Yu, H., Danckaert, T., van Gent, J., Hörmann, C., Wagner, T., Hedelt, P., Bauer, H., Romahn, F., Pedergnana, M., Loyola, D. and Van Roozendael, M.: Sulfur dioxide retrievals from TROPOMI onboard Sentinel-5 Precursor: algorithm theoretical basis, Atmos. Meas. Tech., 10(1), 119–153, doi:10.5194/amt-10-119-2017 , 2017.

Theys, N., Fioletov, V., Li, C., De Smedt, I., Lerot, C., McLinden, C., Krotkov, N., Griffin, D., Clarisse, L., Hedelt, P., Loyola, D., Wagner, T., Kumar, V., Innes, A., Ribas, R., Hendrick, F., Vlietinck, J., Brenot, H., and Van Roozendael, M.: A sulfur dioxide Covariance-Based Retrieval Algorithm (COBRA): application to TROPOMI reveals new emission sources, Atmos. Chem. Phys., 21, 16727–16744, https://doi.org/10.5194/acp-21-16727-2021, 2021.

Theys, N., Lerot, C., Brenot, H., van Gent, J., Smedt, I. D., Clarisse, L., Burton, M., Varnam, M., Hayer, C., Esse, B., and Van Roozendael, M.: Improved retrieval of SO 2 plume height from TROPOMI using an iterative Covariance-Based Retrieval Algorithm, Atmos. Meas. Tech., 15, 4801–4817, https://doi.org/10.5194/amt-15-4801-2022, 2022.

Tilstra, L. G., Tuinder, O. N. E., Wang, P., and Stammes, P.: Directionally dependent Lambertian-equivalent reflectivity (DLER) of the Earth's surface measured by the GOME-2 satellite instruments, Atmos. Meas. Tech., 14, 4219–4238, https://doi.org/10.5194/amt-14-4219-2021, 2021.

Tilstra, L.G., TROPOMI ATBD of the directionally dependent surface Lambertian-equivalent reflectivity, KNMI Report S5P-KNMI-L3-0301-RP, Issue 2.1.0, September 4, 2023.

Valks, P., Chan, L., Hedelt, P., Slijkhuis, S., and Lutz, R.: Algorithm Theoretical Basis Document for GOME-2 Total Column Products of Ozone, NO_2, BrO, SO_2, H2O, HCHO and Cloud Properties (GDP 4.8 for GOME-2 on MetOp-A and B, GDP 4.9 for GOME-2 on MetOp-C), Tech. rep., SAF/AC/DLR/ATBD/01, Iss./Rev.: 3/B, 2019.

Van Damme, M., Clarisse, L., Franco, B., Sutton, M. A., Erisman, J. W., Kruit, R. W., van Zanten, M., Whitburn, S., Hadji-Lazaro, J., Hurtmans, D., Clerbaux, C., and Coheur, P.-F.: Global,

regional and national trends of atmospheric ammonia derived from a decadal (2008–2018) satellite record, Environ. Res. Lett., https://doi.org/10.1088/1748-9326/abd5e0, 2021.

Van Damme, M., Whitburn, S., Clarisse, L., Clerbaux, C., Hurtmans, D., and Coheur, P.-F.: Version 2 of the IASI NH 3 neural network retrieval algorithm: near-real-time and reanalysed datasets, Atmos. Meas. Tech., 10, 4905–4914, https://doi.org/10.5194/amt-10-4905-2017, 2017.

van Geffen, J. H. G. M., Eskes, H. J., Boersma, K. F., and Veefkind, J. P.: TROPOMI ATBD of the total and tropospheric NO_2 data products, Tech. Rep. S5P-KNMI-L2-0005-RP, Koninklijk Nederlands Meteorologisch Instituut (KNMI), https://sentinels.copernicus.eu/documents/247904/2476257/ Sentinel-5P-TROPOMI-ATBD-NO2-data-products, CI-7430-ATBD, issue 2.2.0, 16 June 2021.

van Geffen, J., Boersma, K. F., Eskes, H., Sneep, M., ter Linden, M., Zara, M., and Veefkind, J. P.: S5P TROPOMI NO_2 slant column retrieval: method, stability, uncertainties and comparisons with OMI, Atmos. Meas. Tech., 13, 1315–1335, https://doi.org/10.5194/amt-13-1315-2020, 2020.

van Geffen, J., Eskes, H., Compernolle, S., Pinardi, G., Verhoelst, T., Lambert, J.-C., Sneep, M., ter Linden, M., Ludewig, A., Boersma, K. F., and Veefkind, J. P.: Sentinel-5P TROPOMI NO_2 retrieval: impact of version v2.2 improvements and comparisons with OMI and ground-based data, Atmos. Meas. Tech., 15, 2037–2060, https://doi.org/10.5194/amt-15-2037-2022, 2022.

Verhoelst, T., Compernolle, S., Pinardi, G., Lambert, J.-C., Eskes, H. J., Eichmann, K.-U., Fjæraa, A. M., Granville, J., Niemeijer, S., Cede, A., Tiefengraber, M., Hendrick, F., Pazmiño, A., Bais, A., Bazureau, A., Boersma, K. F., Bognar, K., Dehn, A., Donner, S., Elokhov, A., Gebetsberger, M., Goutail, F., Grutter de la Mora, M., Gruzdev, A., Gratsea, M., Hansen, G. H., Irie, H., Jepsen, N., Kanaya, Y., Karagkiozidis, D., Kivi, R., Kreher, K., Levelt, P. F., Liu, C., Müller, M., Navarro Comas, M., Piters, A. J. M., Pommereau, J.-P., Portafaix, T., Prados-Roman, C., Puentedura, O., Querel, R., Remmers, J., Richter, A., Rimmer, J., Rivera Cárdenas, C., Saavedra de Miguel, L., Sinyakov, V. P., Stremme, W., Strong, K., Van Roozendael, M., Veefkind, J. P., Wagner, T., Wittrock, F., Yela González, M., and Zehner, C.: Ground-based validation of the Copernicus Sentinel-5P TROPOMI NO_2 measurements with the NDACC ZSL-DOAS, MAX-DOAS and Pandonia global networks, Atmos. Meas. Tech., 14, 481–510, https://doi.org/10.5194/amt-14-481-2021, 2021.

Volkamer, R., Baidar, S., Campos, T. L., Coburn, S., DiGangi, J. P., Dix, B., Eloranta, E. W., Koenig, T. K., Morley, B., Ortega, I., Pierce, B. R., Reeves, M., Sinreich, R., Wang, S., Zondlo, M. A. and Romashkin, P. A.: Aircraft measurements of BrO, IO, glyoxal, NO_2, H2O, O2–O2 and aerosol extinction profiles in the tropics: comparison with aircraft-/ship-based in situ and lidar measurements, Atmos. Meas. Tech., 8(5), 2121–2148, doi:10.5194/amt-8-2121-2015, 2015.

Walker, J. C., Dudhia, A., and Carboni, E.: An effective method for the detection of trace species demonstrated using the MetOp Infrared Atmospheric Sounding Interferometer, Atmos. Meas. Tech., 4, 1567–1580, https://doi.org/10.5194/amt-4-1567-2011, 2011.

Wang, P., P. Stammes, R. van der A, G. Pinardi, and M. van Roozendael, FRESCO+: an improved O2 A-band cloud retrieval algorithm for tropospheric trace gas retrievals, Atmos. Chem. Phys., 8, 6565-6576, doi:10.5194/acp-8-6565-2008, 2008.

Wang, P., Piters, A., van Geffen, J., Tuinder, O., Stammes, P., and Kinne, S.: Shipborne MAX-DOAS measurements for validation of TROPOMI NO_2 products, Atmos. Meas. Tech., 13, 1413–1426, https://doi.org/10.5194/amt-13-1413-2020, 2020.

Wang, W., Liu, C., Clarisse, L., Van Damme, M., Coheur, P.-F., Xie, Y., Shan, C., Hu, Q., Zhang, H., Sun, Y., Yin, H., and Jones, N.: Spatial distribution and seasonal variability in atmospheric ammonia measured from ground-based FTIR observations at Hefei, China, Atmos. Meas. Tech. Discuss., https://doi.org/10.5194/amt-2020-39, 2020.

Whitburn, S., Clarisse, L., Bouillon, M., Safi eddine, S., George, M., Dewitte, S., De Longueville, H., Coheur, P.-F., and Clerbaux, C.: Trends in spectrally resolved outgoing longwave radiation from 10 years of satellite measurements, NPJ Clim. Atmos. Sci., 4, https://doi.org/10.1038/s41612-021-00205-7, 2021.

Whitburn, S., Clarisse, L., Crapeau, M., August, T., Hultberg, T., Coheur, P. F., and Clerbaux, C.: A CO 2 -independent cloud mask from Infrared Atmospheric Sounding Interferometer (IASI) radiances for climate applications, Atmos. Meas. Tech., 15, 6653–6668, https://doi.org/10.5194/amt-15-6653-2022, 2022.

Whitburn, S., Van Damme, M., Clarisse, L., Bauduin, S., Heald, C. L., Hadji-Lazaro, J., Hurtmans, D., Zondlo, M. A., Clerbaux, C., and Coheur, P.-F.: A flexible and robust neural network IASI-NH 3 retrieval algorithm, J. Geophys. Res., 121, 6581–6599, https://doi.org/10.1002/2016jd024828, 2016.

Williams, J. E., Boersma, K. F., Le Sager, P., and Verstraeten, W. W.: The high-resolution version of TM5-MP for optimized satellite retrievals: description and validation, Geosci. Model Dev., 10, 721-750, doi:10.5194/gmd-10-721-2017, 2017.

Zara, M., Boersma, K. F., De Smedt, I., Richter, A., Peters, E., van Geffen, J. H. G. M., Beirle, S., Wagner, T., Van Roozendael, M., Marchenko, S., Lamsal, L. N., and Eskes, H. J.: Improved slant column density retrieval of nitrogen dioxide and formaldehyde for OMI and GOME-2A from QA4ECV: intercomparison, uncertainty characterisation, and trends, Atmos. Meas. Tech., 11, 4033–4058, https://doi.org/10.5194/amt-11-4033-2018, 2018.

Zhou, D. K., Larar, A. M., and Liu, X.: MetOp-A/IASI Observed Continental Thermal IR Emissivity Variations, IEEE J. Sel. Topics Appl. Earth Observations Remote Sens., 6, 1156–1162, https://doi.org/10.1109/JSTARS.2013.2238892, 2013.